UC San Diego
UC San Diego Electronic Theses and Dissertations

Title

Wedge Inelasticity and Fully Coupled Models of Dynamic Rupture, Ocean Acoustic Waves, and Tsunami for Megathrust Earthquakes in the Japan Trench

Permalink

https://escholarship.org/uc/item/9f612441

Author

Du, Yue

Publication Date

2024

Supplemental Material

https://escholarship.org/uc/item/9f612441#supplemental

Peer reviewed|Thesis/dissertation

UNIVERSITY OF CALIFORNIA SAN DIEGO

SAN DIEGO STATE UNIVERSITY

Wedge Inelasticity and Fully Coupled Models of Dynamic Rupture, Ocean Acoustic Waves, and Tsunami for Megathrust Earthquakes in the Japan Trench

A Dissertation submitted in partial satisfaction of the requirements
for the degree Doctor of Philosophy

in

Geophysics

by

Yue Du

Committee in charge:

University of California San Diego

Yehuda Bock
John S. McCartney

San Diego State University

Shuo Ma, Chair
Steven M. Day
Ignacio Sepúlveda

2024

The Dissertation of Yue Du is approved, and it is acceptable in quality
and form for publication on microfilm and electronically.

_____

_____

_____

_____

_____
Chair

University of California San Diego

San Diego State University

2024

TABLE OF CONTENTS

LIST OF FIGURES

LIST OF TABLES

LIST OF SUPPLEMENTAL FILES

Movie 1.1. Movie of slip velocity, vertical seafloor velocity, dynamic ocean bottom pressure change, sea surface elevation, and seafloor displacement vectors and inelastic shear strain in the wedge at 6 cross sections in the inelastic model.

Movie 1.2. Similar to Movie 3.1 except for the elastic model. The difference with the inelastic model lies mostly in the northern Japan Trench.

Movie 1.3. Movie of slip velocity, shear stress change, slip, seafloor vertical velocity, dynamic ocean bottom pressure change, sea surface elevation, and seafloor displacement vectors at 6 cross sections in the elastic model.

Movie 1.4. Similar to Movie 4.1 except for the inelastic model.

Movie 1.5. Similar to Movie 4.1 except for a southern hypocenter (elastic model).

Movie 1.6. Similar to Movie 4.2 except for a southern hypocenter (inelastic model).

Movie 1.7. Similar to Movie 4.1 except for a northern hypocenter (elastic model).

Movie 1.8. Similar to Movie 4.2 except for a northern hypocenter (inelastic model).

ACKNOWLEDGEMENTS

Shuangyi Liu, and Yi Wang. Having each of them in my life has truly been a blessing, and I am grateful for every moment we've shared.

VITA

2018   Bachelor of Science in Geophysics, University of Toronto

2024   Doctor of Philosophy in Geophysics, University of California San Diego & San Diego State University

PUBLICATIONS

Du, Y., Ma, S., Kubota, T., & Saito, T. (2021). Impulsive tsunami and large runup along the sanriku coast of Japan produced by an inelastic wedge deformation model. *Journal of Geophysical Research: Solid Earth, 126*(8).

Du, Y., Ma, S., Wedge Inelasticity and Fully Coupled Models of Dynamic Rupture, Ocean Acoustic Waves, and Tsunami in the Japan Trench: 1. The 2011 Tohoku-Oki Earthquake. *In preparation for publication.*

Du, Y., Ma, S., Wedge Inelasticity and Fully Coupled Models of Dynamic Rupture, Ocean Acoustic Waves, and Tsunami in the Japan Trench: 2. The 1896 Sanriku Earthquake. *In preparation for publication.*

ABSTRACT OF THE DISSERTATION

Wedge Inelasticity and Fully Coupled Models of Dynamic Rupture, Ocean Acoustic Waves, and Tsunami for Megathrust Earthquakes in the Japan Trench

by

Yue Du

Doctor of Philosophy in Geophysics

University of California San Diego, 2024
San Diego State University, 2024

Professor Shuo Ma, Chair

In this dissertation I investigate the physics of tsunami generation and seismic/acoustic radiations of two megathrust earthquakes in the Japan Trench. Elastic dislocation theory has been widely used for modeling shallow subduction earthquakes and tsunami generation, but several important observations in the 2011 M_W 9.1 Tohoku-Oki earthquake contradict the theory, including diminishing shallow slip observed in the northern Japan Trench from differential

bathymetry observations before and after the earthquake where the largest tsunami (up to 40 m) was generated and deficiency in high-frequency radiation associated with large tsunamigenesis. The 1896 Sanriku earthquake was a devastating tsunami earthquake with similar characteristics in the northern Japan Trench. Here I test an inelastic wedge deformation hypothesis in explaining these anomalous but important observations. Chapter 1 serves as an introduction to this dissertation. In Chapter 2, inelastic wedge deformation in the thick sediment of northern Japan Trench is shown as a mechanism to produce impulsive tsunami that can explain the extreme runup of the 1896 Sanriku tsunami. Chapters 3 and 4 present models of the 2011 Tohoku-Oki earthquake and 1896 Sanriku earthquake by fully coupling dynamic rupture, ocean acoustic waves, and tsunami with a finite-element code. Inelastic wedge deformation is shown in both earthquakes to cause depletion in high-frequency radiation but efficient tsunami generation with diminishing shallow slip, consistent with the observations. The inelastic deformation hypothesis may be applicable to accretionary and other sediment-rich margins. These results have important implications for tsunami hazard assessment and reduction around the world.

Chapter 1

INTRODUCTION

Despite unprecedented seismic, geodetic, and tsunami observations on- and off-shore and numerous published models for the 2011 M_W 9.1 Tohoku earthquake, the fundamental question of what generated the devasting tsunami in the Japan Trench remains unsolved (e.g., Kodaira et al., 2021). The largest tsunami runup (up to 40 m) were observed north of 39°N along the Sanriku coast more than 100 km north of the epicenter (~38.1°N). The tsunami heights along the Sanriku coast were consistently 2 – 3 times larger than the south, causing immense devastations. The differential bathymetry before and after the earthquake near 38.1°N observed more than 50 m horizontal seafloor displacement within ~40 km landward from the trench (Fujiwara et al., 2011), indicating large slip at the trench. Most kinematic slip models also inferred large slip at the trench near 38.1°N (e.g., Sun et al., 2017; Lay, 2018; and references therein), consistent with the differential bathymetry observation. However, nearly all the models using seismic and/or geodetic models resolved little shallow slip north of 38.5°N, incapable of explaining the large tsunami along the Sanriku coast (e.g., Tappin et al, 2014; Yamazaki et al., 2018).

In order to explain the large tsunami runup along the Sanriku coast, kinematic slip models using tsunami data requires up to 36 m slip at or near the trench north of 38.5°N (e.g., Satake et al., 2013; Yamazaki et al., 2018). However, differential bathymetry at two profiles at 39.2 – 39.5°N indicated no large shallow slip at the trench nor large submarine landslides (Fujiwara et al., 2017). Also, turbidite units, correlating with large near-trench slip in the Japan Trench, were not observed north of ~38.7°N (e.g., Ikehara et al., 2018; Uchida & Bürgmann, 2021). Both the differential

bathymetry and turbidite observations seem to suggest a completely different deformation mode in the northern Japan Trench.

Without large near-trench slip or submarine landslides what produced the large tsunami along the Sanriku coast? This question needs to be fully addressed as it relates to the fundamental physics of tsunami generation, which has important implications for tsunami hazard assessment and reduction worldwide.

The prevailing hypothesis for large tsunamigenesis is large shallow slip near the trench (e.g., Satake & Tanioka, 1999; Lay et al., 2012), based on elastic dislocation theory of faulting. Nearly all the models for the 2011 Tohoku-Oki earthquake and other large tsunamigenic earthquakes are elastic dislocation models. However, applying elastic dislocation theory to shallow subduction zones can be questionable for several reasons (Wilson & Ma, 2021): (a) the overriding wedge may have low strength due to weak sediments; (b) the outer wedge in accretionary margins subject to intense deformation geologically may be at or close to failure (e.g., Dahlen, 1990); (c) elevated pore pressure can be prevalent in the wedge due to low permeability of sediments (e.g., Saffer & Tobin, 2011); (d) thin-skinned wedge geometry gives rise to low confining pressure and can result in large dynamic stress concentration during earthquake rupture; and (e) dynamic pore pressure increase due to updip rupture and increase of fault friction in the shallow velocity-strengthening region can weaken the wedge (Wang & Hu, 2006). These mechanisms can lead to inelastic deformation in the overriding wedge (e.g., Ma, 2012; Ma and Hirakawa, 2013), which may be why elastic dislocation models failed to reconcile the key observations of the 2011 Tohoku-Oki earthquake and tsunami.

Inelastic wedge deformation can cause efficient seafloor uplift landward from trench with diminishing shallow slip on the fault (Ma, 2012). The higher efficiency is due to frictional sliding

on conjugate microfractures with steeper dips than that of the plate interface. Inelastic wedge deformation is also a large energy sink due to plastic dissipation that can lead to slow rupture velocity, deficiency in high-frequency seismic radiation, and low moment-scaled radiated energy (Ma and Hirakawa, 2013), which have been anomalously observed for tsunami earthquakes and shallow slip kinematics of large tsunamigenic earthquakes for nearly 50 years (e.g., Kanamori, 1972; Lay et al., 2012; Ye et al., 2016). Ma and Nie (2019) extended the inelastic wedge deformation model to 3D and showed that for a ~M_W 8.0 earthquake along-strike variation of wedge strength (due to variation of sediment thickness) and dynamic wedge failure can lead to along-strike variations of shallow slip and seafloor uplift. Sediment thickness increases significantly from south to north along the Japan Trench (e.g., Tsuru et al., 2012). Ma and Nie (2019) suggested that in the south where the sediment is thin the wedge deformation is mostly elastic, leading to large shallow slip and predominantly horizontal seafloor displacement. However, in the north the thick wedge sediment can cause significant inelastic deformation, which produces large seafloor uplift with diminishing shallow slip. Ma (2023) extended this mechanism and modelled the 2011 M_W 9.1 Tohoku-Oki earthquake.

Another anomalous observation in the 2011 M_W 9.1 Tohoku-Oki earthquake is weak high-frequency radiation in the northern Japan Trench. The seismic intensity along the Sanriku coast was significantly less than the south (e.g., Kodaira et al., 2021). Nearly all the slip models based on seismic data failed to resolve the rupture north of 39°N, which is consistent with depletion in high-frequency radiation. The 1896 Sanriku earthquake also occurred in the northern Japan Trench, which produced a devastating tsunami that killed more 22,000 people (e.g., Shuto et al., 2007) but is depleted in high-frequency radiation. Kanamori (1972) classified this class of

earthquakes as tsunami earthquake. Physics of depletion in high-frequency radiation associated with large tsunamigenesis is, however, not well understood by the elastic dislocation theory.

In this dissertation, I will test a hypothesis based on inelastic wedge deformation to explain both the anomalous depletion in high-frequency radiation and large tsunamigenesis as observed in both earthquakes.

In Chapter 2, the 1896 Sanriku tsunami is modelled by using the final seafloor displacement from dynamic rupture models incorporating inelastic deformation of Ma & Nie (2019) as sea surface initial condition. Tsunami propagation and runup are modelled by solving a nonlinear Boussinesq equation using a multi-grid finite-difference code. The inelastic deformation model produces short-wavelength seafloor uplift with diminishing slip near trench, while generating tsunami efficiently. This model provides a mechanism for the impulsive tsunami waves recorded offshore the Sanriku coast in 2011. The amplification of short-wavelength (impulsive) tsunami by the rugged Sanriku coast is shown to lead to extreme runup. The model produces runups consistent with the observations of the 1896 Sanriku tsunami with little model tuning.

Chapter 3 presents fully coupled models of dynamic rupture, ocean acoustic waves, and tsunami for the 2011 M_W 9.1 Tohoku-Oki Earthquake. A compressible ocean is added to the model of Ma (2023) to rigorously simulate tsunami and ocean acoustic waves. The inelastic deformation of thick sediment in the northern Japan Trench is shown to cause slow rupture velocity (~850 m/s), large seafloor uplift (~4 m) with diminishing slip, and weak radiation of ocean acoustic and seismic waves, consistent with the observations. South of 39°N, fast rupture velocity (~3 km/s), large slip at trench (>50 m), and dominantly elastic wedge response produce strong radiation. Ocean acoustic waves due to their high-frequency nature have little sensitivity to tsunami (sensitive to static deformation), which may not provide robust signals for tsunami early warning. This chapter also

shows that modest inelastic deformation leads to long slip duration and locally large shallow slip enhanced by the hydroacoustic dilation of ocean.

Fully coupled models of dynamic rupture, ocean acoustic waves, and tsunami for the 1896 Sanriku earthquake are shown in Chapter 4. A 3D critical wedge solution is used to set up the stress and pore pressure conditions in the model. The rupture zone is very shallow, within 40 km from the trench. The inelastic deformation of wedge sediment in the northern Japan Trench is shown to generate efficient short-wavelength seafloor uplift (>5 m), which is several times larger than the uplift by elastic dislocation models and generates impulsive tsunami that can have large impact on the rugged Sanriku Coast. The inelastic wedge deformation is, however, a large energy sink, which causes slower rupture velocity, weaker radiation of ocean acoustic and seismic waves, and ~10 times lower moment-scaled radiated energy than from elastic models, explaining nearly all the anomalous characteristics of this tsunami earthquake. The anti-plane shear stress in the mode III rupture direction (along strike), limited by yielding, plays an important role in the slow rupture velocity and energy radiation along strike. Again, these results suggest that ocean acoustic waves may not provide robust signals for tsunami early warning due to weak high-frequency radiation by inelastic deformation. Large, long-duration ground velocity pulses can naturally result from inelastic deformation, which provide important implications for the long-period ground motion observations in the 1999 ChiChi, Taiwan, earthquake and other surface-rupturing earthquakes.

Chapter 2

Impulsive Tsunami and Large Runup Along the Sanriku Coast of Japan Produced by an Inelastic Wedge Deformation Model

Abstract

Dynamic wedge failure produces short-wavelength seafloor uplift efficiently with diminishing shallow slip on the plate interface, generating impulsive tsunami. For ria coasts with prevalent small-wavelength bathymetric features, such as the Sanriku coast of Japan, impulsive tsunami can be amplified to produce large runup. We model tsunami propagation and runup of the 1896 Sanriku tsunami by using the seafloor deformation from dynamic rupture models of Ma & Nie (2019) for a M_W 8 earthquake with inelastic wedge deformation. The fully nonlinear Boussinesq equation is solved by a nested-grid finite-difference method with high-resolution bathymetry data. We show that the inelastic wedge deformation model produces impulsive tsunami similar to those observed offshore the Sanriku coast in the 2011 Tohoku earthquake and generates large runup remarkably consistent with the 1896 Sanriku tsunami. As an alternative to previous models based solely on fault slip, we suggest that the impulsive tsunami and large runup along the Sanriku coast observed in the 2011 Tohoku earthquake can be explained by inelastic wedge deformation north of 38.5°N.

2.1. Introduction

The ria coast of Sanriku region, situated about 50 – 200 km north of the Sendai Plain, witnessed several of the worst tsunamis in recorded history of Japan (Figure 2.1). The 1896 Sanriku earthquake, a ~M_W 8 tsunami earthquake (e.g., Kanamori, 1972; Tanioka & Satake, 1996; Tanioka & Seno, 2001; Satake et al., 2017), generated weak high-frequency ground shaking, but the resulting tsunami produced runup up to 38.2 m on the Sanriku coast, causing about 22,000 deaths (Shuto et al., 2007). The Sanriku coast was hit by another tsunami due to a M_W 8.4 outer rise earthquake in 1933 with runup as high as 28.7 m (e.g., Abe, 1978; Kanamori, 1971; Mori et al., 2011). In the 2011 M_W 9.0 Tohoku earthquake the largest tsunami runup heights (up to 40 m) were observed on the Sanriku coast (Mori et al., 2011; Figure 2.2), causing catastrophic destructions more than 100 km north of the epicenter (~38.1°N). However, the largest shallow slip near the trench (more than 50 m) was observed (Fujiwara et al., 2011; Kodaira et al., 2020) or inferred from most inversion models (Lay, 2018; and references therein) updip from the hypocenter. The maximum tsunami runup heights are quite similar on the Sanriku coast between the 1896 and 2011 earthquakes despite their different magnitudes (Figure 2.2).

Why does the Sanriku coast host such devastating tsunamis? Why did the largest tsunami in the 2011 Tohoku earthquake occur more than 100 km north of the largest shallow slip region (near 38.1°N)? In order to explain the large tsunami runup on the Sanriku coast, elastic dislocation models require large shallow slip (up to 36 m) near the trench north of ~38.5°N (e.g., Satake et al., 2013; Yamazaki et al., 2018). However, differential bathymetry data before and after the earthquake around 39.2° – 39.5°N indicated no large shallow slip near the trench (Fujiwara et al., 2017; Kodaira et al., 2020). The bathymetry data also ruled out the possibility of a large submarine landslide (Tappin et al., 2014).

Without large shallow slip at trench or submarine landslide what caused the devastating tsunami along the Sanriku coast in the 2011 Tohoku earthquake? This is a major unresolved question related to the 2011 Tohoku earthquake despite unprecedented onshore and offshore data and numerous published models in the last ten years (Kodaira et al., 2021). This question challenges current understanding of the fundamental physics of tsunamigenesis and needs to be critically addressed, which will be instrumental in evaluating and reducing tsunami hazard in the Japan Trench and other subduction zones worldwide. The prevailing hypothesis of large shallow slip in explaining tsunami generation is based on elastic dislocation theory, which may not be applicable in shallow subduction zones with thick sediments and therefore cannot reconcile with these key observations in the 2011 Tohoku earthquake. We refer the reader to Ma & Nie (2019) for more detailed discussion of physical mechanisms of tsunamigenesis and possible issues associated with elastic dislocation models.

Fujiwara et al. (2017) suggested that differential bathymetry data is more consistent with widespread inelastic deformation of wedge sediments (Tanioka & Seno, 2001). Ma (2012) and Ma & Hirakawa (2013) modeled inelastic wedge deformation in 2D dynamic rupture models of shallow subduction earthquakes by using the undrained Mohr-Coulomb plasticity theory. They showed that inelastic wedge deformation is more efficient to generate seafloor uplift than large shallow slip on a shallow dipping fault due to frictional sliding on conjugate Coulomb microfractures with steeper dips (the efficiency is defined by peak seafloor uplift scaled by seismic potency). With significant inelastic deformation large seafloor uplift occurs landward from the trench with diminishing shallow slip on the fault, which is consistent with the observation of Fujiwara et al. (2017). Inelastic deformation is also a large energy sink (Ma & Hirakawa, 2013), which can lead to slow rupture velocity, deficiency of high-frequency seismic radiation, and low

moment-scaled radiated energy, observed anomalously for tsunami earthquakes and in the shallow rupture characteristics of large tsunamigenic earthquakes (e.g., Lay et al., 2012).

Ma & Nie (2019) extended the inelastic wedge deformation model to 3D and modeled a M$_W$ 8.0 shallow subduction earthquake, similar to the 1896 Sanriku earthquake. They showed that along-strike variation of sediment thickness (thus wedge strength), such as in the Japan Trench (Tsuru et al., 2002; Kodaira et al., 2017), can cause along-strike variation of inelastic wedge deformation. In particular, they suggested that due to thick sediments north of 38.5°N inelastic deformation of sedimentary wedge can produce large seafloor uplift with diminishing shallow slip. In contrast, the scarcity of sediments in the south (near 38.1°N) induces mostly elastic wedge deformation, generating large shallow slip and mostly horizontal seafloor displacement but small uplift near the trench. Although the horizontal seafloor displacement can significantly contribute to tsunami generation (e.g., Tanioka & Satake, 1996) the efficiency of generating seafloor uplift (uplift normalized by slip) can be limited by the overall gentle slope of seafloor. The along-strike variations of shallow slip and seafloor uplift near the trench in the model are similar to the observations in the 2011 Tohoku earthquake (Fujiwara et al., 2011, 2017; Mori et al., 2011), suggesting a plausible mechanism for both large slip at the trench near 38.1°N and the devastating tsunami on the Sanriku coast without large northern trench slip in the 2011 Tohoku earthquake.

Another rare and intriguing observation in the 2011 Tohoku tsunami is that two ocean bottom pressure gauges (TM1 and TM2) and three GPS wave gauges off the Sanriku coast (Iwate N, M, and S) recorded an impulsive tsunami signal on top of a broad signal due to high sampling rates of the instruments (Figure 2.2). The impulsive signal was not observed south of the Sanriku coast. The broad signal is due to long-wavelength seafloor uplift caused by deep slip on a ~200 km wide fault south of ~39°N (e.g., Satake et al., 2013). The nature of the impulsive signal,

however, is not well understood. The width of the impulsive signal is approximately 3 – 4 minutes at TM1 and TM2, which was thought to be caused by large localized slip at the trench near 38.1°N (e.g., Maeda et al., 2011). Later tsunami inversions (e.g., Satake et al., 2013; Yamazaki et al., 2018) attributed the impulsive signal to large near-trench slip north of 38.5°N. Tappin et al. (2014) fit the impulsive signals and runup on the Sanriku coast by using a submarine landslide model. As mentioned previously, all these models are inconsistent with the bathymetry observations of Fujiwara et al. (2017).

In this work, we will show that such impulsive tsunami signals can be a direct result of short-wavelength seafloor uplift produced by inelastic wedge deformation. Several studies (e.g., Shimozono et al., 2012, 2014; Yamazaki et al., 2018; Yamanaka et al., 2020) showed that the rugged Sanriku coast, characterized by steep terrains and narrow and long bays, can greatly amplify the impulsive (short-period) tsunami to cause large runup, although local amplification patterns can be highly nonlinear (e.g., Rogers & Mei, 1978). The amplification of long-period tsunami on the Sanriku coast due to long-wavelength seafloor uplift south of ~39°N in the 2011 Tohoku earthquake was found significantly less (e.g., Yamanaka et al., 2020). This frequency-dependent amplification on the Sanriku coast may explain why the short-wavelength tsunami of the 1896 and 1933 Sanriku earthquakes produced similar runup to the 2011 Tohoku earthquake despite their different magnitudes. Below we will show acute sensitivity of the runup on the Sanriku coast to impulsive tsunami generated by inelastic wedge deformation. Thus, inelastic wedge deformation is a mechanism that can explain both the impulsive tsunami and large runup along the Sanriku coast without large trench slip, as observed in the 2011 Tohoku earthquake.

To demonstrate that inelastic wedge deformation can produce impulsive tsunami, we will model the 1896 Sanriku tsunami by using the seafloor displacements from two models of Ma &

Nie (2019) as the initial conditions. The models represent M_W 8 shallow subduction earthquakes, with fault geometry and rupture extent following that of Tanioka & Seno (2001) for the 1896 Sanriku earthquake. The slight difference is that Ma & Nie (2019) included a seafloor slope, while Tanioka & Seno (2001) used a flat seafloor. One model has mostly elastic wedge response with large shallow slip at the trench and mostly horizontal seafloor displacement (Figure 2.3). The second model (Figure 2.4) has significant inelastic wedge deformation, which generates narrow and large uplift landward from the trench with diminishing shallow slip. Such narrow uplift will be shown to directly lead to impulsive tsunami similar to those observed in 2011. The differences between these two models are due to different wedge strengths, characterized by a closeness-to-failure (*CF*) parameter. The *CF* is defined as the ratio of square root of second invariant of deviatoric stress tensor to yield stress in a Drucker-Prager yield criterion (see equation 3 of Ma & Nie, 2019), which is between 0 and 1. The *CF* of 0.7 and 0.95 was used everywhere in the wedge in Figures 2.3 and 2.4, respectively. As the *CF* increases, the wedge is less cohesive and closer to failure; wedge failure due to dynamic stresses during rupture propagation gives rise to significant inelastic deformation and distinctly different seafloor deformation.

Hereafter we will refer to the model in Figure 2.3 as model I and Figure 2.4 as model II. Model II is likely more applicable to the 1896 Sanriku earthquake due to the presence of thick sediments north of 38.5°N (Tsuru et al., 2002). The moment magnitudes (M_W) for these two models are 8.01 and 7.95, respectively. More detailed discussion of the two models and how variation of sediment thickness may lead to along-arc variation of inelastic deformation in the Japan Trench can be found in Ma & Nie (2019). We will also consider a kinematic slip model of the 1896 Sanriku earthquake (based on elastic dislocation theory), which is the final model of Satake et al. (2017). The model (M_W 8.1) consists of 8 subfaults with large localized buried slip

(20 m) on two subfaults at depths of about 3.5 – 7 km, illustrated in Figure 2.5d. Each subfault is 50 km long and 25 km wide, with strike 193°, dip 8°, and rake 81°. We will refer to this model as model III in this paper.

We will show that shorter-wavelength seafloor uplift of models II and III produce more impulsive tsunami signal than model I and the former are similar to the observed impulsive signal in the 2011 Tohoku tsunami. Neither model II or III has large trench slip, consistent with the observations of Fujiwara et al. (2017). However, model III may have a plausibility issue due to large stress change in the overriding wedge caused by large localized slip (e.g., Geist & Dmowska, 1999), which may lead to inelastic deformation violating the assumption of elastic dislocation. Model II produces large runup with a remarkable fit to the observed runup of the 1896 Sanriku tsunami (Iki,1897; Matsuo, 1933) without any model tuning. Model I, with a longer-wavelength and smaller seafloor uplift, produces consistently lower tsunami height and runup than model II. The limited along-strike extent of localized buried slip of model III overestimates the runup of the 1896 tsunami between about 39.3°N and 39.9°N and underestimates the runup elsewhere. Given the capability of generating impulsive tsunami and large runup along the Sanriku coast by short-wavelength seafloor uplift we suggest that inelastic deformation of thick wedge sediments north of 38.5°N can likely explain the large tsunami runup on the Sanriku coast in the 2011 Tohoku earthquake while being consistent with the observations of Fujiwara et al. (2017).

2.2. Tsunami modeling

We model the 1896 Sanriku tsunami by solving the fully nonlinear Boussinesq equation in a Cartesian coordinate system

$$\frac{\partial \eta}{\partial t} + \frac{\partial P}{\partial x} + \frac{\partial Q}{\partial y} = 0, \tag{1}$$

$$\frac{\partial P}{\partial t} + \frac{\partial}{\partial x}\left(\frac{P^2}{H}\right) + \frac{\partial}{\partial y}\left(\frac{PQ}{H}\right) + gH\frac{\partial \eta}{\partial x} + \frac{gn^2}{H^{7/3}}P\sqrt{P^2 + Q^2} = \frac{H^2}{3}\frac{\partial}{\partial x}\frac{\partial}{\partial t}\left(\frac{\partial P}{\partial x} + \frac{\partial Q}{\partial y}\right), \tag{2}$$

$$\frac{\partial Q}{\partial t} + \frac{\partial}{\partial x}\left(\frac{PQ}{H}\right) + \frac{\partial}{\partial y}\left(\frac{Q^2}{H}\right) + gH\frac{\partial \eta}{\partial y} + \frac{gn^2}{H^{7/3}}Q\sqrt{P^2 + Q^2} = \frac{H^2}{3}\frac{\partial}{\partial y}\frac{\partial}{\partial t}\left(\frac{\partial P}{\partial x} + \frac{\partial Q}{\partial y}\right), \tag{3}$$

where η is sea surface height, P and Q are volume fluxes in x and y, respectively, g is gravitational acceleration, H is total water depth ($H = \eta + h$, h is initial ocean depth), and n is the Manning's sea bottom roughness coefficient. In this work, a constant Manning's coefficient $n = 0.03 \, m^{-\frac{1}{3}}s$ is used throughout the model (e.g., Saito et al., 2014). The volume fluxes are given by $P = v_x H$ and $Q = v_y H$, where v_x and v_y are depth-averaged flow velocities assuming shallow water. The governing equations written in terms of volume fluxes rather than velocities, known as the conservative form (e.g., Roeber et al., 2010), have a wider range of applications even when the shallow-water assumptions are invalid, such as across a shock or hydraulic jump, and show better accuracy in areas with steep bathymetry gradients (Dresback et al., 2015). Baba et al. (2015) solved the similar equations in a spherical coordinate system.

The Boussinesq equation is widely used in modeling dispersive tsunami propagation (e.g., Horrillo et al., 2006; Saito et al., 2014; Kirby et al., 2013; Tappin et al., 2014; Baba et al., 2015; Hossen et al., 2015; Tanioka et al., 2018). The dispersion is due to the terms on the right side of equations 2 and 3, which approximates true frequency dispersion reasonably well even when tsunami wavelength is not much larger than ocean depth. Baba et al. (2015) further showed that the nonlinear Boussinesq equations 2 and 3 can simulate a remarkable near-coast small-wavelength phenomenon called 'tsunami soliton fission', which is due to frequency dispersion as

well as dispersion from wave amplitude (i.e., wave speed is a function of wave amplitude). Without the two right-side terms equations 2 and 3 reduce to the standard nonlinear shallow water equations, which excludes dispersion. In the following, we will show results both with and without dispersion.

A staggered-grid finite-difference method using nested grids was developed to solve equations 1 – 3, following Baba et al. (2015). Without dispersion, the finite-difference method is fully explicit. To simulate dispersion, we use an iterative implicit solver by the method of successive over-relaxation (Young, 1971), a variant of Gauss-Seidel method. A robust moving boundary scheme (e.g., Saito et al., 2014) was developed to track the instantaneous location of the coastline for accurate runup modelling. An absorbing boundary scheme (Cerjan, et al., 1985) with a sponge layer of 20 grid cells is used on the domain boundaries to avoid wave reflections.

The four grid layers used in this work are shown in Figure 2.1. The largest grid spacing is 1350 m, covering the majority of the computational domain. The grid spacing reduces to 450 m, 150 m, and 50 m successively (in a ratio of 1:3) as the coast is approached. Three overlapping regions in the 150 m grid and five overlapping regions in the 50 m grid are used to cover the Sanriku coast in high resolution. The smaller grid sizes near the coast are essential to resolve short tsunami wavelengths and model runup accurately. A two-way coupling between grid layers is implemented, which is described in detail in Baba et al. (2015). Communications are only allowed between two consecutive grid layers (e.g., between the 50 m and 150 m grids), i.e., no communication is between different regions of the same grid layer (for example, the overlapping regions in the 50 m grid). The use of nested grids significantly reduces the degrees of freedom in the simulations. The bathymetry data provided by the Central Disaster Management Council of

Government of Japan (Saito et al., 2014) are used for all the grid layers. All the simulations are run for 2 hours with a time step of 0.625 s.

2.3. Initial sea surface elevations from three models

To obtain the initial sea surface elevation for the 1896 Sanriku tsunami simulations, we rotate models I and II to follow the same fault strike as in model III (193°) and set the center of fault surface trace at (143.2°E, 39.3°N), which is same as the northeast corner of the third subfault on the east side in model III (Figure 2.5d). The detailed locations of the subfaults in model III are given in Table 1 of Satake et al. (2017). The seafloor displacement in model III is calculated in a homogeneous half space following Okada (1985). In each model, we project the seafloor displacement onto the real bathymetry. We add the contributions of horizontal seafloor displacement due to local bathymetric slope to the vertical displacement to obtain the total seafloor uplift (Tanioka & Satake, 1996). We then apply a lowpass filter (Kajiura, 1963) with a cutoff wavelength of 4 km (e.g, Saito et al., 2014) to obtain the initial sea surface elevation.

Figure 2.5 shows the initial sea surface elevations for the three models. The fault-perpendicular cross sections of horizontal and vertical seafloor displacements and initial sea surface elevations through the center of the fault are shown in Figure 2.6. Model I has large horizontal seafloor displacement and a displacement discontinuity at the trench (blue line, Figure 2.6a) due to large shallow slip (Figure 2.3), while model II has negligible horizontal displacement and no discontinuity at the trench (red line, Figure 2.6a) because of diminishing trench slip caused by inelastic deformation (Figure 2.4). The small slip at shallow subfaults in model III produces modest horizontal displacement at the trench (green line, Figure 2.6a). Due to large localized buried slip (Figure 2.5d) model III produces a narrowest seafloor uplift with a peak amplitude of

15

6.37 m (Figure 2.6b). The peak uplift in model II and I is 4.86 m and 2.15 m, respectively (Figure 2.6b); the larger peak uplift in model II is due to inelastic wedge deformation (see Figures 2.3 and 2.4). The horizontal seafloor displacements contribute significantly to the sea surface elevation due to local bathymetric slope in all three models (Figure 2.6c). However, most of small-wavelength contributions shorter than ocean depth are filtered out by nonhydrostatic response of the ocean (Kajiura, 1963). After the filtering, the large contribution from the horizontal displacement is mostly seen within 30 km from the trench in model I (green solid line, Figure 2.6c). The narrow peak uplift of model III has also been significantly reduced by the filtering, while the peak uplift in model II is only modestly reduced due to the overall smooth nature of the inelastic seafloor deformation.

We compare the filtered profiles of initial sea surface elevation among three models (solid lines, Figure 2.6c). Model I has the longest wavelength among three models because the rupture breaks the entire width of the fault (~60 km; Figure 2.3). The initial elevation also has a broad and subdued peak (3.06 m). The large trench slip in this model is inefficient to produce sea surface elevation although significant horizontal displacement contribution is included. The rupture of model II stops at about 10 km down dip from the trench due to inelastic wedge deformation (Figure 2.4), leading to a slightly smaller wavelength of the initial sea surface elevation. One significant difference from model I is a clear peak (4.35 m) about 20 – 25 km wide on top of a broad signal in model II, which is caused by inelastic wedge deformation. This small-wavelength feature is important to generate impulsive tsunami, as will be shown below. The broad signal is controlled by the width of the rupture zone. The subsidence of these two models are quite similar. A sharp peak of about 25 km wide and 4.97 m high is seen in model III, which is due to 20 m buried slip on two 25 km wide subfaults (Figure 2.5d). Such large localized slip at shallow depths (3.5 – 7

16

km) generates a large narrow uplift, as well as a narrow subsidence nearly twice as large as that of models I and II, which is also clearly seen in the vertical seafloor displacement (Figure 2.6b). The elevation profile of model III is clearly narrower than that of model I and II. Although the uplift due to inelastic deformation is comparable in width in model II to that in model III the larger fault width (~50 km) leads to a larger dominant wavelength than model III. The along-strike extent of large uplift and subsidence in model III, also dominated by the two subfaults with localized slip, is about 100 km (Figure 2.5d). Models I and II have nearly uniform along-strike slip and inelastic deformation for about 200 km, extending from approximately 38.5°N to 40.2°N. We will see that these differences lead to different periods of tsunami signals and runup distributions on the Sanriku coast.

The efficiency of generating seafloor uplift in models II and III can be crudely compared as follows. The seafloor uplift in model III is mainly produced by 20 m localized buried slip on two subfaults (50 km x 25 km each). The seismic potency on these two subfaults is 2.5×10^{10} m^3. The seismic potency by inelastic deformation in the wedge in model II is 2.13×10^{10} m^3, which accounts for most of the uplift. Ignoring the small differences in peak seafloor uplift and different rupture lengths both models require similar potency to produce similar seafloor uplift, implying similar efficiency.

However, there may be a plausibility issue in model III associated with unrealistically large stress change in the overlying wedge (e.g., Geist & Dmowska, 1999). The shear strain on the fault in this kinematic slip model can be crudely calculated by slip divided by the width of the subfault, which is equal to 8.0×10^{-4}. Assuming a shear modulus of 10 – 30 GPa for sedimentary rocks the stress drop on the two subfaults is 8 – 24 MPa on average. Dynamic stress changes off the fault can be an order or more larger than this static estimate (e.g., Andrews, 2005). There are also stress

singularities at the edges of subfaults due to slip discontinuity. The depth of slip is shallow (~ 3.5 – 7 km), which is essential to generate large uplift in this model. Due to low confining pressure, possible fluid overpressure, and weak sediments in the wedge such large stress changes may cause wedge failure leading to inelastic deformation, similar to model II. Thus, despite generating short-wavelength seafloor uplift efficiently large localized buried slip on shallow narrow subfaults may be mechanically implausible. This issue may need further investigations.

2.4. Results

We show the snapshots of tsunami due to model II when wave dispersion is included (Figure 2.7). As the tsunami propagates towards the coast tsunami speed decreases due to decreasing ocean depth. Clear narrowing of wavelength and increase of wave amplitude is seen, which is the well-known shoaling effect. Small dispersive signals can be seen after the leading tsunami due to the small wavelength of uplift relative to ocean depth in the model. Such narrow-wavelength leading tsunami will be manifested as impulsive signals in time histories, to be shown below. Shortly after 30 minutes tsunami starts to impact the Sanriku coast with large wave amplitude. Edge waves as energy trapped near the shore last long after the leading tsunami hits the coast. Tsunami propagating into deep ocean shows the opposite effect. The increase of ocean depth increases wave speed and tsunami wavelength and decreases the wave amplitude. Strong wave dispersion is evident. The dispersion in deep ocean due to long travel distance has been shown by several studies (e.g., Horrillo et al., 2006; Saito et al., 2014; Baba et al., 2015; Tanioka et al., 2018). Here the strong dispersion is largely due to the small wavelength of seafloor uplift relative to ocean depth.

The wavefield without dispersion for model II is much simpler (Supplemental Figure 2.1). The leading tsunami toward the coast is similar to Figure 2.7 although stronger shoaling effects can be seen. The increase of wave amplitude and narrowing of leading tsunami are slightly more significant. The wave amplitude in deep ocean is significantly higher than that with dispersion. The snapshots of wavefield with and without dispersion for models I and III (Supplemental Figures 2.2 – 2.5) show similar patterns.

The waveforms with and without dispersion at five offshore stations (TM1, TM2, and Iwate N, M, and S) and one Deep-ocean Assessment and Reporting of Tsunami (DART) station (21418) are shown in Figure 2.8. The data recorded in the 2011 Tohoku earthquake at these stations (Figure 2.2) are high-pass filtered at 15 minutes to take out the impulsive signal by removing the long-period components caused by the broad seafloor uplift south of 39°N, shown as a reference. We do not aim to fit the 2011 data in this work as the simulations are for the 1896 Sanriku tsunami. Our focus here is more on the amplitude and wavelength of seafloor uplift necessary to generate the signal similar to the impulsive signal observed in 2011. The timing of the filtered data is arbitrary (i.e., not with respect to the origin time of the three models). At five nearshore stations a clear impulsive signal of the leading tsunami is seen, which is not significantly affected by the dispersion. The impulsive signal without dispersion is slightly larger and narrower than the dispersive signal because dispersion tends to smooth out the wave field. Both nondispersive and dispersive impulsive signals show a remarkable similarity to the impulsive signals observed in the 2011 Tohoku tsunami in terms of impulse width and amplitude, which is due to the small wavelength of seafloor uplift in model II. The observed signals in 2011 show slightly narrower width, suggesting that the wavelength of model II needs to be reduced if the 2011 data is to be fitted, which can be achieved by narrowing the fault width. The smaller amplitude of the data at

Iwate N indicates that rupture extent of the 2011 Tohoku earthquake may not reach as far north as in model II or the seafloor uplift in the north was smaller than in model II. At DART 21418, the observed signal shows clear wave dispersion, which is well reproduced by the dispersive model, as shown by previous studies (e.g., Saito et al., 2014; Tappin et al., 2014; Baba et al., 2015). The nondispersive model oversimplifies the waveform and significantly overestimates the tsunami amplitude in deep ocean. Waveform comparisons with and without dispersion for models I and III are shown in Supplemental Figures 2.6 and 2.7, displaying similar patterns.

We compare the waveforms at all stations for the three dispersive models (Figure 2.9). The width of the impulsive signal in model I is the largest among three models because model I has the longest wavelength of initial sea surface elevation (Figures 2.5 and 2.6). The initial sea surface elevation in model I is the smallest of the three models, resulting in that model having the smallest amplitude of the impulsive signal at four of five offshore stations. At Iwate N, the impulsive signal of Model III is the smallest because this model has a shorter rupture extent (Figure 2.5c). Model II produces more impulsive signal and larger wave amplitude than model I at all stations due to the smaller wavelength and larger total seafloor uplift. The most impulsive signal is seen in model III, which has the shortest wavelength due to large localized buried slip on 25 km wide subfaults, but may be mechanically implausible as mentioned earlier. This model also generates the largest tsunami height at four of five offshore stations due to larger seafloor uplift and a smaller rupture extent (Figure 2.5c). The waveform comparison for three nondispersive models (Supplemental Figure 2.8) shows narrower impulsive signals than the dispersive results, consistent with Figures 2.8, Supplemental Figure 2.6 and 2.7, and the patterns among three models are similar.

The maximum tsunami heights of three dispersive models are illustrated in Figure 2.10. Model II produces overall larger tsunami heights than model I, which is consistent with the

waveforms shown in Figure 2.9. Model III has the largest tsunami height between about 39°N and slightly south of 40°N because the initial sea surface elevation is concentrated above the two-central subfaults with large localized buried slip. Clear focusing of wave energy is seen, generating large tsunami heights on the Sanriku coast south of 40°N. This model, however, generates smaller tsunami height north of 40°N due to its shorter along-strike extent of seafloor uplift than models I and II (see also the waveform at Iwate N in Figure 2.9). The maximum tsunami height for the three nondispersive models (Supplemental Figure 2.9) show similar patterns landward with slightly larger amplitudes than the dispersive models. The peak tsunami amplitude in deep ocean is significantly overestimated and unrealistic due to the exclusion of dispersion.

Table 2.1. The root-mean-square (rms) of simulated runups at all locations in the models and ratios of simulated to observed runup at the observation sites

		rms of simulated runup (m)	rms of ratio of simulated to observed runups
Model I	nondispersive	6.71	0.92
	dispersive	6.56	0.91
Model II	nondispersive	8.23	1.04
	dispersive	7.60	1.01
Model III	nondispersive	7.42	0.84
	dispersive	7.50	0.85

Finally, tsunami runup along the Sanriku coast for the three models without and with dispersion are shown in Figures 2.11 and 2.12, respectively. All the simulated runup values in the three models are shown. In order to compare the three models clearly, the runup values are shaded and outlined by a peak envelope function in each model, which is obtained by spline interpolation of local maxima over 20 points. The runup data of the 1896 Sanriku tsunami collected at 144 sites

by Iki (1897) and 266 sites by Matsuo (1933) are also shown. The root-mean-square (rms) of runup heights at all locations in the three models with and without dispersion are listed in Table 2.1. The table also lists the rms of the ratios of simulated to observed runup heights at the observation sites of Iki (1897) and Matsuo (1933). The data at which the simulated runup does not exist (i.e., simulated tsunami does not reach the observation point) is not included in the calculation. The comparison of simulated runup (with and without dispersion) with data in each model is detailed in Supplemental Figures 2.10 – 2.12.

Nondispersive models in general generate slightly larger runup than dispersive models with a possible exception of Model III (see also Supplemental Figures 2.10 – 2.12), consistent with distributions of maximum tsunami height (Figures 2.10 and Supplemental Figure 2.9). The differences in the runup of model III with and without dispersion appear indistinguishably small. Model II produces consistently larger runup than model I although the two runup patterns are similar, which can also be seen in the rms of simulated runups (Table 2.1). The difference in runup between these two models can be well above 5 m (Figures 2.11d – f and 2.12d – f) although the difference in the initial sea surface elevations is slightly above 1 m, illustrating the stronger shoaling effect and the amplification of small-wavelength tsunami by the bathymetry and coastal topography of the Sanriku coast.

The runup of model II show a remarkable similarity to the 1896 runup data, especially in the overall trend of runup distribution. The largest tsunami runup observed in the 1896 Sanriku tsunami, 38.2 m in Ryori-Shirohama (141.8071°E, 39.0569°N), is nearly reproduced by both the nondispersive and dispersive models with a slightly better match in the nondispersive model. The rms of the ratios of simulated to observed runup heights is 1.04 (without dispersion) and 1.01 (with

dispersion), better than the other two models. These remarkable fits are obtained without any tuning of the model.

Model III significantly overestimates the runup height between about 39.3°N and 39.9°N, which is about the same region with large peak tsunami height in Figure 2.10. The model underestimates the runup elsewhere, including the large runup in Ryori-Shirohama, due to its shorter along-strike extent of seafloor uplift, which results in the rms of the ratios of simulated to observed runups less than 1.0 in this model.

2.5. Discussion and Conclusions

We have presented three models of the 1896 Sanriku tsunami by using two dynamic rupture models and one kinematic slip model of the 1896 Sanriku earthquake. The short-wavelength seafloor uplift is shown instrumental in generating impulsive tsunami, which can be greatly amplified by the rugged coast of Sanriku to produce large runup. We show that the inelastic wedge deformation model (Model II), with width of seafloor uplift about 20 – 25 km, produces impulsive tsunami similar to what was observed at two ocean-bottom pressure sensors (TM1 and TM2) and three GPS wave gauges (Iwate N, M, and S) offshore the Sanriku coast in the 2011 Tohoku tsunami. Our focus is not to fit the 2011 tsunami data as the simulations are for the 1896 Sanriku tsunami, but to show a physical mechanism capable of generating such short-wavelength seafloor uplift and impulsive tsunami.

Despite Model III (a kinematic slip model with elastic dislocation) can also generate short-wavelength seafloor uplift efficiently this model may be mechanically implausible; the large stress changes in the overriding wedge can likely cause failure leading to inelastic deformation, similar to model II. The physical plausibility of model III may need further investigations. This model

also produces a worse fit to the observed runup of the 1896 Sanriku tsunami than the other two models. Large trench slip with mostly elastic wedge deformation (model I) produces broader and smaller seafloor uplift largely due to the shallow dipping fault geometry, giving rise to smaller and longer-period tsunami than the other two models.

Inelastic wedge deformation (model II) produces consistently larger tsunami heights than large shallow slip (model I), because the former model produces larger seafloor uplift and shorter wavelength than does the latter. The difference in runup between these two models can be more than five times the difference in the initial sea surface elevations due to the acute sensitivity of runup to short tsunami wavelengths and stronger shoaling effect of short-period tsunami. This model also produces runup on the Sanriku coast with a remarkable similarity to the observed runup of the 1896 Sanriku tsunami without any tuning of the model.

The 1896 Sanriku earthquake is a tsunami earthquake (Kanamori, 1972), which caused weak high-frequency seismic radiation and large tsunami. Inelastic wedge deformation is a large energy sink and generates seafloor uplift efficiently, which can explain both the characteristics of tsunami earthquakes (Ma, 2012; Ma & Hirakawa, 2013). In this work, we extend the models of Ma & Nie (2019) and further show that short-wavelength inelastic seafloor uplift can produce impulsive tsunami to be amplified on the Sanriku coast, resulting in large runup. Thus, inelastic wedge deformation is a possible mechanism that can account for nearly all the important characteristics of the 1896 Sanriku earthquake. Fully coupled models of dynamic rupture and tsunami (e.g., Lotto et al., 2018; Wilson & Ma, in review) for the 1896 Sanriku earthquake should be done next to more rigorously model tsunami excitation and explore the radiation characteristics of seismic and ocean acoustic waves due to inelastic deformation, which can provide important insights to tsunami early warning in the Japan trench margin.

No large shallow slip near the trench or large submarine landslide were observed north of 39°N in the 2011 Tohoku earthquake (Fujiwara et al., 2017). Given the similarity of tsunami runup generated by the 1896 Sanriku and 2011 Tohoku earthquakes and the capability of inelastic wedge deformation in generating impulsive tsunami, large tsunami runup, and deficient high-frequency seismic radiation we suggest, as an alternative to shallow-slip models, that the devastating 2011 Tohoku tsunami on the Sanriku coast may be caused by inelastic wedge deformation north of 38.5°N due to the presence of thick sediments (e.g., Tsuru et al., 2002; Kodaira et al., 2017).

Chapter 2, in full, is a reprint of the material as it appears in Journal of Geophysical Research: Solid Earth, 2021, Du, Yue; Ma, Shuo; Kubota, Tatsuya; Saito, Tatsuhiko, American Geophysical Union, 2021. The dissertation author was the primary investigator and author of this material.
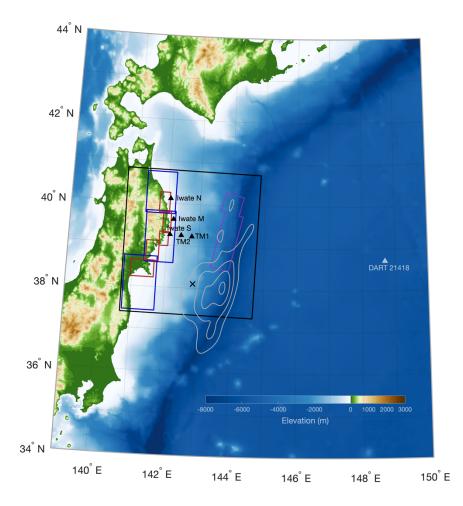
Figure 2.1. Map of the computational domain. Four nested grid layers are used. The outmost grid layer uses 1350 m grid spacing with 974 x 1370 grid cells, covering the entire computational domain (larger than shown here). The black rectangle shows the 450 m grid. Three overlapping blue rectangles denote the 150 m grid. The 50 m grid is shown by five red overlapping rectangles, covering the Sanriku coast in high resolution. The six triangles denote the stations used in this study. The cross symbol marks the epicenter of the 2011 Tohoku earthquake. The contours are the initial sea surface elevation model of Saito et al. (2014) for the 2011 Tohoku tsunami. The magenta lines outline the surface projection of the fault plane used in Satake et al. (2017) for the 1896 Sanriku earthquake, which is model III of this work.
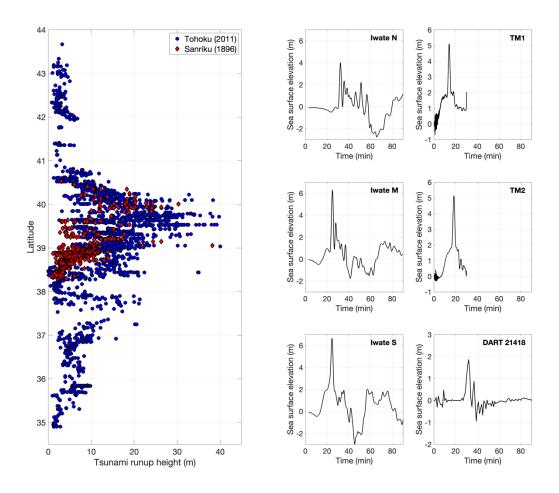
Figure 2.2. (left) Comparison of observed tsunami runup heights in the 1896 Sanriku earthquake (Iki, 1897; Matsuo, 1933) and 2011 Tohoku earthquake (Mori et al., 2011). Both earthquakes produced large runups up to 40 m on the Sanriku coast despite different earthquake magnitudes. The 2011 tsunami height is consistently larger on the Sanriku coast more than 100 km north of the epicenter (38.1°N). (right) Observed tsunami waveforms at six stations (shown in Figure 2.1) in the 2011 Tohoku earthquake. Five stations offshore of the Sanriku coast recorded a rare impulsive signal atop a broad regional signal. A deep-sea buoy station (DART 21418) recorded clear dispersive tsunami. The physics of producing these signals is addressed in this work.
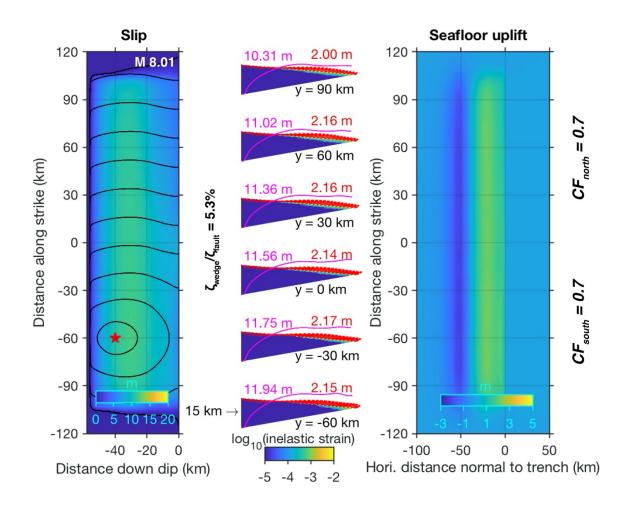
Figure 2.3. The large shallow slip model and model I of this work. Left panel shows the slip distribution on the fault with moment magnitude shown on the upper right corner and rupture time contours every 10 s. The middle panel shows the final seafloor displacement (red arrows), on-fault slip (magenta curves), and inelastic shear strain at six cross sections (y is distance along strike). The numbers in red and magenta denote the peak uplift and slip, respectively, at each cross section. The ratio of seismic potency in the wedge to the fault is shown between the first two panels. The right panel shows the surface map of final vertical seafloor displacement. Figure from Ma & Nie (2019). CF: closeness-to-failure.
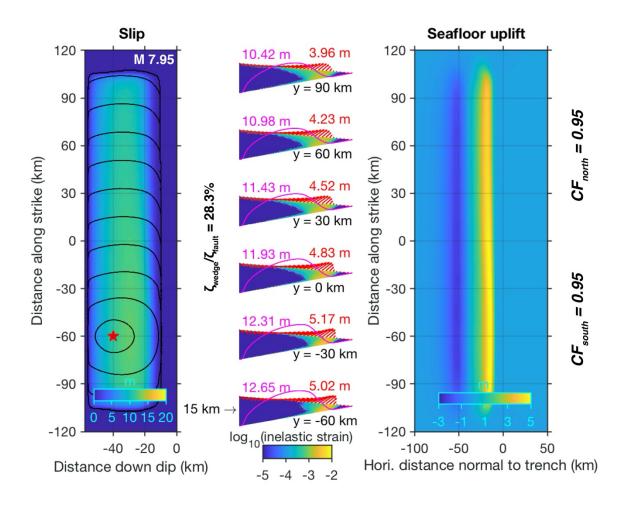
Figure 2.4. The inelastic wedge deformation model and model II of this work. Similar to Figure 2.3. The inelastic wedge deformation produces large and narrow seafloor uplift landward from trench with diminishing shallow slip. Figure from Ma & Nie (2019). CF: closeness-to-failure.
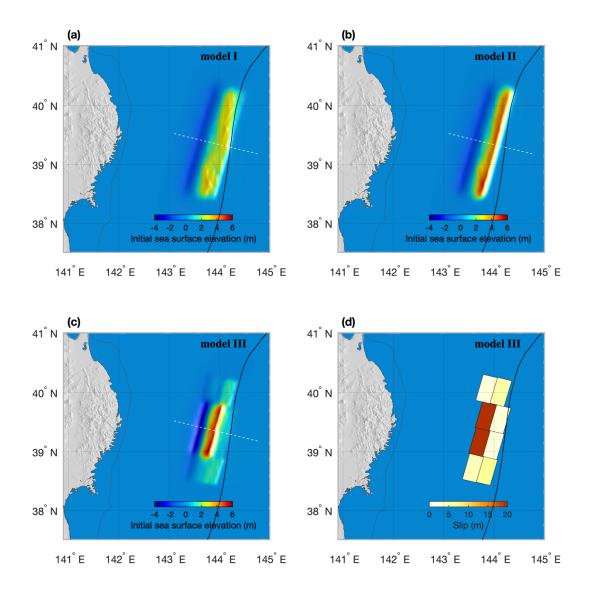
Figure 2.5. (a, b, c) Comparison of initial sea surface elevations among three models of the 1896 Sanriku tsunami in this study. Model III is the final model of Satake et al. (2017). The slip distribution of this model is shown in (d). The white dashed line marks the cross section shown in Figure 2.6.
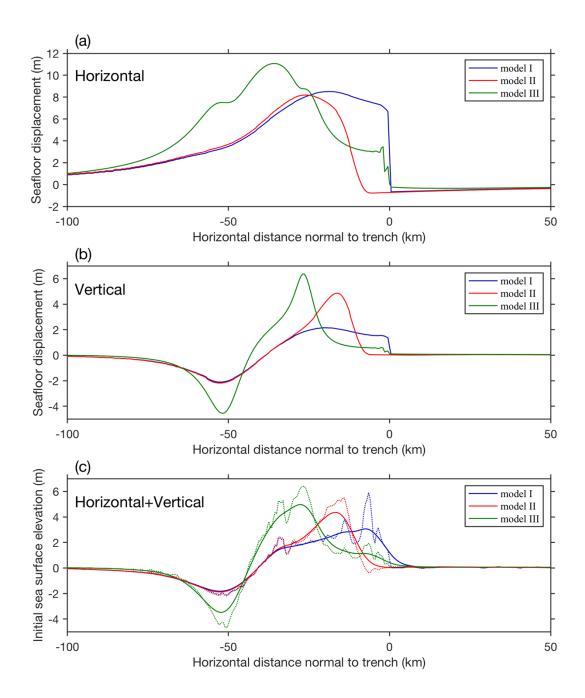
Figure 2.6. Comparisons of (a) horizontal seafloor displacements, (b) vertical seafloor displacements, and (c) initial sea surface elevations at a cross section shown in Figure 2.5. The contribution of horizontal seafloor displacement is included in the calculation of initial sea surface elevation in (c). The unfiltered initial sea surface elevations (dotted lines) contain many small-wavelength variations, which cannot exist due to the nonhydrostatic ocean response. The solid lines show the initial sea surface elevation after applying a Kajiura lowpass filter with a cutoff wavelength of 4 km. The horizontal seafloor displacement contributes significantly to initial sea surface elevation in model I (within 30 km from the trench), but not in the other two models.

32
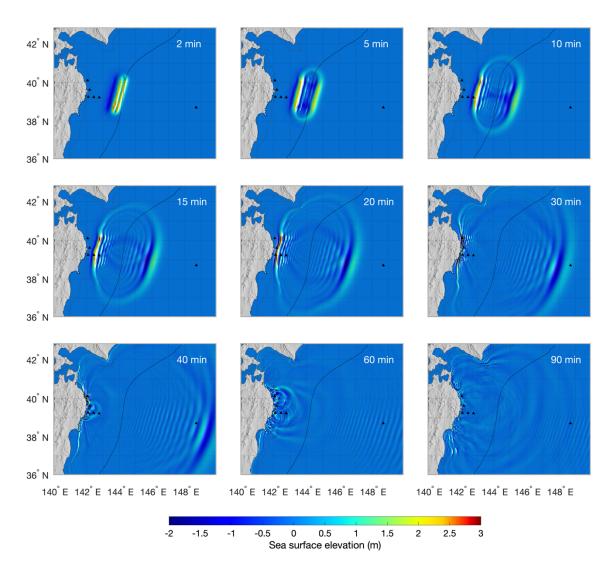
Figure 2.7. Snapshots of sea surface elevation for model II with dispersion. Clear wave shoaling effect is seen on the landward tsunami, with increasing amplitude and decreasing wavelength as tsunami slows down. The tsunami recorded at five stations (shown by black triangles) off the Sanriku coast with impulsive signals are shown in Figure 2.8. Seaward tsunami shows strong wave dispersion largely due to small wavelength of seafloor uplift relative to ocean depth, which is recorded at DART 21418.
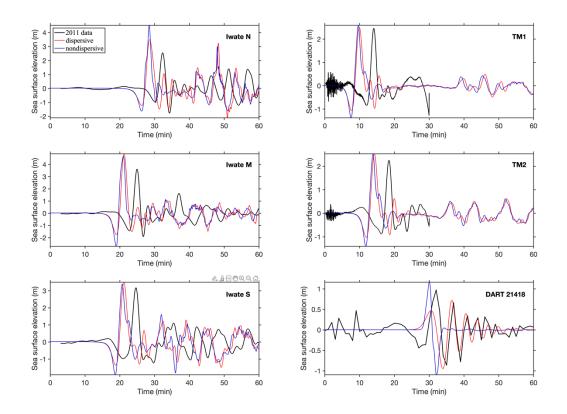
Figure 2.8. Comparison of simulated waveforms at six stations with (red) and without (blue) dispersion for model II. The observed data (Figure 2.2) high-pass filtered with a 15-minute cutoff period are shown in black for reference. We do not intend to match the 2011 data because the simulations are for the 1896 Sanriku tsunami. The timing of the 2011 data is arbitrary. Both nondispersive and dispersive waveforms show a clear impulsive signal, similar to the observed signal in 2011. Dispersion effects for the five offshore stations are minor. The dispersive impulsive signal is slightly wider and smaller than the nondispersive signal. At DART 21418 the nondispersive waveform is significantly oversimplified.
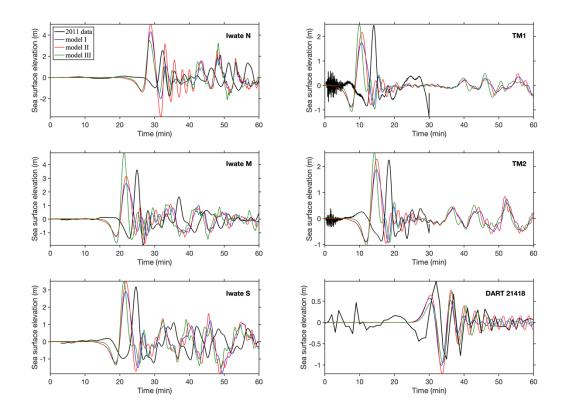
Figure 2.9. Comparison of simulated waveforms from three dispersive models. Model I produces the smallest and widest impulse at four of five offshore stations due to its smallest and longest-wavelength initial sea surface elevation (Figure 2.6). Model III produces the smallest amplitude at Iwate N because of its shorter along-strike extent of seafloor uplift (Figure 2.5).The impulsive signal in Model II is consistently larger and narrower than model I. Model III produces the narrowest impulse due to its shortest wavelength among three models, however, may contain mechanical inconsistencies at the earthquake source.
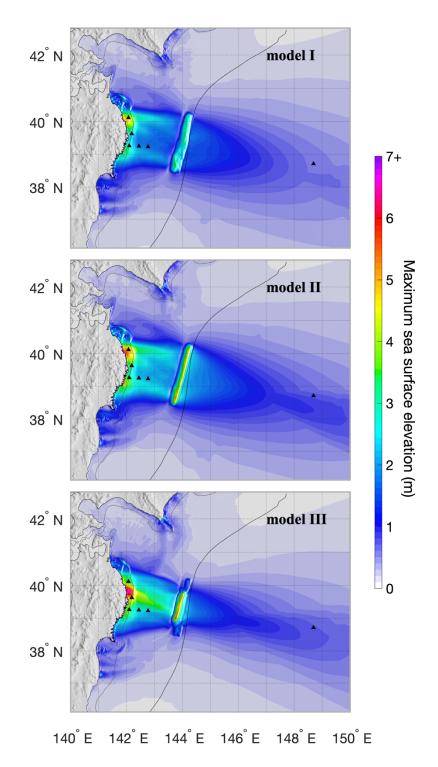
Figure 2.10. Comparison of maximum sea surface elevation for three dispersive models. Model II generates consistently larger tsunami height than model I. The localized slip and uplift of model III produce large tsunami height between about 39°N and 40°N. The 200 m depth contour by a thin grey line shows approximately the width of continental shelf.

Figure 2.11. Comparison of runup from three nondispersive models of the 1896 Sanriku tsunami. (a) All the runup values along the coast calculated from three models compared with the data of Iki (1897) and Matsuo (1933), (b) map of the Sanriku coast with the maximum sea elevation of model II, (c – f) enlarged view of comparison in (a) on four segments with a shaded region outlined by an envelope function for each model. Each envelope function is determined using spline interpolation over local maxima separated by 20 points. A remarkable similarity between the runup of model II and data can be seen. Model II produces consistently larger runup than model I. Model III overestimates the runup between about 39.3°N and 39.9°N and underestimate the runup elsewhere.
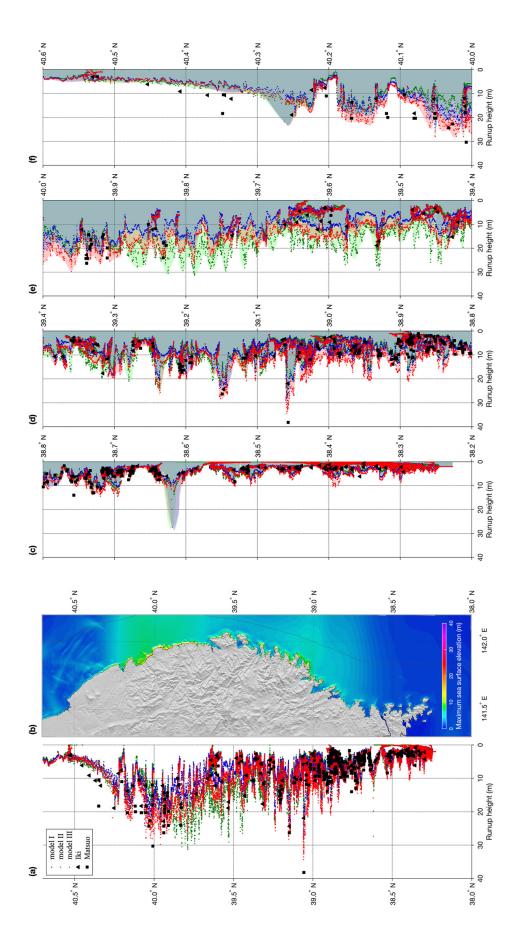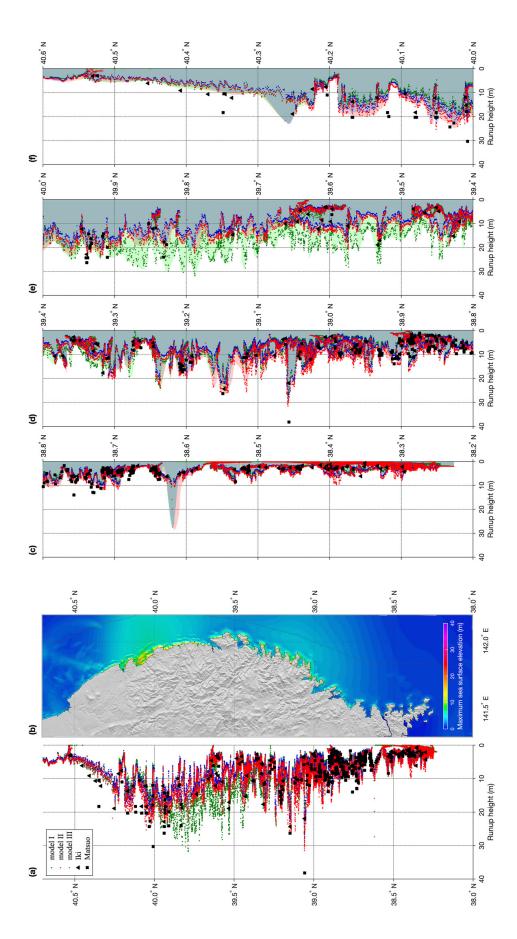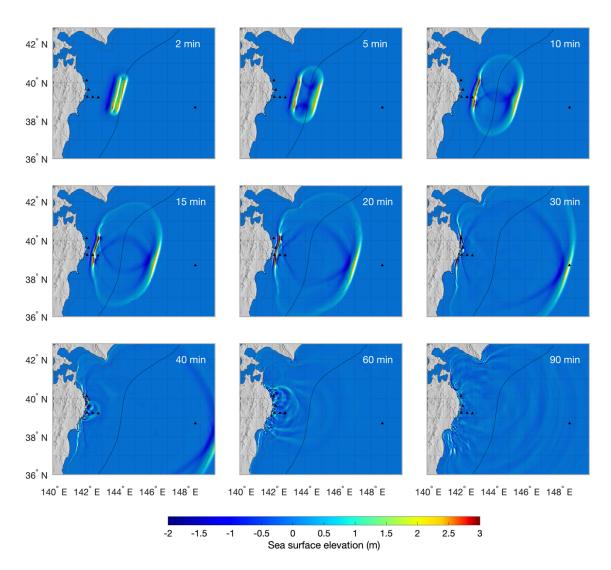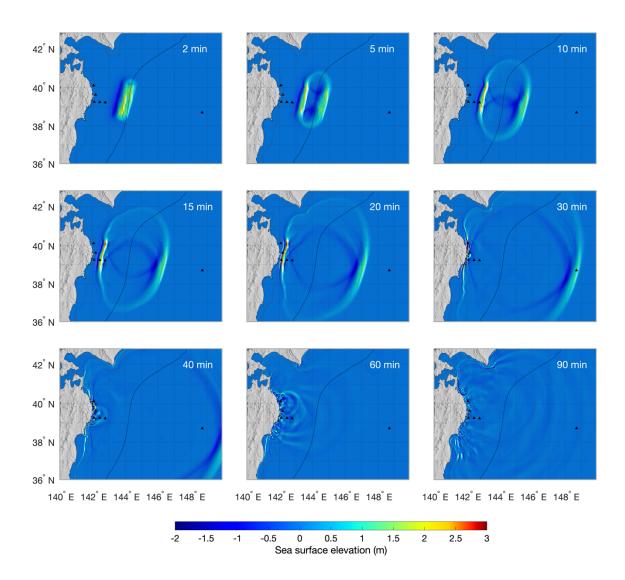
Figure 2.12. Similar to Figure 2.11, but for three dispersive models. The modeled runups are slightly smaller than in Figure 2.10. Similar patterns among three models can be seen.
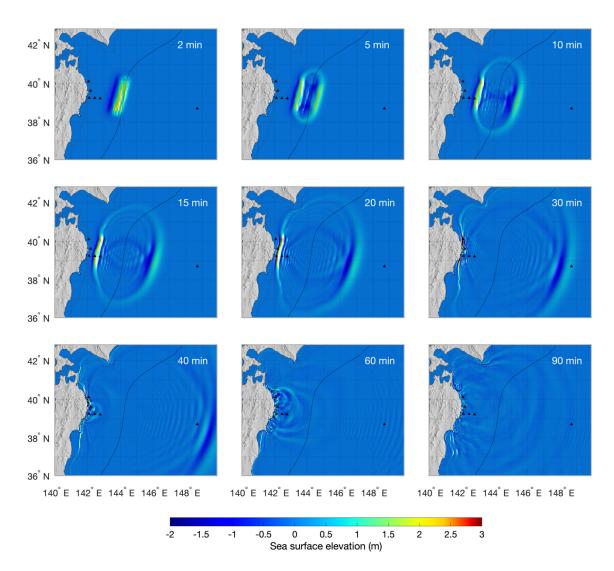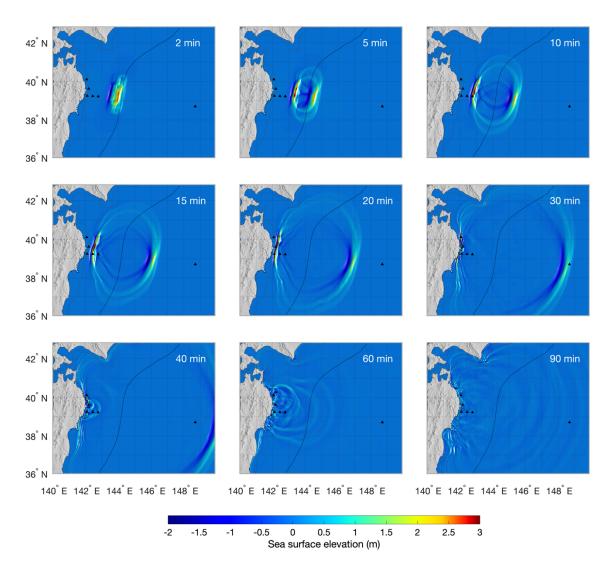
Supplemental Figure 2.1. Similar to Figure 2.7, but for model II without dispersion.
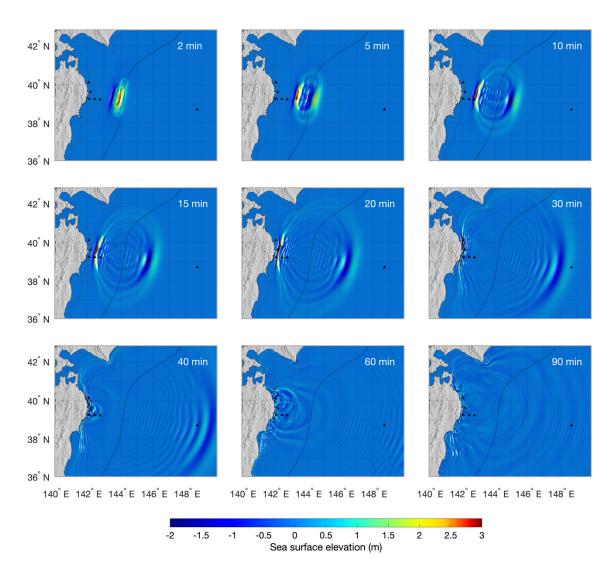
Supplemental Figure 2.2. Similar to Figure 2.7, but for model I without dispersion.
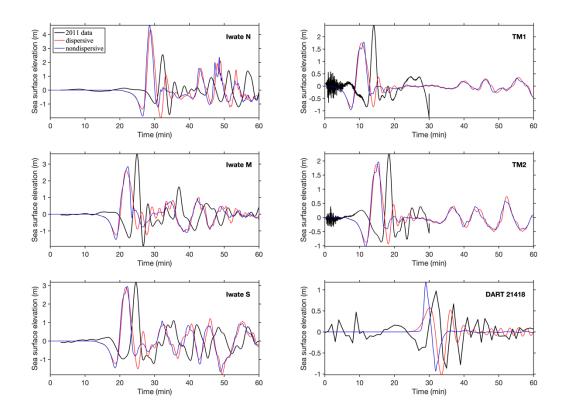
Supplemental Figure 2.3. Similar to Figure 2.7, but for model I with dispersion.
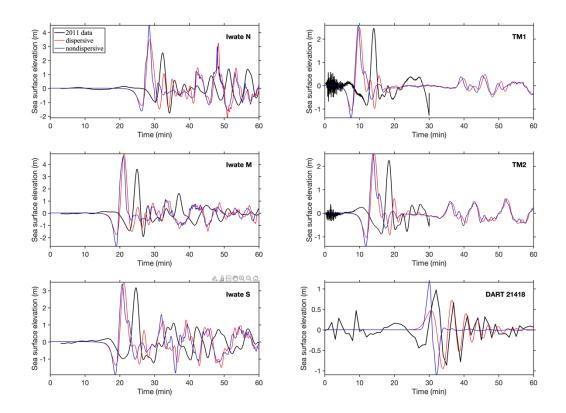
Supplemental Figure 2.4. Similar to Figure 2.7, but for model III without dispersion.
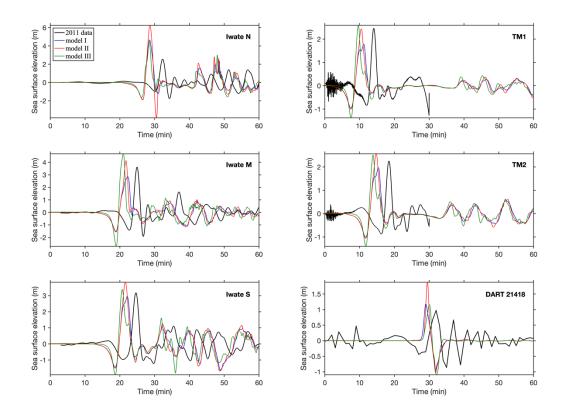
Supplemental Figure 2.5. Similar to Figure 2.7, but for model III with dispersion.
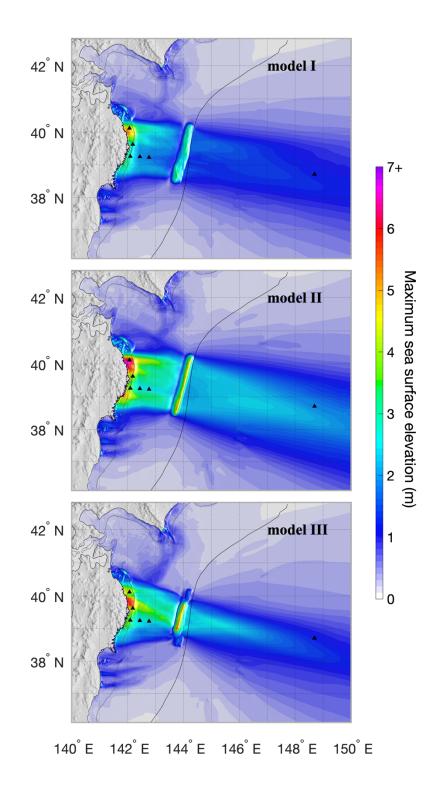
Supplemental Figure 2.6. Similar to Figure 2.8, but for model I.
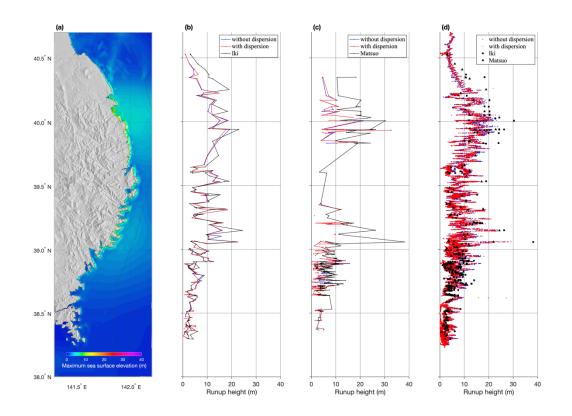
Supplemental Figure 2.7. Similar to Figure 2.8, but for model III.
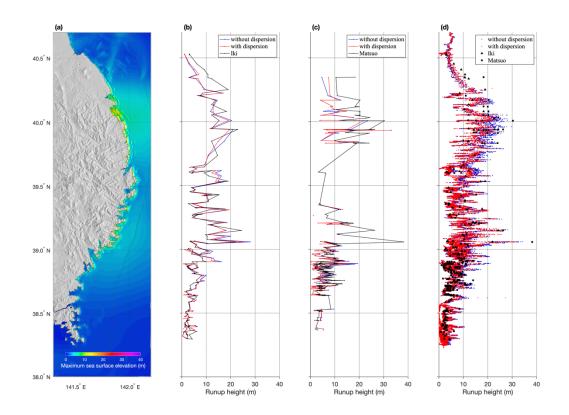
Supplemental Figure 2.8. Similar to Figure 2.9, but for three nondispersive models.
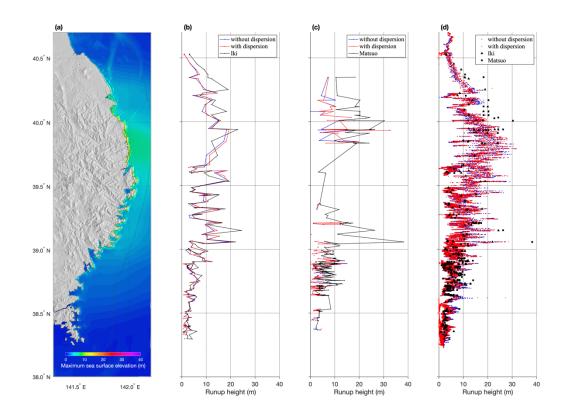
Supplemental Figure 2.9. Similar to Figure 2.10, but for three nondispersive models.

Supplemental Figure 2.10. Comparison of runup from model I with and without dispersion. (a) Map of the Sanriku coast with the maximum sea elevation of the model with dispersion, (b) the data of Iki (1897) compared with simulated runups at the observation locations, (c) the data of Matsuo (1933) compared with the simulated runups, (d) all the runup values along the coast calculated from dispersive and nondispersive models compared with the data of Iki (1897) and Matsuo (1933). Nondispersive model in general produces slightly larger runup.

Supplemental Figure 2.11. Similar to Supplemental Figure 2.10, but for the comparison of model II with and without dispersion.

Supplemental Figure 2.12. Similar to Supplemental Figure 2.10, but for the comparison of model III with and without dispersion.

Chapter 3

Wedge Inelasticity and Fully Coupled Models of Dynamic Rupture, Ocean Acoustic Waves, and Tsunami in the Japan Trench: 1. The 2011 Tohoku-Oki Earthquake

Abstract

Along-strike variation of sediment thickness and inelastic wedge deformation can significantly affect the variations of near-trench slip, seismic radiation, and tsunamigenesis along the Japan Trench. We present fully coupled models of dynamic rupture, ocean acoustic waves, and tsunami for large tsunamigenic earthquakes in this subduction zone, to fully investigate the physics of tsunami generation and radiation field. In part 1, we focus on the 2011 M_W 9.1 Tohoku-Oki earthquake. Part 2 addresses the 1896 Sanriku earthquake. We extend a dynamic rupture model of the 2011 Tohoku-Oki earthquake that incorporated wedge inelasticity by including a compressible ocean. The fully coupled models produce tsunami in good agreement with that from a dispersive shallow-water model, confirming the validity of both models. We show strong radiation of ocean acoustic and seismic waves caused by fast rupture velocity (~3 km/s) and large near-trench slip south of 39°N, dominated by elastic wedge response. However, north of 39°N where sediment thickens in the northern Japan Trench, the inelastic wedge deformation excites tsunami efficiently with diminishing near-trench slip (<20 m), consistent with differential bathymetry observations, but causes slow rupture velocity (~850 m/s) and significantly weaker radiation of ocean acoustic and seismic waves. Inelastic wedge deformation thus provides a self-consistent interpretation to both depletion in high-frequency radiation and large tsunami generation in the northern Japan Trench, which may challenge the use of ocean acoustic waves for robust tsunami early warning.

3.1. Introduction

A controversy about the 2011 M_W 9.1 Tohoku-Oki earthquake and tsunami arose shortly after the disasters unfolded, which centers on the physics of tsunami generation and particularly why the largest tsunami (up to 40 m) occurred >100 km north of large slip region updip from the hypocenter (e.g., Mori et al., 2011). Most slip models based on seismic and geodetic data resolved large slip updip from the hypocenter (Sun et al., 2017; Lay, 2018; Uchida & Bügurman, 2021; and references therein), confirmed by the differential bathymetry data before and after the earthquake showing >50 m slip near the trench around 38.1°N (Fujiwara et al., 2011) and seafloor geodesy data (e.g., Sato et al., 2011; Kido et al., 2011). These slip models can explain the large tsunami inundation distances in Sendai and Ishinomaki Plains, however, resolved little slip north of 39°N, incapable of explaining the large tsunami generation in the northern Japan Trench (e.g., MacInnes et al., 2013).

To explain the large tsunamigenesis in the northern Japan Trench, slip models by inverting tsunami data requires near-trench slip up to 36 m north of 39°N (e.g., Satake et al., 2013; Yamazaki et al., 2018). However, the differential bathymetry data in the northern Japan Trench (Fujiwara et al., 2017, 2021; Kodaira et al., 2020, 2021; Zhang et al., 2023) showed the trenchward coseismic horizontal displacement <20 m invalidating these models. A large submarine landslide for tsunami generation (Tappin et al., 2014) is also ruled out by the differential bathymetry data.

Nearly all the slip models for this earthquake are based on elastic dislocation theory, which requires large shallow slip to explain tsunami generation (e.g., Satake and Tanioka, 1999; Lay et al., 2012). Despite being inconsistent with the differential bathymetry data in the northern Japan Trench large shallow slip is still the prevailing hypothesis in explaining the 2011 tsunami and large

tsunami runup north of 39°N and has been widely used to explain tsunamigenesis around the globe (e.g., Cheung et al., 2021).

A different and opposing hypothesis was proposed by Ma & Nie (2019) and Ma (2023), which resorts to inelastic wedge deformation (Ma, 2012; Ma & Hirakawa, 2013). They questioned the application of the elastic dislocation theory in the northern Japan Trench, where weak and thick sediments are present in the frontal prism (Tsuru et al., 2002; Kodaira et al., 2017). Figure 3.1 shows the variation of width of sediment along the Japan Trench based on the data of Tsuru et al. (2002). With weak sediments large dynamic stresses during rupture propagation can drive the wedge into failure, making the elastic dislocation theory inapplicable. We refer the reader to Ma & Nie (2019), Wilson & Ma (2021), Du et al. (2021), and Ma (2023) for more discussions of the applicability of elastic dislocation theory in shallow subduction zones. Inelastic deformation of overriding wedge, mimicking frictional sliding on Coulomb microfractures with steeper dips, can efficiently generate seafloor uplift on a shallowly dipping plate interface with diminishing shallow slip. Ma (2023) showed that the along-strike variation of sediment thickness and inelastic deformation in the northern Japan Trench can explain the large shallow near-trench slip (>50 m) around 38.1°N and large tsunami generation with diminishing shallow slip (< 20 m) north of 39°N, providing a self-consistent explanation to the puzzling >100 km distance offset mentioned above while being consistent with the differential bathymetry observations (Fujiwara et al., 2011, 2017, 2021; Kodaira et al., 2020, 2021). The inelastic deformation of the model produces short-wavelength uplift, generating impulsive tsunami that matches the amplitude, arrival time, and pulse width of the tsunami observed offshore the Sanriku coast (e.g., Maeda et al., 2011), which can be instrumental in leading to extreme runup in the rugged Sanriku coast due to amplification

of short-wavelength components (e.g., Shimozono et al., 2014; Tappin et al., 2014; Yamazaki et al., 2018; Du et al., 2021).

It is important to further test these two hypotheses, as the seemingly puzzling observations may illuminate the physics of tsunami generation. One way to do so is to examine the radiation characteristics of elastic dislocation models and models with significant inelastic wedge deformation. Since Kanamori (1972) identified tsunami earthquakes as earthquakes that generate disproportionately large tsunamis relative to their surface wave magnitude (M_S) depletion in high-frequency radiation had been recognized as one of the essential characteristics of tsunami earthquakes. Over the last 50 years, depletion in high-frequency radiation is also recognized as an important rupture characteristic in the upper ~10 – 15 km of rupture zone in large tsunamigenic earthquakes worldwide (e.g., Lay et al., 2012). Some related and important characteristics of earthquakes associated with large tsunamigenesis include anomalously slow rupture propagation and low moment-scaled radiated energy (Newman & Okal, 1998). Lay et al. (2012) classified the upper 10 – 15 km as Domain A for global subduction zones, a domain associated with anomalously large tsunami generation and depletion in high-frequency radiation. (They associated Domain A with large slip, which is questionable because large tsunami can be generated with diminishing slip as observed in the northern Japan Trench. The classification also ignored important along-strike rupture variations, such as in the 2011 Tohoku-Oki earthquake and many other tsunamigenic earthquakes, e.g., the 2004 Sumatra earthquake.)

Yet, depletion in high-frequency radiation is not well understood and largely unaccounted for in most kinematic and dynamic rupture models of large tsunamigenic earthquakes. Most models focused only on tsunami generation by shallow slip in the realm of elastic dislocation

theory. Perhaps it is not surprising that slip models using seismic data failed to detect slip north of 39°N because of anomalous depletion in high-frequency radiation associated with large tsunami generation. The lower seismic intensity observed in Iwate Prefecture than Miyagi and Fukushima Prefectures to the south (locations denoted in Figure 3.1), shown in Figure 1 of Kodaira et al. (2021), is also consistent with depletion in high-frequency radiation in the north. The 1896 Sanriku earthquake, one of the most anomalous tsunami earthquakes, also occurred in the northern Japan Trench, which strongly suggests that the same physics may lead to large tsunami generation and depletion in high-frequency radiation in both events.

How do we understand large tsunami generation and depletion in high-frequency radiation in shallow subduction zones as a whole? Noda & Lapusta (2013) argued that thermal pressurization of pore fluids in the fault zone can weaken the fault, leading to large slip and long slip duration, which may apply to the 2011 Tohoku-Oki earthquake and 1999 ChiChi earthquake. However, their model was in a whole space. The rapid stress drop in their model seems unable to explain the long-period observations. Kubota et al. (2022) showed that tsunami data ruled out the possibility of thermal pressurization updip from the hypocenter; large shallow slip is driven mostly by deep large stress drop enhanced by the free surface. Ma & Hirakawa (2013) showed the importance of the free surface in enhancing depletion in high-frequency radiation as it unclamps the fault and causes large strength drop. Yin & Denolle (2021) showed similar results. However, the free surface alone should not account for the full physics for depletion in high-frequency radiation. Meng & Duan (2023) showed that along-strike frictional heterogeneities (Bilek & Lay, 2002) may lead to slow rupture propagation, depletion in high-frequency radiation, and low moment-scaled radiated energy. This mechanism is promising, but the radiation from their model may need to be examined because locally large stress drops on velocity-weakening patches

surrounded by velocity-neutral or velocity-strengthening patches (similar to seamount rupture modelled by Duan, 2012) may lead to more high-frequency radiation. All these models are elastic (except for Ma & Hirakawa, 2013) and require large shallow slip to explain tsunami generation.

Many early studies (e.g., Okal,1988; Kanamori & Kikuchi, 1993; Satake and Tanioka, 1999; Polet & Kanamori, 2000) attributed anomalous depletion in high-frequency radiation and tsunamigenesis to sediment in the fault zone. A recent study can be seen in Sallarès & Ranero (2019). They argued if seismic moment is fixed the low rigidity of sediment increases slip, therefore increasing seafloor displacement and tsunami generation, which may be oversimplified. To explain depletion in high-frequency radiation most studies attributed to slow rupture velocity, again due to low rigidity of sediment. However, in a low-velocity fault zone rupture velocity is not controlled by the sediment, instead it can be controlled by the material outside the fault zone. Trapped waves within the low-velocity fault zone can inevitably lead to more high-frequency radiation and sometime to supershear rupture velocities (Harris & Day, 1997). Lotto et al. (2017) modelled dynamic rupture propagation in the presence of a large sedimentary prism and found that sediment leads to slow rupture propagation and large slip, similar to Ma & Beroza (2008) and the elastic model in Ma (2023). However, dynamic rupture on a bimaterial interface may inevitably lead to large, rapid strength drop and slip velocities enhanced by the free surface (Ma & Beroza, 2008; Scholtz, 2014), leading to more high-frequency radiation.

One mechanism that can reconcile probably all the anomalous observations of shallow subduction earthquakes is inelastic deformation (Ma, 2012; Ma & Hirakawa). Seno (2000) and Tanioka & Seno (2001 a, b) first proposed the concept of inelastic deformation and showed that inelastic deformation can generate tsunami efficiently with diminishing slip. Their conceptual

model did not include realistic constitutive modeling of inelastic deformation. Neither did they relate inelastic deformation to anomalous rupture characteristics (see some recent examples in Gusman et al., 2012 and Hill et al., 2012). Ma (2012) modelled inelastic wedge deformation using undrained Mohr-Coulomb yield criterion and showed inelastic deformation can lead to slow rupture velocity and efficient tsunamigenesis with diminishing slip. Ma & Hirakawa (2013) further showed that inelastic deformation is a large energy sink, which can explain depletion in high-frequency radiation and low moment-scaled radiated energy for shallow subduction earthquakes. The free surface also exerts a fundamental control on inelastic deformation because the yielding of Coulomb materials is depth-dependent, leading to flower-like damage zone in a strike-slip setting (e.g., Ma, 2008; Ma & Andrews, 2010; Ma, 2022). Ma & Nie (2019) extended the inelastic deformation model to 3D. In Ma (2023), the dynamic rupture model with inelastic deformation in the northern Japan Trench for the 2011 Tohoku-Oki earthquake reduces the along-strike rupture velocity to ~850 m/s, which explains the timing of tsunami off the Sanriku coast, in contrast to the 3-min delay of shallow slip required by the elastic dislocation model of Satake et al. (2013). These results show that sediment can play a critical role in tsunami generation and deficiency in high-frequency radiation in its weak strength leading to inelastic deformation, rather than low rigidity identified in previous studies.

In a series of two papers, we will present fully coupled models of dynamic rupture, ocean acoustic waves, and tsunami for two large tsunamigenic earthquakes in the Japan Trench, focusing on tsunami generation and different radiation characteristics of seismic and acoustic waves in elastic and inelastic models. In part 1 (this paper), we will investigate the 2011 Tohoku-Oki earthquake. In part 2, we will show models of the 1896 Sanriku earthquake. Fully coupled models allow rigorous simulation of tsunami generation and propagation as well as ocean acoustic and

seismic waves (e.g., Lotto & Dunham, 2015; Lotto et al., 2018; Wilson & Ma, 2021; Ma, 2022; Abrahams et al., 2023). For both earthquakes we will show that inelastic wedge deformation in the northern Japan Trench leads to more depletion of high-frequency radiation than models with elastic deformation while generating tsunami more efficiently. The results will shed light on the validity of different hypotheses in explaining the tsunamis in 2011 and 1896 in the Japan Trench and have important implications to tsunami hazard assessments and reductions worldwide. Because ocean acoustic waves travel faster than tsunami there were studies advocating ocean acoustic waves for tsunami early warning (e.g., Ewing et al., 1950; Kozdon & Dunham, 2014; Mei & Kadri, 2018; Gomez & Kadri, 2023). However, depletion in high-frequency radiation may pose a challenge to use ocean acoustic waves for robust tsunami early warning because the periods of these waves are significantly shorter than that of tsunami.

We will also show in this work that moderate inelastic deformation coupled with ocean response can significantly increase slip duration, leading to locally large shallow slip >100 m south of 39°N (in contrast to diminishing shallow slip with intense inelastic deformation in the northern Japan Trench), which may be observed in Ueda et al. (2023). Increase of slip duration by inelastic deformation may explain the long-period ground motion recorded in the northern rupture zone of the 1999 ChiChi earthquake (Ma et al., 2003). Significant long-period radiation due to inelastic deformation will also be shown in part 2.

3.2. Fully coupled models

Our fully coupled models of dynamic rupture, ocean acoustic wave, and tsunami for the 2011 Tohoku-Oki earthquake are directly based on the dynamic rupture models of Ma (2023). Ma (2023) presented two models: one elastic model and one model with inelastic wedge deformation (mostly in the northern Japan Trench). Both models were based on a stress drop model of Kubota et al. (2022), constrained by on- and off-shore GPS and tsunami data. The fault geometry, bathymetry, and velocity structure were based on the Japan Integrated Velocity Structure Model (JIVSM) of Koketsu et al. (2012). The results from both models differ mostly in the northern Japan Trench, where the elastic model showed large slip (>40 m) at the trench, fast rupture velocity, and large slip velocity, while the inelastic model showed diminished slip (<20 m) at the trench, slow rupture velocity (~850 m/s), and small slip velocity. The large shallow slip in the elastic model violates the differential bathymetry observations north of 39°N (Fujiwara et al., 2017) and produces tsunami larger and faster than the observations offshore the Sanriku coast. In contrast, the inelastic model is consistent with the differential bathymetry and tsunami observations. These different rupture characteristics between the two models will also be seen in the fully coupled models below.

Figure 3.1 shows the map of this study, depicting the bathymetry, fault, sedimentary wedge with along-strike variation of sediment thickness (Tsuru et al., 2002), strong motion generation areas (SMGA, Kurahashi & Irikura, 2013), and geodetic and tsunami sensors considered in Ma (2023). The coordinate system used in this work is identical to the one in Ma (2023): the x axis is along the plate convergence direction (E20°S), y axis along N20°E, z axis vertical up, and the origin located at the epicenter (38°06.2' N, 142°51.6'E). The fault expands 200 km wide (along x) and 600 km long (along y), which breaks the trench at -200 km $\leq y \leq$ 300 km and is buried at $y \leq$ -200 km.

We refer the reader to Ma (2023) for the detailed set up of the models, which remains identical in this work. The only minor difference in the inelastic model here is that the wedge slope and fault dip are fit by using only the sediment part of the wedge, i.e., seaward from backstop (Supplemental Figure 3.1), which give rise to 5.4149° (wedge slope) and 4.5571° (fault dip). Ma (2023) obtained slightly different parameters by fitting the data within 65 km from the trench to consider possible inelastic deformation in the inner wedge. We allow inelastic deformation only in the sediment seaward from backstop in this work. These parameters set the stresses and strength parameters in the wedge; however, the results only show slight differences from Ma (2023).

To fully couple dynamic rupture, ocean acoustic waves, and tsunami, we add a compressible ocean to the models of Ma (2023). To create the ocean, we first create a hemi-ellipsoid (three axes are 340, 380, and 340 km along three coordinate axes) centered at (-80 km, -10 km, 0) to intersect the ocean. We then make a horizontal cut at 400 m depth on the seafloor and slice the cut line along an inclination angle 15° to intersect the sea surface, which results in the irregular curved line near the coast in Figure 3.1. The irregular dipping surface on the west (above 400 m depth), hemi-ellipsoid, and seafloor with realistic bathymetry form the boundary of the ocean of interest in the model. We use 4-node tetrahedral elements (element size ~500 m) to mesh the ocean. To minimize wave reflections at ocean-solid boundaries, we further extend the ocean outward for an additional ~300 km with a coarser mesh.

The coupling between the ocean and solid earth at the seafloor is done by enforcing continuity of normal displacement and traction and vanishing shear traction. To include gravity waves in the model we use a linearized sea surface boundary condition of Lotto & Dunham (2015), verified by a semi-analytical solution in Wilson & Ma (2021). This free surface boundary condition

naturally gives rise to dispersions of ocean acoustic waves and tsunami in the linear regime. The fully coupled models account for generation and propagation of gravity waves in the ocean, including the contributions of horizontal displacement of sloping seafloor and rupture duration on tsunami generation as well as filtering of short-wavelength uplift features by variable ocean depth (e.g., Lotto et al., 2018; Wilson & Ma, 2021), which may be the most accurate method in modelling tsunami although the computational expense is high compared to the widely-used shallow water models (Abrahams et al., 2022). The feedback of ocean on the solid earth is also rigorously simulated.

We present below two fully coupled models of the 2011 Tohoku-Oki earthquake and tsunami based on the elastic and inelastic models of Ma (2023). Each model is run for 500 s with a time step of 0.01 s.

3.3. Results

To illustrate the fully coupled models, we show 3 snapshots of slip velocity, vertical seafloor velocity, dynamic ocean bottom pressure (OBP) change, sea surface elevation, and seafloor displacements and inelastic shear strain at 6 cross sections at 38 s, 66 s, and 124 s for the inelastic model (Figure 3.2). In comparison, we also show the snapshot at 124 s for the elastic model, which shows significantly different rupture and radiation characteristics in the northern Japan Trench. The detailed processes for these two fully coupled models are illustrated in Movies 3.1 and 3.2. The rupture processes with ocean are nearly identical to the results of Ma (2023)

except for some differences at shallow depths (to be shown below), as in general the ocean has a minor effect on the response of solid earth.

Shortly after nucleation, the rupture expands in all directions driven by the large stress drop (~10 MPa) around the hypocenter. The rupture propagates faster up dip (mode II direction) with a rupture velocity ~3 km/s. Significant along-strike propagation at depth is also seen due to large stress drop along strike, although the rupture velocity is slower along the mode III direction. Strong seismic waves are excited, which causes rapid motion of the seafloor. The vertical seafloor velocity pattern strongly resembles the P-SV wave radiation pattern: up-dip rupture pushes the seafloor up, down-dip rupture pulls the seafloor down and the along-strike direction is a node. The up-dip rupture propagation enhanced by the free surface leads to strong directivity with large fault-normal motion, displacing seafloor mostly vertical above a shallowly dipping plate interface. Strong SH and Love waves are also excited and propagate along strike, but do not show up in vertical seafloor velocity and ocean bottom pressure. The vertical motion of seafloor compresses the ocean, generating strong P-wave in the ocean propagating upward, reflecting at sea surface and propagating downward as a pulling motion because sea surface boundary is nearly free. The reflected P-wave amplitude reverses again due to a large impedance contrast at seafloor, which gives rise to the alternating red and blue colors in vertical seafloor velocity and ocean bottom pressure change as P waves bounce multiply in the ocean. The tsunami can also be seen in the sea surface elevation in the model, which has much longer wavelengths than those of the ocean acoustic waves. A cross-sectional view of these fields was well illustrated in the movies of 2D models of Kozdon & Dunham (2014).

As the up-dip rupture breaks the trench at ~38 s, the slip velocity reaches ~17 m/s, which generates strong radiation of different waves. The largest wave propagating seaward is oceanic

Rayleigh wave. The strong reflected wave propagating landward is the PL wave (Kozdon & Dunham, 2014), which is a leaky P wave mode due to interference of P waves trapped in the ocean and upper solid earth but is leaking energy due to conversion to S wave (e.g., Oliver & Major, 1960; Phinney, 1961). Kozdon & Dunham (2014) found a good correlation of PL wave amplitude with slip at trench. Because these waves travel much faster than that of tsunami they advocated the use of PL wave for tsunami early warning. Indeed, the PL waves are strongly excited in our 3D simulations. As the rupture propagates bilaterally along strike (see 66 s), large PL wave radiation can be seen to follow behind the rupture front although the inelastic deformation has occurred. However, as the rupture enters the northern Japan Trench significant inelastic wedge deformation causes slow rupture velocity (~850 m/s), small slip velocity, diminishing shallow slip, and radiation of all acoustic waves become much weaker (Figure 3.2c). Large inelastic uplift occurs with diminishing horizontal displacement. In contrast, in the elastic model large acoustic radiation is clearly seen trailing behind the rupture front with large slip velocities and fast rupture velocity (Figure 3.2d). Large seafloor uplift is caused by fast slip peaking at trench. In both models, rupture directivity greatly enhances the amplitudes of oceanic Rayleigh waves: they are smallest directly updip from the hypocenter but are much larger to the north and south, shown more clearly in dynamic ocean bottom pressure changes. At 124 s, the tsunami splitting above the trench can be seen.

The wavefields are complex because radiation from the rupture front is contaminated by the waves radiated from earlier rupture propagation (including breaking of the SMGAs at depth). To show the differences of radiations at rupture front in the two models we calculate the difference between the wavefields of the two models (Figure 3.3). The waves due to the earlier rupture at depth are cancelled because they are identical in the two models. What remains is the difference

due to radiation near trench influenced by inelastic wedge deformation. Because the radiation from inelastic deformation is much weaker the difference shown reflects largely the radiation from the rupture front in the elastic model. Significant energy is trapped within the sediment behind the rupture front, which is the source of radiation. The PL waves clearly radiate from behind the rupture front but travel faster than the rupture. Some PL waves radiated from earlier rupture even arrive in front of rupture front. The alternating blue and red colors indicate oscillatory nature of P waves trapped in the ocean. These waves are clearly dispersive; longer-wavelength components travel faster. A small, short-wavelength PL wave is seen to radiate from the trapped energy behind the rupture front, which propagates slowest. The radiation of oceanic Rayleigh wave is also greatly reduced by inelastic wedge deformation. Clear slower propagation of oceanic Rayleigh waves than PL waves is shown as they both radiate from the rupture front. The radiation differences between elastic and inelastic models as rupture propagates are more detailed in Movies 3.1 and 3.2.

Figure 3.4a shows the snapshots of tsunami from the fully coupled model with inelastic deformation, which is remarkably similar to the tsunami from a shallow water model of Ma (2023), shown in Figure 3.4b. The shallow water model, assuming incompressible ocean, solved a 2D nonlinear Boussinesq equation using the time-dependent seafloor displacement from the dynamic rupture model. At each time step, contribution from horizontal displacement (Tanioka & Satake, 1996) is calculated and added to the total seafloor uplift. Then, a lowpass Kajiura filter with a cutoff wavelength of 6 km is applied to filter out short-wavelength waves by the ocean (Kajiura, 1963) before entering it in the shallow water model. To account for tsunami dispersion, a Boussinesq equation needs to be solved. In the fully coupled model these effects have been considered in sea surface and bottom boundary conditions. The agreement between the two models validates both approaches, especially when a constant cutoff wavelength was used in the shallow

water model. Note that the ocean acoustic waves are clearly visible in the first 4 snapshots of Figure 3.4a, but not in Figure 3.4b. The slightly different tsunami amplitudes are largely due to the presence of ocean acoustic waves in the fully coupled model.

The slip distributions at t = 500 s for both the fully coupled elastic and inelastic models are shown in Figure 3.5c and d. Rupture time contours every 10 seconds are marked in black. They are very similar to the models of Ma (2023) without ocean, shown in Figure 3.5a and b. The slip distributions and rupture velocities outside northern Japan Trench among all models are similar because of dominantly elastic off-fault response. North of 38.7°N, the large shallow slip and fast rupture velocity in the elastic models and diminishing shallow slip and slow rupture propagation in the inelastic models are clearly seen.

However, when we examine slip distributions more closely peak slip differs in a small patch near y = 50 km at the trench. The peak slip in the fully coupled model with inelastic deformation reaches 109.43 m, much larger than the fully coupled elastic model (85.17 m). In the two models without ocean, the peak slip in the inelastic model (75.67 m) is smaller than that of elastic model (87.63 m). The slip contours in blue also indicate that slip is slightly larger in the northern Japan Trench in the inelastic model with ocean than without ocean.

To find out what gives rise to such large slip in this small patch we show the space-time plots of the slip velocity along y = 50 km and relevant time histories at trench for all 4 models (Figure 3.6). One feature to notice immediately is the longer slip duration near trench with inelastic deformation than elastic models (Figure 3.6a – e). The peak slip rate is also reduced by inelastic deformation in models with or without ocean (Figure 3.6e). In the two models without ocean the longer slip duration cannot compensate for the large reduction of peak slip rate so after time integration the final slip is still smaller in the inelastic model. We note a large reduction of peak

slip rate in the elastic model with ocean compared to the model without ocean, which is likely due to the elasticity of ocean (compared to free surface) suppressing slip velocity during rupture breakout. In the inelastic model with ocean this reduction in peak slip rate is much smaller. However, there is a second peak in the slip rate, which coincides with the dilation caused by the reflected P waves from sea surface leading to normal stress reduction and additional stress drop on the fault. This strong dilation makes the slip rate with ocean larger than that without ocean for ~10 s, which gives rise to larger slip after time integration. In the elastic model with ocean this dilatational effect is also present. However, the large reduction of peak slip rate counteracts this effect, making the final slip with and without ocean about similar. Therefore, the combined effect of inelastic deformation and hydroacoustic dilation leads to long slip duration and large, localized slip in this small patch and slight increase in slip in the northern Japan Trench. This effect may only occur with modest inelastic deformation as the peak slip rates between elastic and inelastic models are similar. If the severe inelastic deformation reduces slip rate significantly this combined effect cannot lead to large slip increase; instead diminished shallow slip should occur, as seen in the northern Japan Trench.

The horizontal and vertical surface displacements for the 2 models with ocean at 500 s are shown in Figure 3.7. Although the peak horizontal and vertical displacements differ due to the difference in peak slip both models produce nearly identical fits to the GPS data, indicating limited resolution of GPS data to near-trench deformation. We point out that the large, localized slip patch is likely unimportant in tsunami generation because any features with wavelengths shorter than ocean depth are filtered out by the ocean (Kajiura, 1963), which can be seen in Figure 3.4.

To better illustrate the radiation characteristics between elastic and inelastic models we show the space-time plots of vertical seafloor velocity and dynamic ocean bottom pressure change,

as well as the differences between elastic and inelastic models, along 5 cross sections in Figures 3.8 and 3.9. At $y = 0$, the inelastic deformation is small there is little difference between the two models. Both models resemble closely the 2D dynamic rupture model for the 2011 Tohoku-Oki earthquake of Kozdon & Dunham (2014). The radiation from up- and down-dip rupture from hypocenter can be clearly seen. After rupture breakout at trench strong landward-propagating PL waves and seaward-propagating oceanic Rayleigh waves are strongly excited. There are also distinctly trapped P waves bouncing up and down (marked as organ pipe) in the models. The speed of PL waves exceeds the S-wave speeds of upper crustal layers in the JIVSM (see Figure 2 of Ma, 2023), excluding the possibility of any surface waves and S waves. The landward tsunami is also clearly seen, which was not considered in Kozdon & Dunham (2014). As the rupture propagates northward, similar patterns are seen. PL and oceanic Rayleigh waves are generated at the trench with stronger radiation in the elastic model, which can be more clearly seen in the differences between the two models because common radiations from earlier ruptures are removed. The organ-pipe waves are also much stronger in the elastic model shown in Figure 3.9. The differences between the two models increase to the north due to more significant inelastic deformation, causing weak radiation. The apparent velocity of PL wave seems larger as rupture propagates northward, which is due to the oblique incidence of these waves on the cross sections (Figure 3.3). The trapped wave energy landward from trench appear to be the source of radiation as sediment thickens northward, which are stronger in the elastic model. The slowest propagating PL wave trailing from behind the rupture front is seen to propagate with an apparent velocity less than 1.5 km/s, which is related to rupture velocity (see Figure 3.3, Movies 3.1 and 3.2). The space-time plots of horizontal seafloor velocity are shown in Supplemental Figure 3.2, which shows similar results

and indicates that particle motion is mostly in the same plane as the wave direction, confirming the identification of PL waves.

Figure 3.10 shows the space-time plots of sea surface elevation. Clear tsunami propagation superimposed by ocean acoustic waves is seen. One feature to notice immediately is the longer-wavelength of tsunami at $y = 0$ and 50 km caused by ~200 km rupture width. The width of rupture zone in the northern Japan Trench is only ~40 km, leading to impulsive tsunami as observed off Sanriku coast. Reduction of wavelength during shoaling is also clearly seen at $y = 0$ and 50 km. Tsunami amplitudes are nearly identical in the southern two cross sections between elastic and inelastic models because inelastic deformation is small. In the northern Japan Trench ($y = 150$ and 200 km), the tsunami amplitudes are larger in the elastic model due to >40 m shallow slip peaking at trench, which is inconsistent with the differential bathymetry observations. The elastic model also overestimates the tsunami amplitudes (Ma, 2023). If we normalize sea surface elevation by average slip within 40 km from trench at each section and define it as the efficiency of tsunami generation, we see that the efficiency is the largest in the two northern cross sections in the inelastic model (Figure 3.11). We choose 40 km because it is about the width of rupture in the northern Japan Trench and the value used in the differential bathymetry studies to infer coseismic displacement near trench, which is also the major tsunami generation zone. The average slip at each cross section is shown in the lower right corner of each panel. The larger efficiency in the inelastic model is not surprising because inelastic deformation represents frictional sliding on microfractures with steeper dips than that of the plate interface. The inelastic model produces tsunami with diminishing shallow slip, consistent with the differential bathymetry observations, and the amplitude and timing of tsunami match the observations off the Sanriku coast (Ma, 2023).

We show time histories of two components of seafloor velocity, dynamic ocean bottom pressure change, and sea surface elevation for the two models in Figures 3.12 – 3.14 and Supplemental Figure 3.3. Again, the main difference between the two models is the radiation of ocean acoustic waves, mostly PL, organ pipe, oceanic Rayleigh waves, and trapped waves in the sedimentary wedge. Note that different scales are used for the landward and seaward sides from the trench in Figure 3.13 because the ocean bottom pressure change is much larger in seaward-propagating oceanic Rayleigh waves (see also Figure 3.9). Different periods of ocean acoustic waves and tsunami are clearly shown in Figure 3.14.

3.4. Discussion and Conclusions

The concept of using ocean acoustic waves in tsunami early warning can be traced back to Ewing et al. (1950), who proposed using T waves for tsunami warning. Okal et al. (2003) pointed out that T waves primarily reflect high-frequency characteristics of the source rather than the low-frequency processes controlling tsunami generation, and are particularly weak in tsunami earthquakes, which can severely underestimate tsunami hazards. Kozdon & Dunham (2014) proposed using PL waves for rapid estimate of shallow slip to issue tsunami warnings because these waves travel much faster than tsunami. They assumed that slip occurs rapidly and there may be strong rupture breakout at trench, similar to the elastic model in this work. As they pointed out clearly, the PL wave excitation can be significantly weaker if rapid slip does not occur. As shown in our inelastic model, the radiation of PL and other acoustic waves are significantly reduced by inelastic deformation, but devasting tsunami can be generated with diminishing shallow slip. Other similar works (e.g., Mei & Kadri, 2018; Gomez & Kadri, 2023) advocating ocean acoustic waves

71

for tsunami early warning may also have overlooked the deficiency in high-frequency radiation associated with large tsunamigenesis, a key characteristic pointed out by Kanamori (1972). Because tsunami has much longer period any application of high-frequency acoustic and seismic waves in giving early warnings on robust tsunami amplitude may be a challenge.

The large shallow slip hypothesis for tsunami generation has been widely used in subduction zones worldwide. Although >50 m slip updip from the hypocenter in the 2011 Tohoku-Oki earthquake was confirmed by the differential bathymetry observation this hypothesis violates the differential bathymetry observation north of 39°N. Neither can it account for depletion in high-frequency radiation. Sediment in an elastic setting does not lead to depletion in high-frequency radiation, contradicting many previous studies (e.g., Polet & Kanamori, 2000; Sallarès & Ranero, 2019). Slip models by inverting seismic data failed to resolve the rupture in the northern Japan Trench, which can also be due to depletion in high-frequency radiation. Therefore, the application of elastic dislocation theory and large shallow slip hypothesis in sediment-filled margins, such as northern Japan Trench, may be questionable.

We have shown that inelastic wedge deformation can explain both large tsunamigenesis and depletion in high-frequency radiation in the northern Japan Trench in fully coupled models of dynamic rupture, ocean acoustic waves, and tsunami for the 2011 M_W 9.1 Tohoku-Oki earthquake. Due to presence of thick sediment in the northern Japan Trench inelastic deformation of sediment generates large seafloor uplift (~4 m) with diminishing shallow slip (<20 m), consistent with the differential bathymetry observations. Meanwhile, inelastic deformation is a large energy sink (Ma & Hirakawa, 2013), which leads to slow rupture propagation (~850 m/s) and weak acoustic and seismic radiations. This mechanism provides a self-consistent explanation to large tsunamigenesis,

depletion in high-frequency radiation, and the mysterious >100 km offset between the large tsunami north of 39°N and major shallow slip zone up dip from the hypocenter. In part 2, we will apply it to address the physics of 1896 Sanriku earthquake.

Physics of tsunamigenesis is essential in tsunami hazard reduction worldwide, such as whether ocean acoustic waves can be used in tsunami early warning discussed in this paper. The inelastic wedge deformation hypothesis can probably be applied to accretionary or other sediment-rich margins. Future seafloor observations, such as S-net (Aoi et al., 2020) can help test both the large shallow slip and inelastic deformation hypotheses even further.

Finally, inelastic deformation can greatly increase slip duration at shallow depth and lead to large slip, which may provide an alternative mechanism for the long-period ground motion observed in the northern rupture zone of the 1999 ChiChi earthquake, other than hydroacoustic lubrication (Ma et al., 2003) and thermal pressurization (Noda & Lapusta, 2013).

Acknowledgements

Chapter 3, in full, is currently being prepared for submission for publication of the material. Du, Yue; Ma, Shuo. The dissertation author was the primary investigator and author of this material.
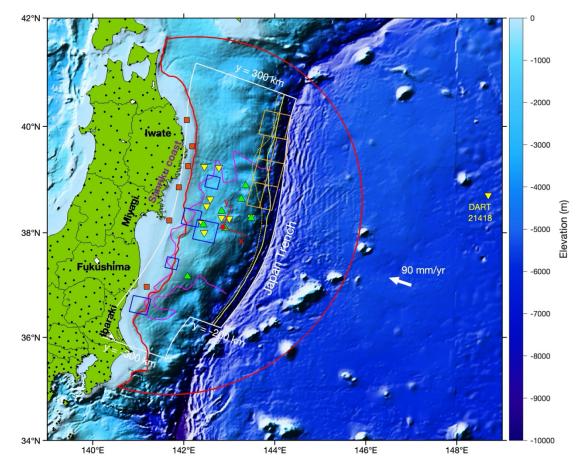
Figure 3.1. Map of the study. The fault surface used in this work is outlined by white. The red dot denotes the epicenter of the 2011 Tohoku-Oki earthquake, which is the origin of the coordinate system used (shown in red, *x* axis is along the plate convergence direction). The magenta curve shows the coseismic rupture area inferred by Kato & Igarashi (2012). The blue squares are the SMGAs identified by Kurahashi & Irakura (2013). The yellow solid and dotted lines denote the traces of the backstop surface on the seafloor and plate interface, respectively, by fitting the sediment-thickness data of Tsuru et al. (2002). Thicker sediments in the northern Japan Trench can be clearly seen. The 8 subfaults of Satake et al. (2013, 2017) in the northern Japan Trench depict the rupture zone of the 1896 Sanriku earthquake. Stations shown are on-land GPS stations (black dots), GPS buoys (orange squares), OBP sensors (yellow inverted triangles), and off-shore GPS stations (green triangles). The four prefectures mentioned in the paper and the Sanriku coast are denoted. These features are identical to those in Figure 1 of Ma (2023). The red crescent-shaped curve is the boundary of the ocean of interest considered in this work.
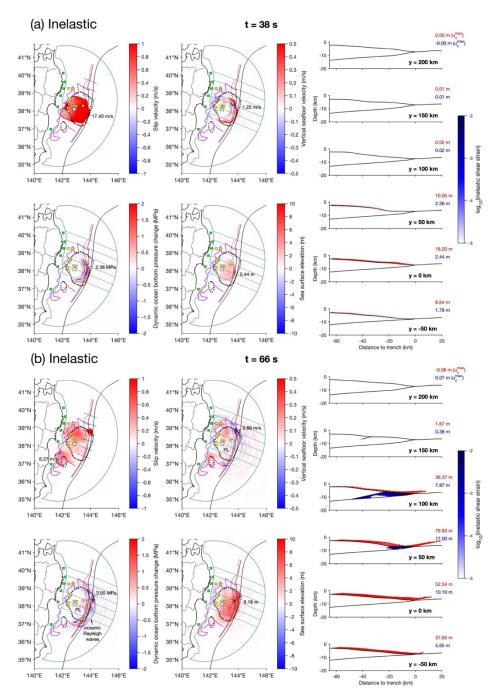
Figure 3.2. Snapshots of slip velocity, vertical seafloor velocity, dynamic ocean bottom pressure change, sea surface elevation, and seafloor displacements at 6 cross sections are shown for the inelastic (a – c) and elastic (d) models. The inelastic strain in the wedge is also shown in (a – c). The black dotted line shows the 15 m contours of slip model of Iinuma et al. (2012). The fully coupled models capture both ocean acoustic and seismic waves and tsunami. Wave fields are complex. Different radiations and seafloor displacements in the northern Japan Trench due to different rupture characteristics between the two models at 124 s are seen with significantly weaker radiation in the inelastic model. More details about the two models are illustrated in Movie 3.1 and 3.2.
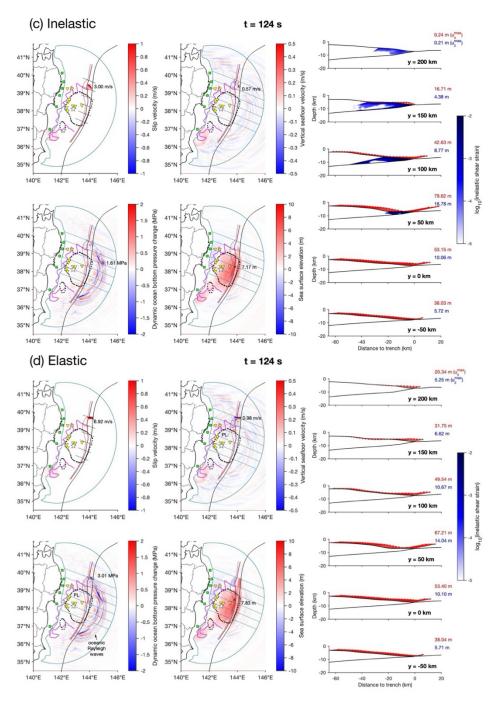
Figure 3.2. Continued.
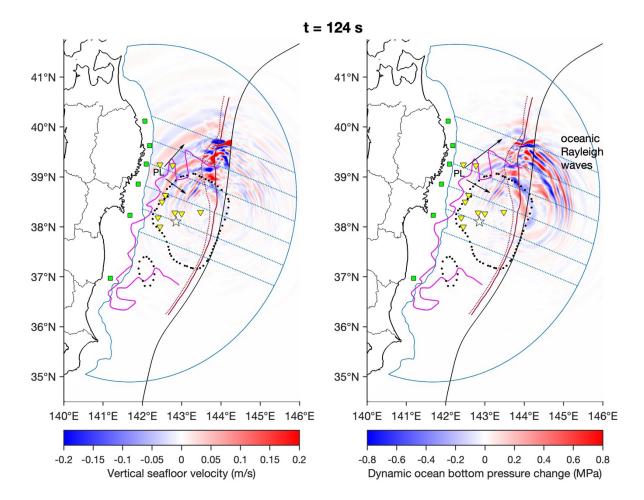
Figure 3.3. Differences in vertical seafloor velocity and dynamic ocean bottom pressure change between the elastic and inelastic models at 124 s are shown. The wave fields are much cleaner due to the cancelling of same waves from earlier rupture governed by the same elastic off-fault response in both models. Due to weak radiation in the inelastic model the differences shown are mostly due to stronger radiation in the elastic model, showing clearly dispersive PL and oceanic Rayleigh waves emanating from rupture front. Strong trapped energy in the sediment behind rupture front in the elastic model is seen.
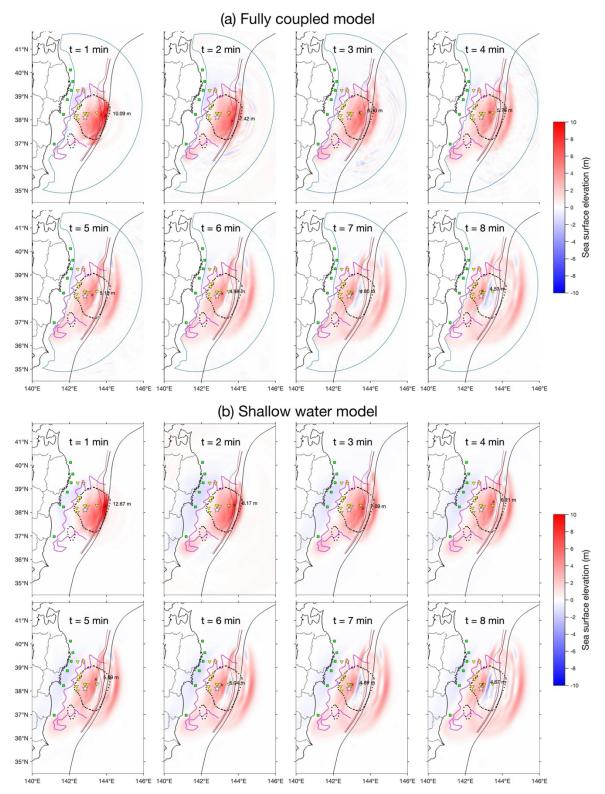
Figure 3.4. Comparison of tsunamis from between the fully coupled inelastic model and shallow water model from Ma (2023). Excellent agreement is obtained.
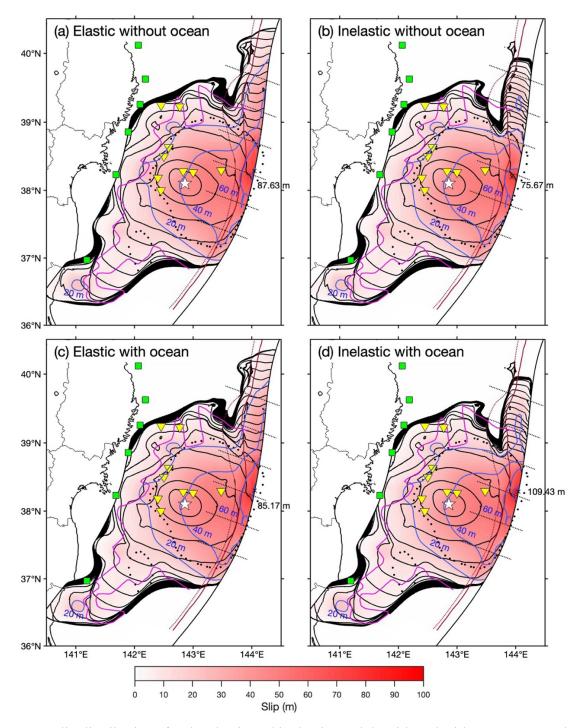
Figure 3.5. Slip distributions for the elastic and inelastic models with and without ocean are shown. Black contours show rupture time every 10 s and blue contours are slip every 20 m. Slow rupture velocity and diminishing shallow slip in the northern Japan Trench are clearly seen in the two inelastic models (b, d), while elastic models (a, c) show fast rupture velocity and large shallow slip. Peak slip value is marked, and the location indicated by x. A small patch with slip > 100 m is seen in (d).
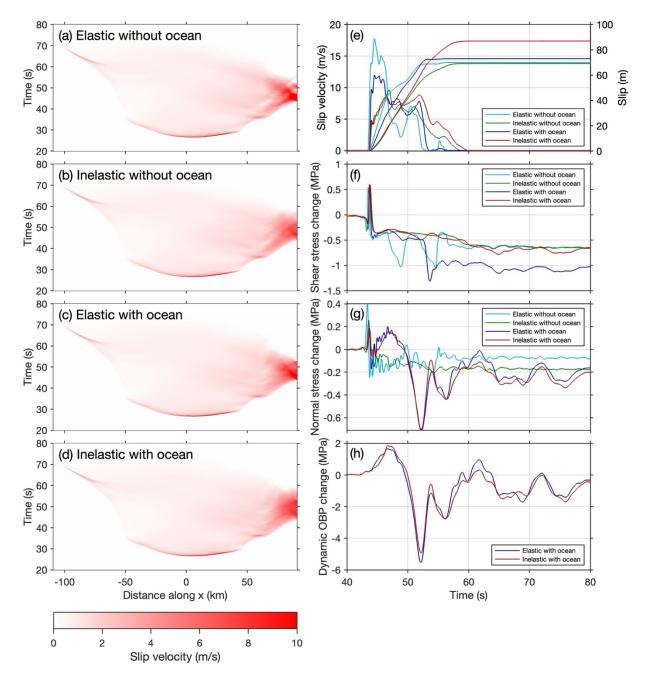
Figure 3.6. Space-time plots of slip velocity at y = 50 km (a – d) and time histories at trench are shown for the four models. Longer slip duration near the trench in the inelastic models can be seen in (a – d) and slip velocity time histories in (e) due to more gradual stress changes (f). Large dilation around 50 s due to P waves reflected from sea surface causes fault normal stress reduction shown in (g, h), which leads to large slip velocity increase and longer slip duration in (e). The peak slip rate is only reduced slightly by modest inelastic deformation in the model with ocean, so the long duration leads to large slip. The large shear stress reduction for the two elastic models (cyan and blue curves) around 50 s in (f) are due to decrease of slip velocity; in the rate-and-state friction as the state variable nears steady state the shear stress is proportional to the logarithm of slip velocity.
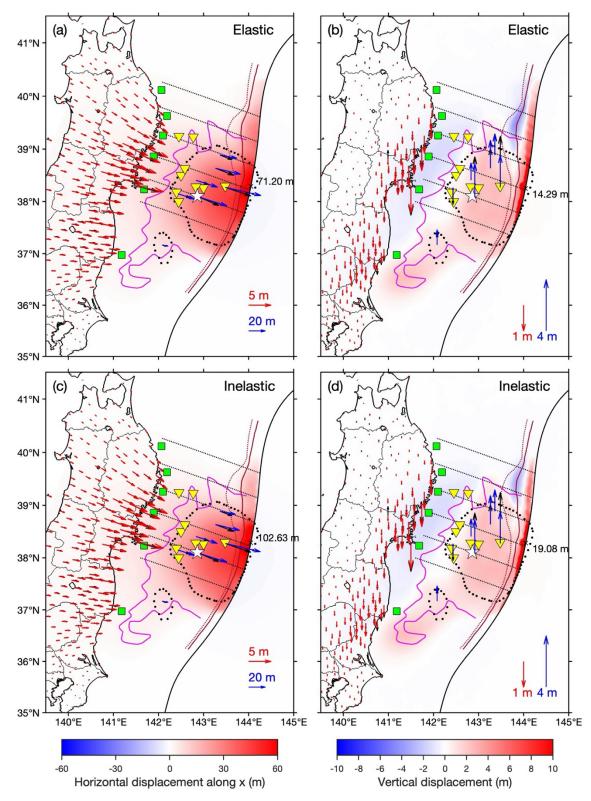
Figure 3.7. Horizontal and vertical seafloor displacements from the elastic and inelastic models are compared with geodetical observations, showing little resolution of data to near-trench deformation.
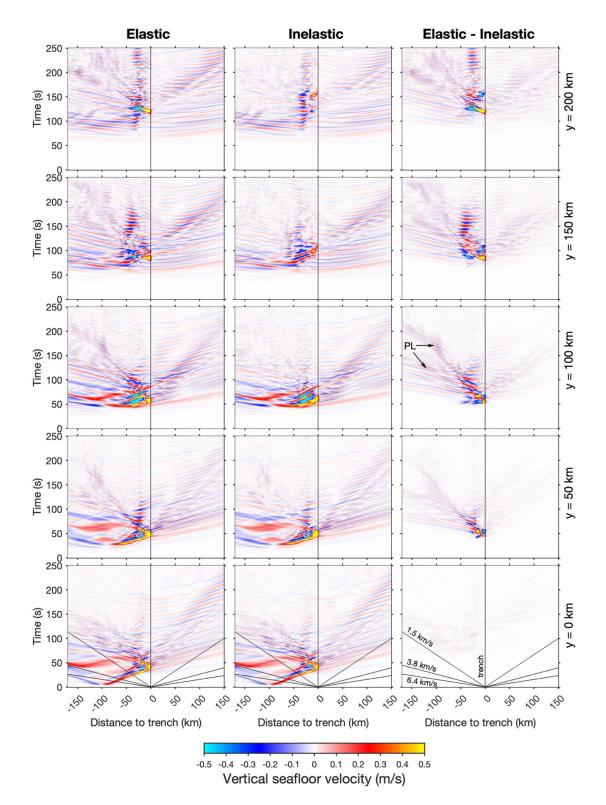
Figure 3.8. Space-time plots of vertical seafloor velocity in elastic and inelastic models are illustrated at 5 cross sections. The difference between the two models is shown in the right column, depicting clearly stronger PL and oceanic Rayleigh waves radiated from rupture front and larger energy trapped within the sediment in the elastic model.
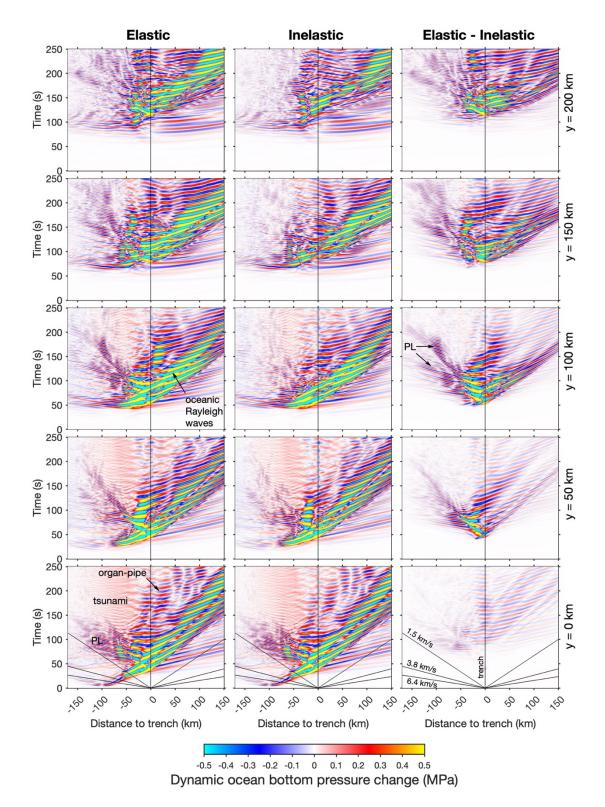
Figure 3.9. Same as Figure 3.8 except for dynamic ocean bottom pressure change. Larger organ-pipe waves above trench in the elastic model can also be seen. The landward tsunami (in pink) is clearly seen in the bottom three rows.
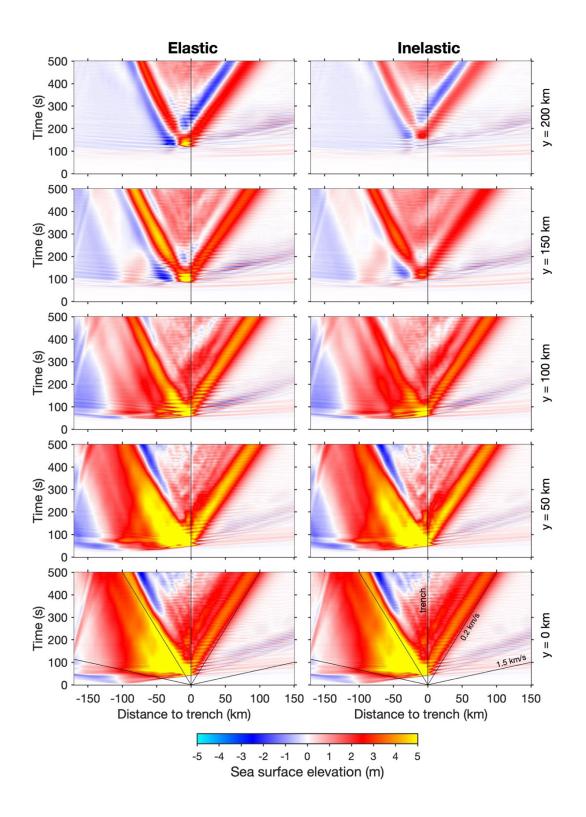
Figure 3.10. Space-time plots of sea surface elevation for elastic and inelastic models are shown. Larger tsunami in the northern 3 cross sections in the elastic model due to larger slip at trench is seen, which, however, overpredicts the observations (Ma, 2023). Reflection from the coast is due to the artificial ocean boundary in the model (Figure 3.1).
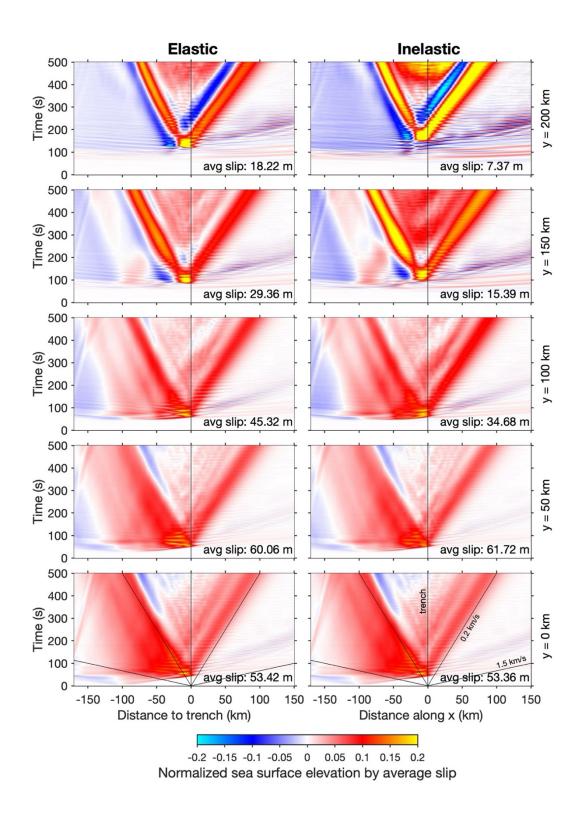
Figure 3.11. Space-time plots of normalized sea surface elevation for elastic and inelastic models show higher efficiency in tsunami generation by inelastic wedge deformation in the northern Japan Trench. The efficiency is defined by the ratio of sea surface elevation to the average slip within 40 km from trench in each cross section (shown in the lower right corner of each panel).

85
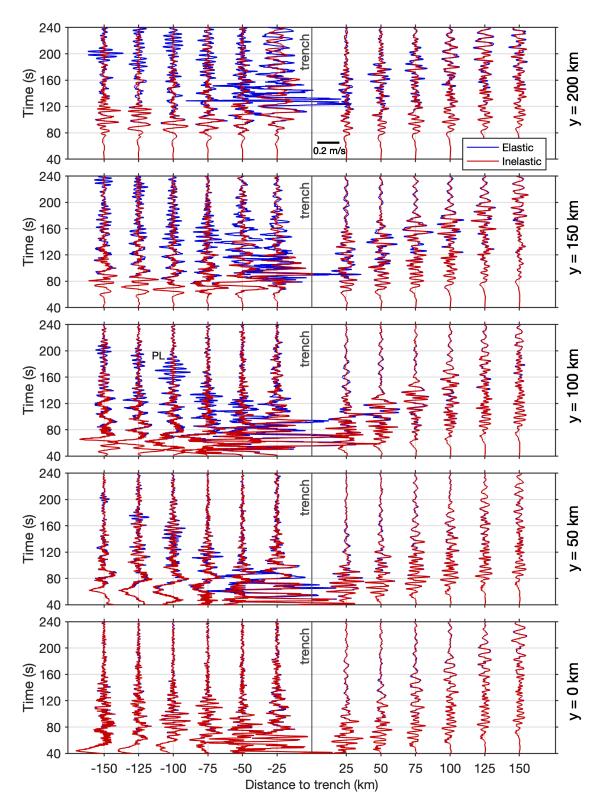
Figure 3.12. Vertical seafloor velocity time histories are compared between elastic and inelastic models, showing stronger radiation landward from trench in the elastic model.
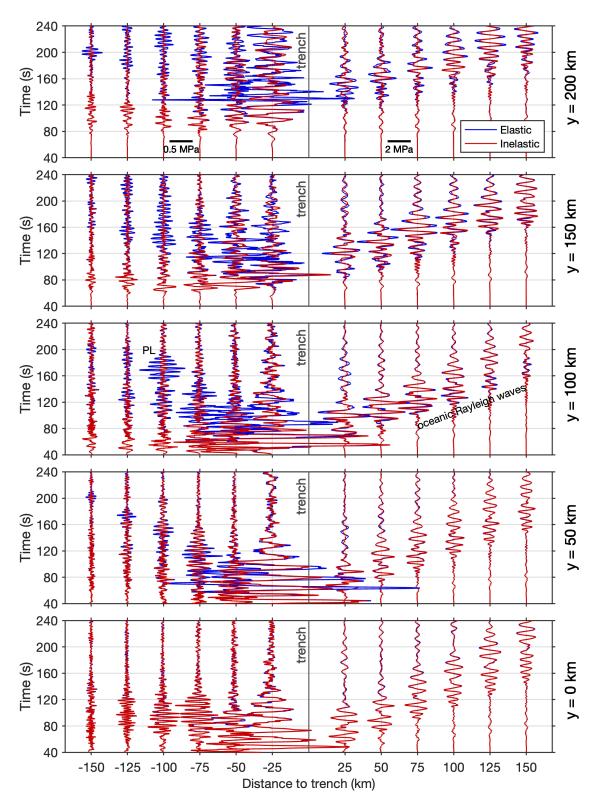
Figure 3.13. Same as Figure 3.12 except for dynamic ocean bottom pressure change. Different amplitude scales are used for landward and seaward from trench.
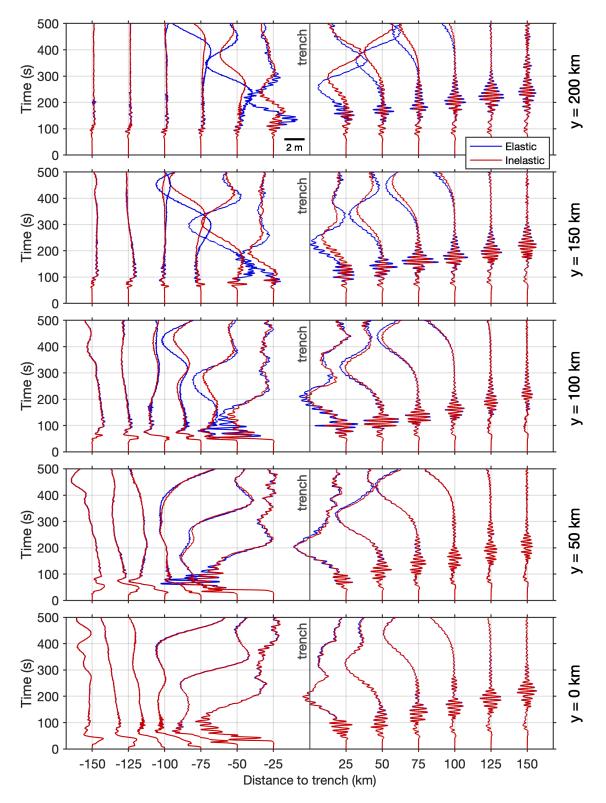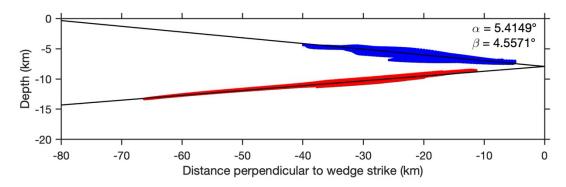
Figure 3.14. Time-histories of sea surface elevation are compared between elastic and inelastic models. Note the different periods of ocean acoustic waves and tsunami. Larger tsunami in the northern Japan Trench in the elastic model overpredicts the tsunami observations (Ma, 2023). The efficiency of tsunami generation is higher in the inelastic model, shown in Figure 3.11.
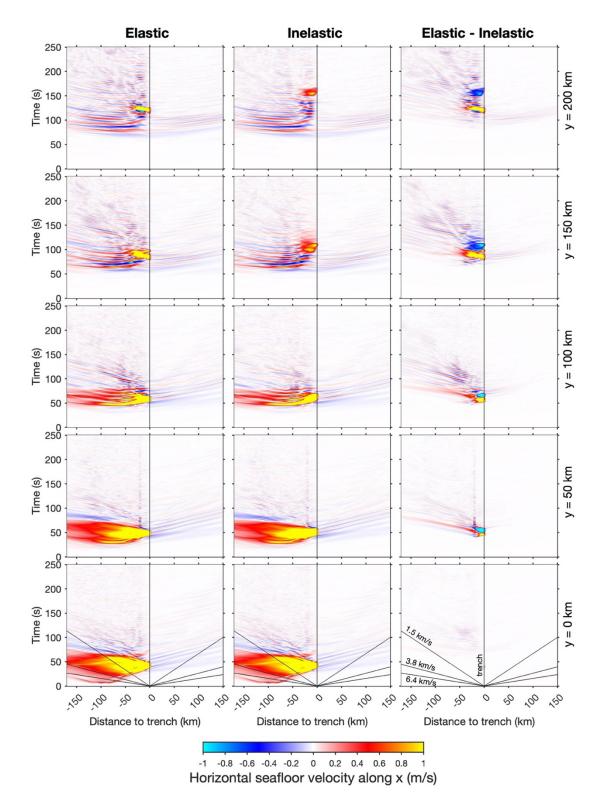
Supplementary materials

Movie 3.1. Movie of slip velocity, vertical seafloor velocity, dynamic ocean bottom pressure change, sea surface elevation, and seafloor displacement vectors and inelastic shear strain in the wedge at 6 cross sections in the inelastic model. The differences between elastic and inelastic models are shown in the lower central two panels. The dotted lines show the locations of cross sections. The magenta curve shows the coseismic rupture extent inferred by Kato & Igarashi (2012). The dark red solid and dotted lines show the traces of the backstop at seafloor and plate interface. The white star denotes the epicenter. The green squares and yellow inverted triangles are the GPS buoy and OBP stations, respectively. The x symbol shows the location of peak amplitude at each time instant in each panel (the value shown in the lower right corner). In the northern Japan trench, as rupture propagates into thick sediments a slow rupture with small slip rate is clearly caused by inelastic wedge deformation, diminishing horizontal seafloor displacement and increasing seafloor uplift. The seafloor deformation is consistent with the differential bathymetry observations. Strong radiation due to large shallow slip updip from hypocenter and weak radiation in the northern Japan Trench is evident. The differences between elastic and inelastic models show stronger radiations of PL, oceanic Rayleigh, organ pipe waves and energy trapped within the sediment behind the rupture front. The tsunami generation and propagation are also clearly illustrated in sea surface elevation changes.
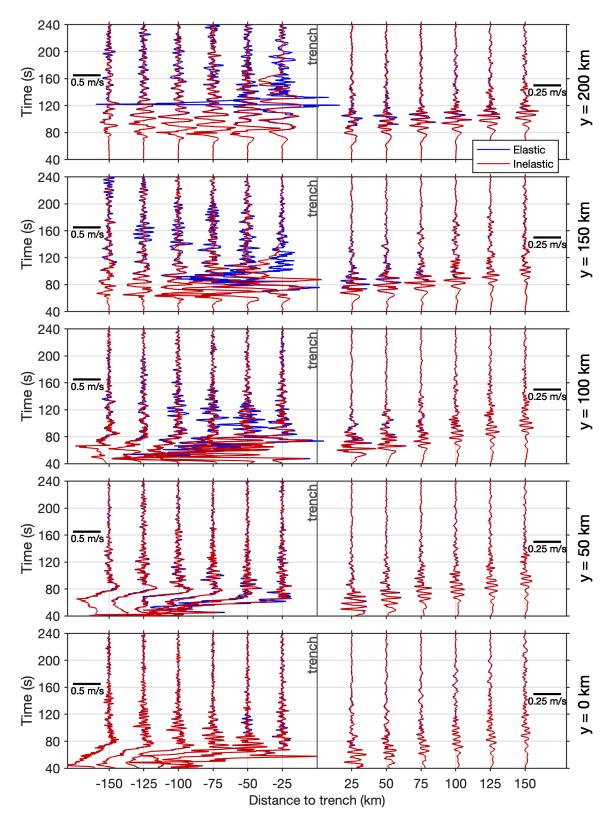
Movie 3.2. Similar to Movie 3.1 except for the elastic model. The difference with the inelastic model lies mostly in the northern Japan Trench. Faster rupture velocity, larger slip velocity, and large horizontal seafloor displacement peaking at trench in the northern Japan Trench produce much stronger radiations than the inelastic model. The large horizontal displacement peaking at the trench north of 39°N is inconsistent with the differential bathymetry observations.

Supplemental Figure 3.1. Projection of all the points at top and bottom of wedge sediment for 50 < y < 250 km in the finite-element mesh onto a plane normal to N5°E. Linear fitting gives the surface slope (α) and basal dip (β) used in the critical wedge solution. Note that the 10° dipping fault segment from the trench is not included in the fitting.

Supplemental Figure 3.2. Same as Figure 3.8 except for horizontal seafloor velocity along *x*-direction. The color is saturated. Similar PL wave patterns can be seen.

91

Supplemental Figure 3.3. Same as Figure 3.12 except for horizontal seafloor velocity along *x*-direction.

Chapter 4

Wedge Inelasticity and Fully Coupled Models of Dynamic Rupture, Ocean Acoustic Waves, and Tsunami in the Japan Trench: 2. The 1896 Sanriku Earthquake

Abstract

One of the essential characteristics of earthquakes associated with large tsunami generation is depletion in high-frequency radiation, which is not well understood by elastic dislocation theory and largely not accounted for in most rupture models of real events. In part 1, we considered the 2011 Tohoku-Oki earthquake. Here in part 2, we present fully coupled models of dynamic rupture, ocean acoustic waves, and tsunami for the 1896 Sanriku earthquake. The inelastic wedge deformation due to thick sediment in the northern Japan Trench is shown to generate efficient short-wavelength seafloor uplift (>5 m), which is several times larger than the uplift by elastic dislocation models and generates impulsive tsunami that can have large impact on the rugged Sanriku Coast. The inelastic wedge deformation is, however, a large energy sink, which causes slower rupture velocity, weaker radiation of ocean acoustic and seismic waves, and ~10 times lower moment-scaled radiated energy than from elastic models, explaining nearly all anomalous characteristics of this tsunami earthquake. The anti-plane shear stress in the mode III rupture direction (along strike), limited by yielding, plays an important role in the slow rupture velocity and energy radiation along strike. Ocean acoustic waves may not provide robust signals for tsunami early warning due to weak high-frequency radiation. Large, long-duration ground velocity pulses can naturally result from inelastic deformation.

4.1. Introduction

The 1896 Sanriku earthquake was one of the two tsunami earthquakes identified by Kanamori (1972). The earthquake was only weakly felt, but the tsunami that arrived ~30 minutes later devastated coastal towns along the Sanriku coast, killing more than ~22,000 people (Shuto et al., 2007). The death toll exceeded that of the 2011 M_W 9.1 Tohoku-Oki earthquake, making it the deadliest earthquake in recorded Japanese history. The surface wave magnitude was M_S 7.2 (Abe, 1994) estimated from global data, well below the moment magnitude ~M_W 8.0 (Utsu, 1994), reflecting the deficiency in high-frequency radiation. The seismic intensity was only 2 – 3 on the Japan Meteorological Agency (JMA) scale and 4 – 5 on the Modified Mercalli scale (e.g., Satake et al., 2017). However, the largest tsunami runup reached up to 40 m (Iki, 1897; Matsuo, 1933), similar to that of the M_W 9.1 Tohoku-Oki earthquake despite the lower magnitude.

Over the last 50 years, tens of other tsunami earthquakes have been identified from better-quality data (e.g., Lay et al., 2012). However, the 1896 Sanriku earthquake remains one of the most anomalous events and the physics for deficiency in high-frequency radiation and large tsunamigenesis is elusive. The earthquake occurred in the northern Japan Trench, with epicenter at (144°E, 39.5°N) (Utsu, 1979), which is the same region that generated devastating tsunami in 2011 that caused extreme runup along the Sanriku coast, more than 100 km north of the epicenter.

Only a few studies modeled this earthquake, mostly using tsunami data. Kanamori & Kikuchi (1993) suggested large submarine landslides for the source of the tsunami due to the puzzling depletion in high-frequency radiation. Tanioka & Satake (1996) and Tanioka & Seno (2001) presented simple elastic dislocation models with uniform slip. They found that rupture zone of about 200 km long along strike and less than 50 km wide located close to trench is required by the tsunami data. Tanioka & Seno (2001) also considered simple conceptual model of inelastic

deformation and showed that with inelastic deformation tsunami data can be explained by reduced fault slip. Satake et al. (2017) inverted waveform data at 3 tidal gauges in the far field using 8 subfaults of Satake et al. (2013) in the northern Japan Trench. They concluded that the 1896 earthquake occurred deeper than the northern rupture of the 2011 Tohoku-Oki earthquake in the model of Satake et al. (2013). Ma & Nie (2019) presented a generic inelastic wedge deformation model of M_W 8.0 earthquake similar to the 1896 Sanriku earthquake and suggested that inelastic wedge deformation of thick sediment in the northern Japan Trench (Tsuru et al., 2002; Kodaira et al., 2017) can explain large tsunamigenesis with diminishing slip and weak high-frequency radiation. Du et al. (2021) modelled the 1896 Sanriku tsunami using an inelastic wedge deformation model of Ma & Nie (2019) and produced tsunami runup in good agreement with the observations (Iki, 1897; Matsuo, 1933), better than those of Satake et al. (2017) obtained from inversion. They emphasized the importance of short-wavelength inelastic uplift in generating impulsive tsunami that can have large impact on the rugged Sanriku coast.

In part 1, we presented fully-coupled models of dynamic rupture, ocean acoustic waves, and tsunami for the 2011 M_W 9.1 Tohoku-Oki earthquake. We showed that inelastic wedge deformation in the northern Japan Trench can produce large seafloor uplift (~4 m) with diminishing slip (<20 m), consistent with the differential bathymetry observations (Fujiwara et al., 2017, 2021; Kodaira et al., 2021), and give rise to slow rupture propagation (~850 m/s) and strongly reduced radiation of ocean acoustic and seismic waves. The slow rupture propagation and weak high-frequency radiation is largely due to inelastic wedge deformation being an energy sink. The frictional sliding on microfractures, mimicked by inelastic deformation, however, generates tsunami more efficiently than slip on a shallowly dipping plate interface. The dynamic rupture model with inelastic wedge deformation in the northern Japan Trench provides a more consistent

explanation to the various observations of differential bathymetry, tsunami, and energy radiation of this earthquake than probably all the elastic dislocation models to date.

In this work, we will extend the same modeling approach and present fully-coupled models of dynamic rupture, ocean acoustic waves, and tsunami for the 1896 Sanriku earthquake. The models will be focused on the northern Japan Trench only due to a smaller rupture extent. We will further examine how inelastic wedge deformation may account for nearly all the anomalous characteristics of this tsunami earthquake.

4.2. Fully coupled models

As in part 1, we use the fault geometry, bathymetry, and velocity structure from the Japan Integrated Velocity Structural Model (JIVSM) based on Koketsu et al. (2012) and incorporate the sediment thickness variation along the Japan Trench from Tsuru et al. (2002). The P- and S-wave speeds and density in the sedimentary wedge are 3000 m/s, 1500 m/s, and 2250 kg/m^3, respectively. In the Tohoku-Oki earthquake models in Ma (2023) and part 1, a 10° dipping fault segment was added between trench and plate interface because in the JIVSM the plate interface does not reach the seafloor, which allows the rupture to reach the trench. In this work, we exclude this dipping fault segment and consider buried rupture only, for simplicity, because this fault segment is somewhat artificial in the narrow rupture zone of the Sanriku earthquake. The top of the fault is only about 0.3 km or less below the trench based on the JIVSM. We consider a fault 240 km along strike and 65 km along dip to include the entire sedimentary wedge (Figure 4.1). The actual rupture zone is less than 40 km wide and ~200 km long controlled by the fault frictional parameters (see Figure 4.2). The fault covers largely the same area considered in Satake et al. (2017); they used an 8° dipping planar plate interface. We add the ocean in the same way as in part

96

1 (Figure 4.1). The coordinate system used in this work is shown in Figure 4.1: x is along E5°S, y along N5°E, and the origin is at the epicenter (144°E, 39.5°N).

To set up the initial fault stress and stress and pore pressure in the sedimentary wedge, we use the 3D critical wedge solution derived in Ma (2023), which gives rise to stresses in the wedge as well as on the fault for oblique plate convergence. The solution is an extension of 2D critical wedge solution of Dahlen (1984) assuming a normal plate convergence to wedge. In part 1, we abandoned the fault stress from the critical solution and used the fault stress derived from the heterogeneous stress drop model of Kubota et al. (2022) to match the observations. Limited observations were available for the 1896 Sanriku earthquake and such a stress drop model is unavailable. We choose to use the fault stress from the critical solution directly for simplicity, as in Ma & Nie (2019), which is self-consistent with stress and pore pressure conditions in the wedge. Future work can incorporate more heterogeneities in the model. The surface slope and fault dip are obtained by fitting the data in the northern Japan Trench in the finite element mesh (Supplemental Figure 4.1), which are 5.475° and 4.7313°, respectively. The maximum compressive direction is assumed along the plate convergence direction, E20°S, and makes an inclination angle 8° from wedge slope. The rake of initial shear stress on the fault is assumed 87°. Assuming the initial frictional coefficient at the base of wedge is 0.25, the 3D critical wedge solution directly gives the pore pressure ratio 0.5856 (slightly overpressured) and internal friction 0.3261. The detail of the 3D critical solution can be seen in Appendix of Ma (2023). The inclination angle used here is smaller than the 15° used in Ma (2023) and part 1 because this angle largely controls the fluid pressure in the wedge. Larger angles lead to larger fluid overpressure, giving rise to too small stress drop for modeling the 1896 Sanriku earthquake.

The rake angle is an important parameter in our models as it controls the amplitudes of on-fault shear stresses along strike and dip. The chosen rake angle due to oblique plate convergence leads to a small left-lateral strike-slip component. If we define x' as the direction along dip, y' along strike, and z' perpendicular to the fault plane (see Figure A1 in Ma, 2023), the shear stress $\sigma_{z'y'}$ determines the shear stress $\sigma_{y'x'}$ in the critical solution, which plays an important role in mode III ruptures (Andrews, 1976, 2004). The rupture propagation in the Sanriku earthquake is mostly along strike (mode III rupture). Along $+y'$ (north) large dynamic shear stress carried by rupture front reduces the amplitude of $\sigma_{y'x'}$, while along $-y'$ (south) the amplitude of $\sigma_{y'x'}$ is increased by rupture front. In mode III ruptures the change in $\sigma_{y'x'}$ is directly proportional to slip velocity and if this stress is limited by yielding it has the effect of limiting slip velocity (Andrews, 1976, 2004). Only stress components $\sigma_{y'x'}$ and $\sigma_{z'x'}$ are important in controlling yielding in model III. Thus, the inelastic yielding will only occur in $-y'$ direction for mode III rupture because of the increase of $\sigma_{y'x'}$ amplitude by rupture front, while along $+y'$ direction rupture front moves the material away from yielding by reducing the $\sigma_{y'x'}$ amplitude. Inelastic yielding contributes to fracture energy in controlling rupture velocity. So, the rupture and slip velocities only to the south of hypocenter are limited by yielding, while to the north they are similar to those of an elastic model. If we decrease the rake angle, so the amplitude of initial $\sigma_{y'x'}$ is larger; southward rupture propagation will be limited to shorter extent while northward rupture is unaffected by yielding. If the rake angle is 90° (on-fault shear stress is along x' only) rupture and slip velocities cannot be controlled by yielding in the mode III direction, as in Ma & Nie (2019). Yielding still occurs at shallow depths due to mixed mode rupture but does not control rupture velocity at depth. These important results will be shown below.

Similar to part 1, we will consider both elastic and inelastic models for the 1896 Sanriku earthquake. For the inelastic models, we use the Drucker-Prager yield criterion (Drucker & Prager, 1952). The 3D critical solution gives initial stresses, pore pressure, and internal friction in the wedge. To determine cohesion, we define a closeness-to-failure parameter (CF), which is the ratio of square root of second invariant of deviatoric stress tensor to yield stress (see equation 9 in Ma, 2023). To consider along-strike variation of sediment thickness we specify CF as a function of y. CF is 0.7 for $y < -120$ km and 0.9 for $y > -60$ km, and varies smoothly as a cosine function from 0.7 to 0.9 for -120 km $< y <$ -60 km. The functional form can be seen in equation 10 in Ma (2023). The CF value directly gives wedge cohesion as all the other parameters in the yield criterion are given by the critical wedge solution. The larger CF mimics lower strength, which may relate to sediment thickness in the northern Japan Trench.

We use the rate-and-state friction with slip law for state evolution (see equations 1 – 6 in Ma, 2023) and standard frictional parameters to model dynamic rupture, as in part 1. Figure 4.2 shows the distributions of a-b and initial normal stress on fault. The parameter b and state evolution distance L are 0.014 and 0.6 m everywhere on the fault. We confine the rupture zone less than 40 km wide, similar to that in the northern Japan Trench in part 1 and Ma (2023), by increasing a-b linearly from -0.004 to 0.004 from 30 km to 35 km from trench. The rupture will penetrate the deep velocity-strengthening region to certain extent. At shallow depth we also include a velocity-strengthening region, where a-b increases linearly from -0.004 to 0.004 over 5 km from 10 km to 5 km from trench. The velocity-strengthening region is also placed on the northern and southern ends of rupture zone, to confine the rupture length ~200 km. Despite constant wedge slope and fault dip are used in the 3D critical wedge solution, the fault and slope are slightly nonplanar, which results in the small variation of initial normal stress on fault, but the normal stress increases

approximately linearly with depth. The initial frictional coefficient on fault also fluctuates slightly around 0.25, the value used in the critical solution. In Ma (2023) and part 1, the velocity-weakening region extended all the way to the trench in the northern Japan Trench as the stress drop model of Kubota et al. (2022) showed positive stress drop at shallow depths. Here we consider the velocity-strengthening friction at shallow depths, as expected from shallow subduction zones (e.g., Scholz, 1998). The results for a shallow velocity-weakening zone will also be shown. The narrow shallow velocity-strengthening region (~5 km wide) is due to the overall narrow rupture zone. The other frictional and undrained poroelastic parameters are identical to those in Ma (2023).

We nucleate the rupture by applying a 2D Gaussian perturbation in shear stress over 1 s on the fault (the standard deviation and peak amplitude of the Gaussian function are 2500 m and 15% of the background shear stress, respectively) centered on the hypocenter. The hypocentral depth is 10.16 km based on the JIVSM. Due to the uncertainty in the hypocentral location of the 1896 earthquake we also consider two other hypocenters for the models, located at (0, -60 km) and (0, 60 km) with hypocentral depths of 9.96 km and 10.36 km, respectively.

Due to a smaller rupture zone than part 1, we can discretize sedimentary wedge using 250 m 4-node tetrahedral elements, resulting in the element size on fault ~250 m. The ocean is meshed using 500 m tetrahedral elements. The mesh gradually coarsens to a remote boundary. Each model is run for 300 s with 0.01 s time step.

4.3. Results

We show snapshots of slip velocity, shear stress change, vertical seafloor velocity, dynamic ocean bottom pressure (OBP) change, and sea surface elevation for the fully coupled elastic and inelastic model in Figures 4.3 and 4.4. The detailed rupture processes and development of inelastic

strain in the sedimentary wedge in the inelastic model are illustrated in Movies 4.1 and 4.2. After nucleation the rupture propagates in all directions with faster rupture velocity along dip (mode II) than along strike (mode III). As the hypocenter is only ~20 km down dip from trench, the rupture reaches the trench at ~14 s, exciting PL waves propagating landward (e.g., Kozdon & Dunham, 2014) and oceanic Rayleigh waves into deep ocean. Large inelastic deformation occurs as the rupture propagates up dip from hypocenter into the shallow velocity-strengthening region in the inelastic model, generating much larger seafloor uplift than the elastic model. The increase of shear stress on fault promotes inelastic failure enhancing uplift, while in the elastic model the velocity-strengthening friction decreases slip and uplift. Ocean acoustic waves from down-dip rupture from the hypocenter are the first waves propagating landward. The down-dip rupture soon dies out in the deep velocity-strengthening region. The rupture in both models is seen to propagate predominantly along strike thereafter. Although the shear stress changes prescribed in both models are the same the two models are distinctly different. In the elastic model rupture propagates with fast rupture velocity and large slip velocity (>5 m/s). The rupture front is seen as narrow pulses, generating strong waves trapped within the sedimentary wedge behind the rupture front. Large PL and oceanic Rayleigh waves are seen to radiate from the trapped energy behind the rupture fronts. In contrast, little radiation from the rupture fronts in the inelastic model is seen. The rupture velocity and slip velocity are much smaller. The excitation of ocean acoustic waves and trapped energy behind the rupture front are much weaker. However, the tsunami from the inelastic model is several times larger than that from the elastic model.

We observe a faster rupture velocity and shallower inelastic deformation zone to the north than the south in the inelastic model. This is the role of shear stress $\sigma_{y'x'}$ in controlling the yielding for mode III ruptures, mentioned earlier. To the north, the dynamic shear stress associated with

rupture front decreases the amplitude of $\sigma_{y'x'}$, thus moving material away from failure. The inelastic deformation is not seen at depth. The shallow inelastic deformation is due to yielding caused by other stress components in mixed-mode rupture. The rupture front to the south instead increases the amplitude of $\sigma_{y'x'}$ to promote inelastic deformation at depth, leading to slower rupture propagation, smaller slip velocity, and weaker radiation.

Figure 4.5 compares the seafloor displacements at 5 cross sections between the two models at 300 s. Significant seafloor uplift is caused by inelastic wedge deformation, several times larger than the elastic uplift. The difference between the inelastic wedge deformation in the north and south is also clearly seen. The inelastic zone to the south is wider than the north and peak uplift is in the north, indicating more intense and localized inelastic deformation in the north, which is likely driven by the fast rupture velocity at depth. The yielding in the south causes broader inelastic deformation, which slows down the rupture at depth, but the uplift is smaller.

We compare the slip and horizontal and vertical seafloor displacements between the two models at 300 s in Figure 4.6. It is somewhat surprising that the peak slip in the inelastic model is larger than the elastic model and there seems a large slip patch stretching in all directions from the hypocenter leading to larger horizontal displacement. The peak uplift is more than three times larger in the inelastic model. The width of the seafloor uplift in the inelastic model is significantly narrower than the elastic model. The narrower inelastic zone in the north leads to narrower uplift than in the south. The rupture length in the elastic model is ~200 km controlled by the prescribed frictional parameter $a - b$ (Figure 4.2), while it is ~180 km in the inelastic model. The shorter rupture length in the inelastic model is due to rupture dying out by yielding controlled by the stress $\sigma_{y'x'}$ in the south. No yielding occurs at depth to the north, so the rupture propagates all the way to the prescribed velocity-strengthening region, as in the elastic model. From the rupture time

contours we can see the rupture velocity to the south (< 1 km/s) is smaller than to the north (~1.2 km/s) in the inelastic model. The rupture velocity to the north is identical to the rupture velocity to both directions in the elastic model, largely controlled by the S-wave speed of the sediment (1.5 km/s).

Supplemental Figure 4.2 shows the results when we change the shallow velocity-strengthening region to velocity-weakening. Peak slip changes only slightly from 16.93 m to 18.35 m in the elastic model. Peak uplift increases slightly from 2.10 m to 2.23 m. In the inelastic model, rupture slows down before reaching about $y = -90$ km and then accelerates and reaches about the same extent as in the elastic model. The peak slip increases from 22.12 m to 25.64 m; however, the peak uplift reduces from 6.75 m to 6.56 m, indicating higher efficiency of generating seafloor uplift by inelastic deformation in the velocity-strengthening region. The rupture velocity pattern is largely similar to Figure 4.6 for the velocity-strengthening cases.

To find out why the slip in the inelastic model is larger, we show the space-time plots of slip velocity and shear stress change along $y = 0$ as well as relevant time histories at a closest node to the hypocenter (Figure 4.7). Although the shallow velocity-strengthening zone is present the rupture propagates up dip with a nearly constant sub-Rayleigh rupture velocity in the elastic model, due to strong effects of free surface and bimaterial interface unclamping the fault (Ma & Beroza, 2008). Little reflection is generated at the trench due to frictional increase in the velocity-strengthening region. The slowing down of deep rupture into the velocity-strengthening region is clearly seen. However, in the inelastic model, a very slow rupture propagation up dip is seen, due to inelastic wedge deformation (Figure 4.5), enhanced by shear stress increase above the velocity-strengthening region. Notice the pronounced longer duration of slip velocity up dip from the hypocenter in the inelastic model (Figure 4.7a, b), leading to little high-frequency radiation.

The longer slip duration is also seen at the hypocenter in the inelastic model (Figure 4.7e). Due to a shallow hypocentral depth and large CF used in the model, inelastic wedge deformation occurs up dip from the hypocenter shortly after nucleation (see Movie 4.2). The inelastic deformation causes more gradual shear stress reduction (Figure 4.7f), giving rise to ~10 s longer slip duration at the hypocenter, which leads to larger slip in the inelastic model. The same mechanism occurs in a large patch around the hypocenter, which explains the larger slip pattern shown in Figure 4.6. This is similar to the >100 m slip patch at shallow depth with modest inelastic deformation, presented in part 1. Here the inelastic deformation around the hypocenter is also modest due to large confining pressure although the CF is large, so the peak slip rate remains identical to the elastic case and peak slip increases because of longer duration. With significant inelastic deformation, peak slip rate is reduced, and slip is diminished despite longer duration, as seen at shallower depths (Figures 5 – 7). In part 1, the modest inelasticity is due to a smaller CF, inelastic deformation occurs near trench due to large stress change and low confining pressure. The hydroacoustic dilation by the ocean also contributes to the longer slip duration, but here it is very small due to a large depth (~10 km).

The seismic potency of the elastic model is 5.1350 x 10^{10} m^3. The total seismic potency of the inelastic model is 5.1364 x 10^{10} m^3, with a ratio of seismic potency in the wedge (inelastic strain is volume density of seismic potency) to the fault 0.2953. The beachball of potency in the wedge shows a vertical-CLVD-T focal mechanism (Figure 4.6), as expected from horizontal compression and vertical extension of inelastic deformation. Assuming a shear modulus 5.06 GPa of wedge sediment in the model, the moment magnitude for both models is M_W 7.54. Due to ambiguity of seismic moment on a bimaterial plate interface in the models (e.g., Ampuero & Dahlen, 2005), if 20 GPa is assumed the moment magnitude for both models are M_W 7.94, close

to the moment magnitude of the 1896 earthquake. Standard approaches, such as CMT solutions, determine moment magnitude without considering material properties in the source region, which may overestimate the magnitudes of shallow subduction earthquakes (e.g., Polet & Kanamori, 2000). The moment magnitude for the 1896 Sanriku earthquake by Utsu (1979) was obtained by aftershock distribution, which may contain large uncertainties.

The different radiation characteristics between the elastic and inelastic models are also illustrated in the space-time plots of vertical seafloor velocity and dynamic ocean bottom pressure change (Figure 4.8). The PL waves generated from updip rupture hitting the trench and by rupture fronts propagating along strike are marked. The large amplitude waves trailing behind the rupture front and strong oceanic Rayleigh waves are clearly seen in the elastic model. However, all these features are nearly diminished in the inelastic model, consistent with Figures 4.3 and 4.4. The radiation to the south is much weaker than to the north in the inelastic model, reflecting the difference in yielding at depth. The radiation from deep rupture to the north in the inelastic model is similar to that in the elastic model. The yellow strips in vertical seafloor velocity at shallow depths in the inelastic model reflect slow and long rupture propagation caused by inelastic deformation as shown in Figure 4.7b. The yellow strips are shorter to the north of hypocenter because inelastic deformation is more limited to shallow depths (Figure 4.5). Little radiation can be seen from yellow strips in both directions in the inelastic model, distinctly different from the elastic model. Similar features can also be seen from the dynamic ocean bottom pressure changes associated with rupture front.

Figure 4.9 shows the space-time plots of sea surface elevation at 5 cross sections between the two models. Clearly larger tsunami in the inelastic model is seen. Ocean acoustic waves are also present in the figure. Same as in part 1, we define the efficiency of tsunami generation as the

sea surface elevation normalized by average slip along each cross section. Because the average slip is larger around the hypocenter in the inelastic model the efficiency of tsunami generation is slightly reduced at $y = 0$. However, larger efficiency in the inelastic model is clearly seen at all the cross sections. Again, this is due to frictional sliding on conjugate Coulomb microfractures with steeper dips than that of the plate interface, modeled by inelastic deformation.

Figures 4.10 – 4.12 detail the waveforms of vertical seafloor velocity, dynamic ocean bottom pressure change, and sea surface elevation at the 5 cross sections. Again, the strong radiation of ocean acoustic waves in the elastic model and weak radiation in the inelastic model are clearly shown. However, the tsunami in the inelastic model is significantly larger. We see large and long-duration vertical seafloor velocity at 10 km to trench, which leads to large seafloor uplift (after time integration). These long-duration velocity pulses correspond to the yellow strips in Figure 4.8. The duration of pulses is ~10 s to the north of hypocenter and is longer to the south; the duration reaches ~25 s at $y = $ -60 km, reflecting the slower rupture propagation to the south. The long-duration velocity pulses are also seen on the horizontal seafloor velocity (Supplemental Figures 4.3 and 4.4).

Due to the uncertainty in the hypocentral location of the 1896 Sanriku earthquake we also run two additional inelastic rupture scenarios with different hypocenters. One has the hypocenter located at (0, -60 km) and the other with hypocenter at (0, 60 km). All other rupture parameters remain the same. Movies 4.3 and 4.4 show the details of these rupture scenarios. Both ruptures have longer duration due to predominantly unilateral rupture propagation (Figure 4.13). For northern hypocenter the southward rupture is particularly slow. The rupture slows down significantly between $y = 0$ and $y = 30$ km, then continue southward with very slow rupture velocity (<1 km/s), making the total duration over 200 s. When the hypocenter is in the south the rupture

propagates northward faster (~1.2 km/s), which is again due to the role of shear stress $\sigma_{y'x'}$ in the yielding for mode III ruptures. Yielding only occurs at depth for southward rupture, limiting rupture velocity, slip velocity, rupture propagation distance, and radiation. The inelastic deformation occurs mostly at shallow depth for northward rupture, resulting in a narrower inelastic seafloor uplift and larger peak uplift (7.04 m). Both ruptures have weak radiation from the trench due to significant inelastic wedge deformation, but the radiation for southward rupture (northern hypocenter) is significantly weaker than northward rupture (southern hypocenter), as seen mostly in energy trapped behind rupture front (Figure 4.14). Although the tsunami is larger for northward rupture the efficiency of tsunami generation is similar between the two ruptures (Figure 4.15). The potency ratio between the wedge and fault is 0.2683 (southern hypocenter) and 0.3 (northern hypocenter) for these two models. Movies 4.5 and 4.6 and Supplemental Figure 4.5 show the results of the elastic models for these two scenarios. The rupture velocity is nearly constant and radiate strong acoustic waves from the rupture front. The peak uplift is more than $2 - 3$ times smaller than that of the inelastic models.

We show the potency rate functions for both elastic and inelastic models and all three hypocenter locations (Figure 4.16). The potency rate time functions within the wedge are also shown for the inelastic models. Inelastic models tend to have longer durations due to slower rupture velocity. When the hypocenter is in the center the duration for the inelastic model is shorter; this is because the longer rupture propagation distance in the elastic model (Figure 4.6). Despite different rupture velocity and very different radiation characteristics between elastic and inelastic models the potency rate functions are all smooth and have similar spectral decay, different from the result in Ma & Hirakawa (2013). This is because the models here do not have strong rupture breakout at trench due to a shallow velocity-strengthening region and buried ruptures. All the

models are shallow subduction events. A larger difference between deep rupture and shallow rupture may exist, as shown by Lay et al. (2012) and Ma & Hirakawa (2013). On the other hand, the results here show that the potency (or moment) rate time function may not well represent the radiation characteristics of earthquakes because it assumes a point source and rupture complexities are averaged out.

Inelastic wedge deformation contributes to seismic potency (moment), however, is a large energy sink due to plastic dissipation (Ma & Hirakawa, 2013). Ma & Hirakawa (2013) derived the energy balance equations for inelastic deformation. We calculate the radiated energy for each rupture scenario based on equations 1, 2, 4, and 5 in Ma & Hirakawa (2013) and results are shown in Table 1. The less radiated energy in the inelastic models than the elastic models is clearly seen. The shear modulus 5.06 MPa of wedge sediment is used to calculate moment. The moment-scaled radiated energy for three elastic models is similar to typical crustal earthquakes, such as the 2004 Parkfield earthquake (Ma et al., 2008). Larger shear modulus would make the moment-scaled radiated energy lower. Perhaps most importantly, the moment-scaled radiated energy for the elastic model is 6.28, 5.29, and 11.20 times larger than that of inelastic model for all the 3 cases (central, southern, and northern hypocenters), respectively, irrespective of shear modulus being used, consistent with the observations of tsunami earthquakes (Newman & Okal, 1998; Lay et al., 2012). Inelastic deformation thus provides an explanation to this anomalous characteristic of tsunami earthquakes, suggested by Ma & Hirakawa (2013).

Table 4.1. Seismic potency, moment, and radiated energy for 6 rupture models

	Central hypocenter		Southern hypocenter		Northern hypocenter	
	elastic	inelastic	elastic	inelastic	elastic	inelastic
Potency (m^3)	5.14×10^{11}	5.17×10^{11}	4.76×10^{11}	6.08×10^{11}	4.87×10^{11}	4.46×10^{11}
Moment (Nm)	2.60×10^{20}	2.62×10^{20}	2.41×10^{20}	3.08×10^{20}	2.47×10^{20}	2.26×10^{20}
Radiated energy (J)	3.13×10^{15}	5.04×10^{14}	2.77×10^{15}	6.70×10^{14}	3.39×10^{15}	2.77×10^{14}
E_R/M_0	1.21×10^{-5}	1.93×10^{-6}	1.15×10^{-5}	2.17×10^{-6}	1.38×10^{-5}	1.23×10^{-6}

4.4. Discussion and Conclusions

We have presented fully coupled models of dynamic rupture, ocean acoustic waves, and tsunami for the 1896 Sanriku earthquake. Realistic bathymetry, fault geometry and velocity structure from the JIVSM, and along-strike variation of sediment thickness in the Japan Trench are incorporated. The modeled rupture zone is within 40 km from trench and below thick sediment in the northern Japan Trench, which is shown to have significant effects on rupture dynamics, seismic and acoustic radiations, and tsunami generation. Although sediment has long been realized to play an important role in deficiency in high-frequency radiation of tsunami earthquakes due to its low rigidity our models show that sediment in an elastic setting leads to strong high-frequency radiation, contradicting the observations.

Weak strength of sediment is at least as important as low rigidity, which has largely been overlooked. Our models show that inelastic deformation can occur in the sedimentary overriding wedge due to weak strength, which acts as a large energy sink and causes slow rupture propagation, deficiency in high-frequency radiation, and low moment-scaled energy. Nearly all the seismic and ocean acoustic radiations (mostly PL and oceanic Rayleigh waves) are strongly diminished by inelastic deformation. Little radiation is shown from the rupture front. The moment-scaled energy

of inelastic models can be an order smaller than that of elastic models. Meanwhile frictional sliding on conjugate Coulomb microfractures during inelastic deformation generates seafloor uplift more efficiently than slip on a shallowly dipping plate interface. The seismic potency due to inelastic deformation shows a clear vertical-CLVD-T focal mechanism. Our models with velocity-strengthening friction at shallow depth show that inelastic wedge deformation enhanced by shear stress increase on fault causes seafloor uplift 2-3 times larger than purely elastic models. Carvajal et al. (2022) showed that buried ruptures at shallow depth are more efficient in generating seafloor uplift than trench-breaking ruptures in their 2D elastic dislocation models. However, higher efficiency of tsunami generation by inelastic deformation than buried ruptures is clearly shown here. Inelastic deformation in the overriding wedge due to weak sediment thus provides a unifying interpretation to nearly all anomalous characteristics of the 1896 Sanriku earthquake and other tsunami earthquakes. The large inelastic uplift shown in Figures 6 and 13 may be misinterpreted as large shallow slip or submarine landslides depending on the physics of tsunami generation assumed in a particular study.

The 1896 Sanriku earthquake, as most other tsunami earthquakes, propagated mainly along strike, which is a predominantly mode III rupture. We have shown that the anti-plane shear stress $\sigma_{y'x'}$ (y' is along strike and x' along dip) plays an important role in controlling yielding in mode III ruptures. This stress component is reduced by northward rupture but increased by southward rupture, given the oblique plate convergence and stress setting in the northern Japan Trench. Thus, yielding occurs mostly to the south of hypocenter at depth. The limit on this stress component placed by yielding reduces rupture velocity and radiation to the south. While the northward rupture prevents yielding at depth, so rupture velocity is mostly controlled by the S wave of sediment. In both rupture directions yielding occurs at shallow depth due to stresses in mixed rupture mode.

However, the inelastic zone to the north is narrower than the south. This finding should not be confused with the slow northward rupture propagation (~850 m/s) in the northern Japan Trench in Ma (2023) and part 1. The inelastic deformation in those models is caused by rupture deeper than sedimentary wedge and large dynamic stresses ahead of rupture front. Heterogeneous stress and fault friction along strike should also play an important role in rupture velocity and radiation, which will be addressed in future work.

Due to weak high-frequency radiation of ocean acoustic waves their use for tsunami early warning is probably cautioned, which was pointed out in part 1. Due to high-frequency nature of these waves they are unlikely to carry useful information of tsunami, which have much longer periods and are more sensitive to static deformation. The problem may be similar to constraining seismic moment by long-period surface waves.

Finally, we find that inelastic deformation can lead to long-duration velocity pulses, which have important implications to the long-period ground motion observed in the 1999 ChiChi earthquake and many other surface-rupturing earthquakes (see Burks & Baker, 2016, for a compilation of these records).

Acknowledgements

Chapter 4, in full, is currently being prepared for submission for publication of the material. Du, Yue; Ma, Shuo. The dissertation author was the primary investigator and author of this material.
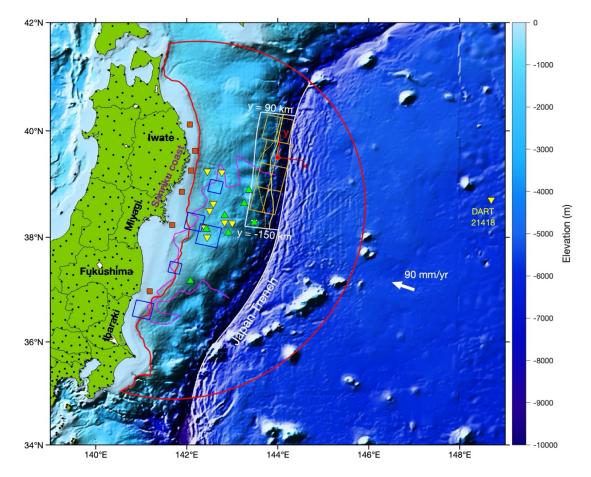
Figure 4.1. Map of the study. The white box denotes the fault used in this work. The 8 yellow rectangles are the subfaults to model the 1896 Sanriku earthquake in Satake et al. (2017). The 1896 epicenter (144°E, 39.5°) is denoted as a red dot, which is the origin of the coordinate system (*x* is along E5°S and *y* is N5°E, shown in red). The red crescent-shaped curve outlines the ocean of interest in the fully coupled models. Other features are identical to Figure 3.1 of part 1, shown as a reference.
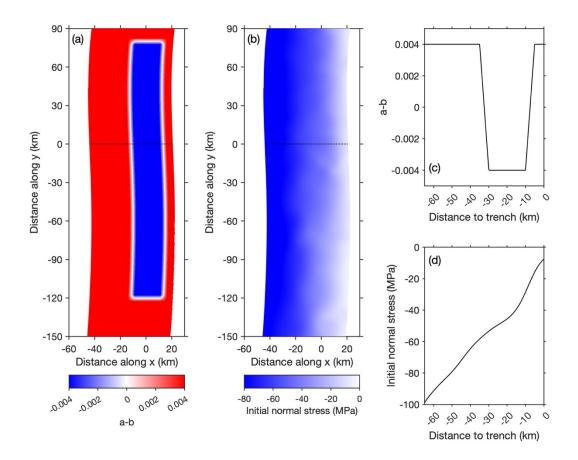
Figure 4.2. Distributions of $a - b$ (a) and initial normal stress (b) are mapped on the fault and a cross section of (a) and (b) along $y = 0$ is shown in (c) and (d), respectively.
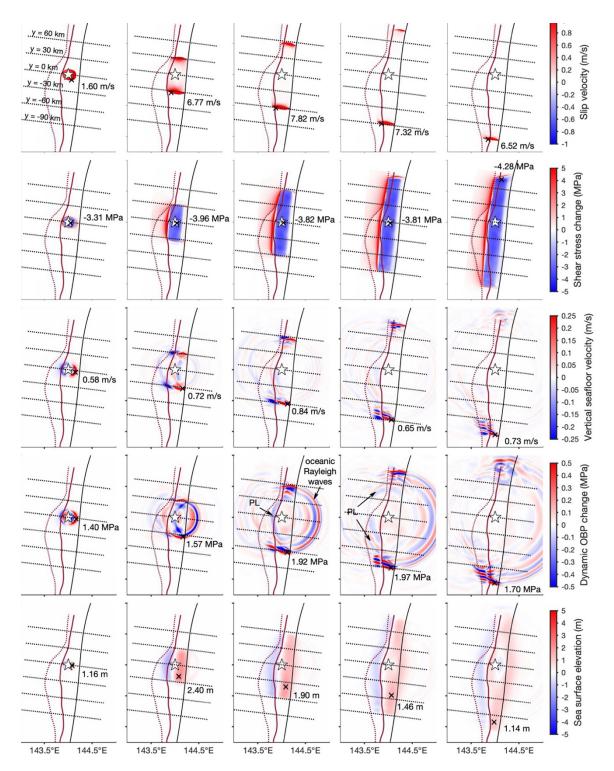
Figure 4.3. Snapshots of slip velocity, shear stress change, vertical seafloor velocity, dynamic ocean pressure change, and sea surface elevation of the elastic model are shown. Strong ocean acoustic waves are radiated from the rupture fronts. Large energy is trapped in the sediment behind rupture fronts. PL and oceanic Rayleigh waves are generated by updip rupture hitting the trench and rupture fronts propagating along strike. The white star denotes the epicenter. The location of peak amplitude (shown by a number) in each panel is marked as a x.
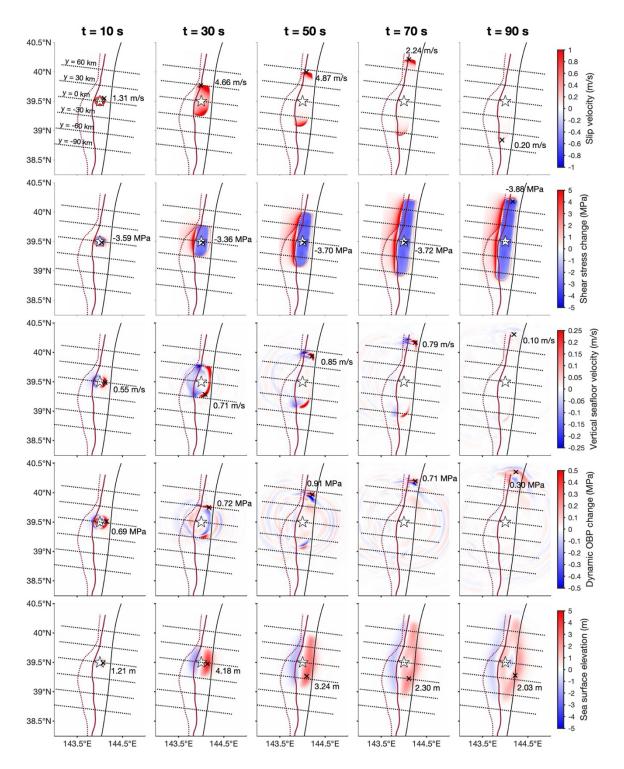
Figure 4.4. Same as Figure 4.3 except for the inelastic model. Significantly weaker radiation but larger tsunami are produced than the elastic model.
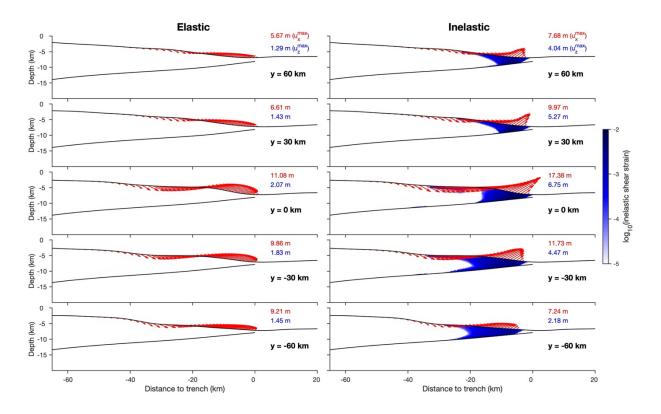
Figure 4.5. Seafloor displacement and inelastic shear strain at $t = 300$ s are shown at 5 cross sections for elastic and inelastic models. Peak horizontal and vertical displacements at each cross section are shown in red and blue numbers, respectively. Significantly larger uplift is generated in the inelastic model.
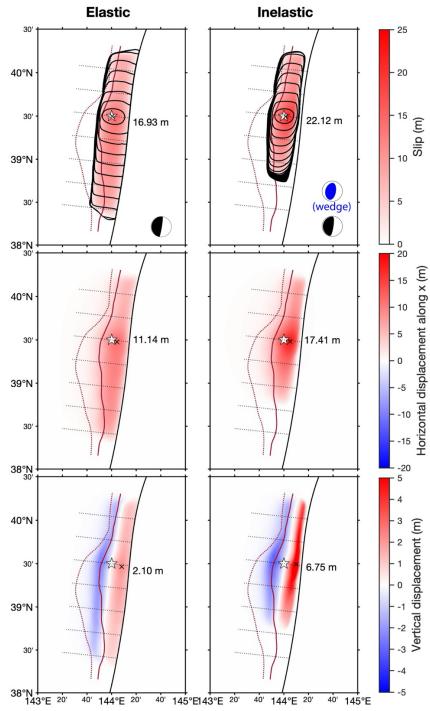
Figure 4.6. Distributions of slip and horizontal and vertical seafloor displacements are compared between elastic and inelastic models. The black beachball in the first row shows the focal mechanism of each model. The blue beachball shows a clear vertical-CLVD-T focal mechanism of seismic potency due to inelastic wedge deformation. The peak uplift in the inelastic model is more than 3 times larger than in the elastic model. The larger peak slip in the inelastic model is due to increase of slip duration by inelastic deformation shown in Figure 4.7. In the inelastic model the rupture velocity to the south is slower and the uplift is wider but smaller in the south.
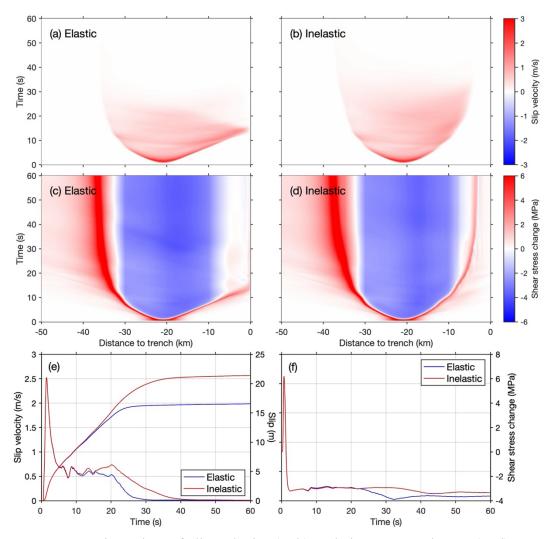
Figure 4.7. Space-time plots of slip velocity (a, b) and shear stress change (c, d) are compared between elastic and inelastic models. Time histories of slip velocity and shear stress change at the closest point to the hypocenter are shown in (e) and (f). Longer duration of slip can be clearly seen in (b) than (a), as well as in (e). The shallow velocity-strengthening region increases shear stress, promoting inelastic deformation in the wedge, and causes slow rupture propagation, increasing slip duration at shallow depths. The longer slip duration at depth in (e) is due to more gradual stress change caused by inelastic deformation, resulting in larger slip in the inelastic model.
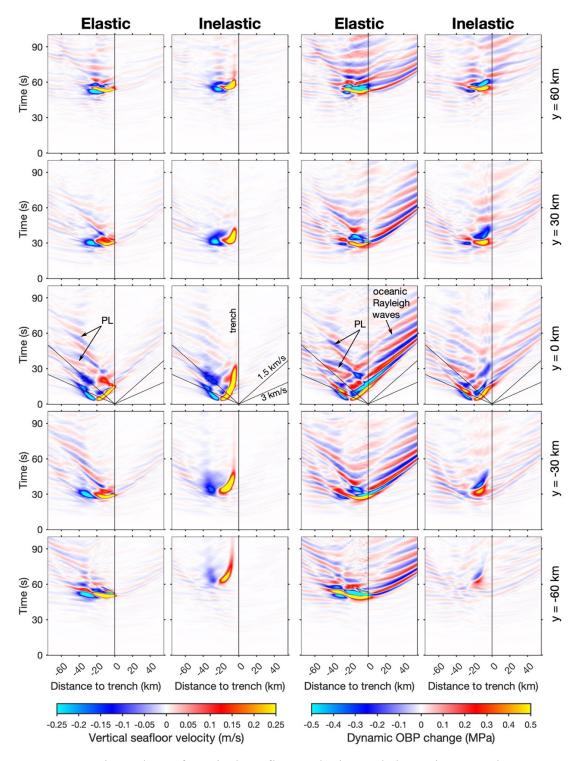
Figure 4.8. Space-time plots of vertical seafloor velocity and dynamic ocean bottom pressure change at 5 cross sections are compared between elastic and inelastic models. Stronger PL and oceanic Rayleigh waves are radiated from rupture front in the elastic model. Little radiation is seen from the rupture front in the inelastic model. In the inelastic model, radiation at rupture front is weaker to the south of hypocenter than to the north due to inelastic deformation at depth. The slopes of straight lines correspond to P and S wave speeds of wedge sediment.
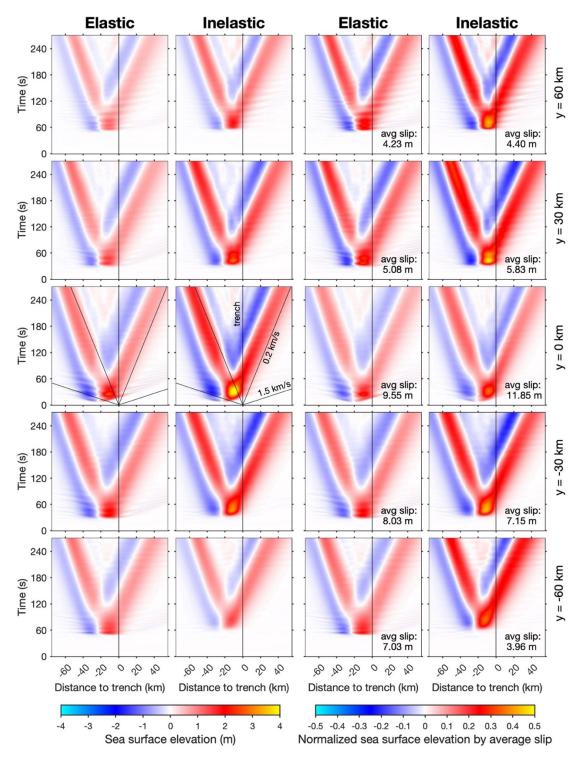
Figure 4.9. Space-time plots of sea surface elevation and normalized sea surface elevation by average slip are compared between elastic and inelastic models. Larger tsunami and higher efficiency of tsunami generation are observed in the inelastic model.
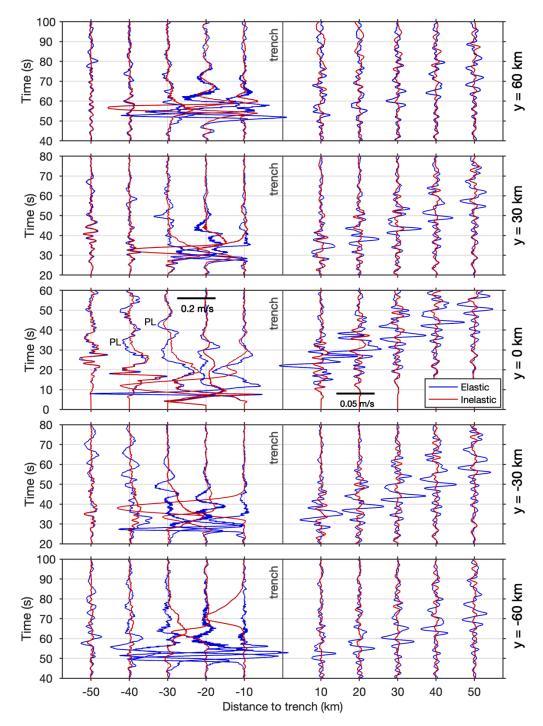
Figure 4.10. Time histories of vertical seafloor velocities are compared between elastic and inelastic models. Stronger radiation is seen in the elastic model. Large long-duration seafloor velocities are seen in the inelastic model, reflecting slow motion due to enhanced inelastic deformation by velocity-strengthening friction on the shallow plate interface, but they are associated with little radiation. The duration of velocity pulses is longer to the south of hypocenter due to the role of $\sigma_{y'x'}$ in enhancing inelastic deformation. PL waves radiated from updip rupture hitting the trench and trapped energy behind rupture fronts along strike are marked.

121
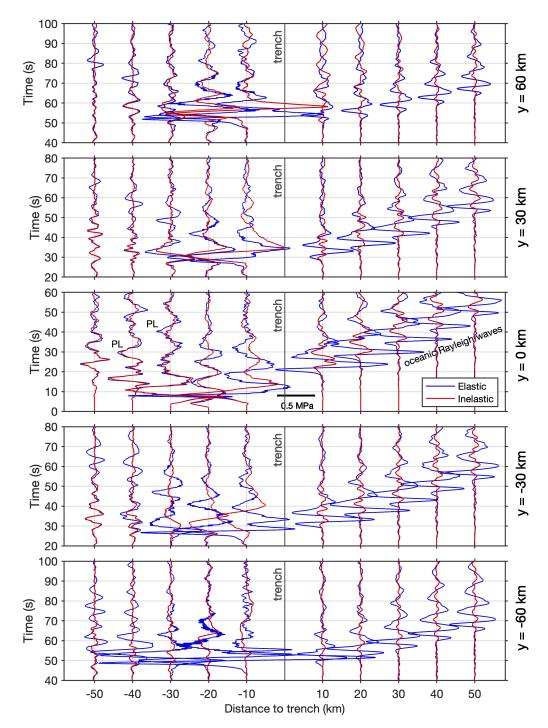
Figure 4.11. Same as Figure 4.10 except for dynamic ocean bottom pressure change.
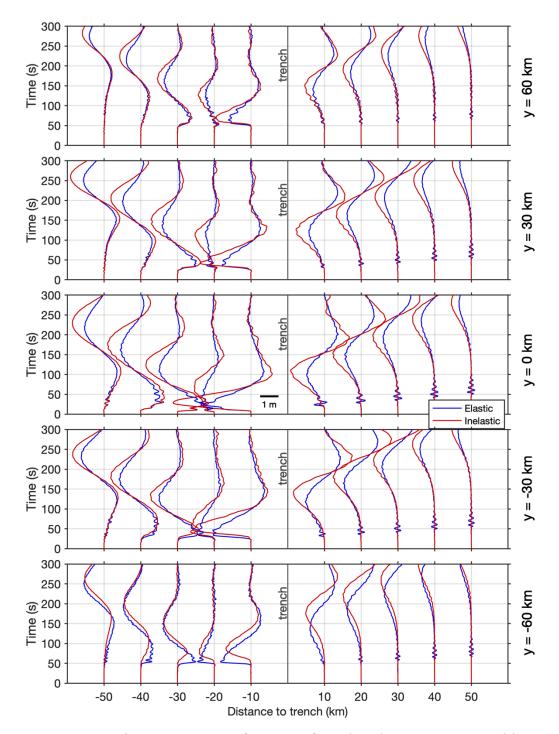
Figure 4.12. Same as Figure 4.10 except for sea surface elevation. Larger tsunami is seen in the inelastic model.
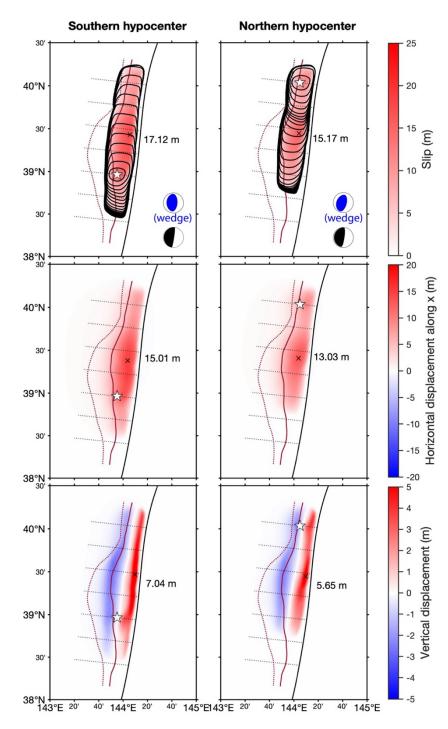
Figure 4.13. Distributions of slip and horizontal and vertical seafloor displacements are compared for ruptures with inelastic wedge deformation and different hypocenter locations. The beachball solutions are shown in the lower right corner of top two panels. The vertical-CLVD-T focal mechanism of inelastic wedge deformation is another manifestation of high efficiency in generating seafloor uplift. The peak amplitude in each panel is shown. The rupture velocity to the south is slower than that to the north in both models due to the role of $\sigma_{y'x'}$ on inelastic deformation at depth.
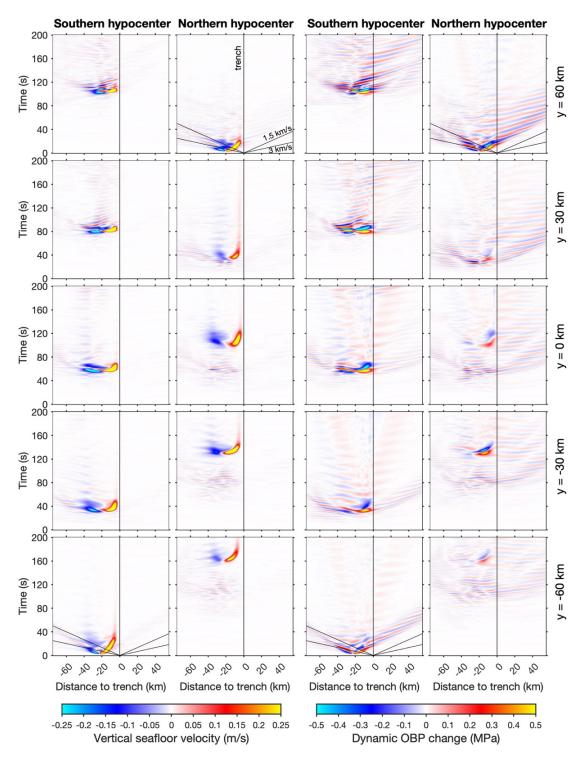
Figure 4.14. Space-time plots of vertical seafloor velocity and dynamic ocean bottom pressure change at 5 cross sections are compared between inelastic models with northern and southern hypocenters. Stronger radiation to the north for a southern hypocenter than to the south for a northern hypocenter is seen. The yellow strip at rupture front in vertical velocity represents slow deformation (the color is saturated) and is shorter to the north and longer to the south, due to the effect of $\sigma_{y'x'}$ on inelastic deformation.
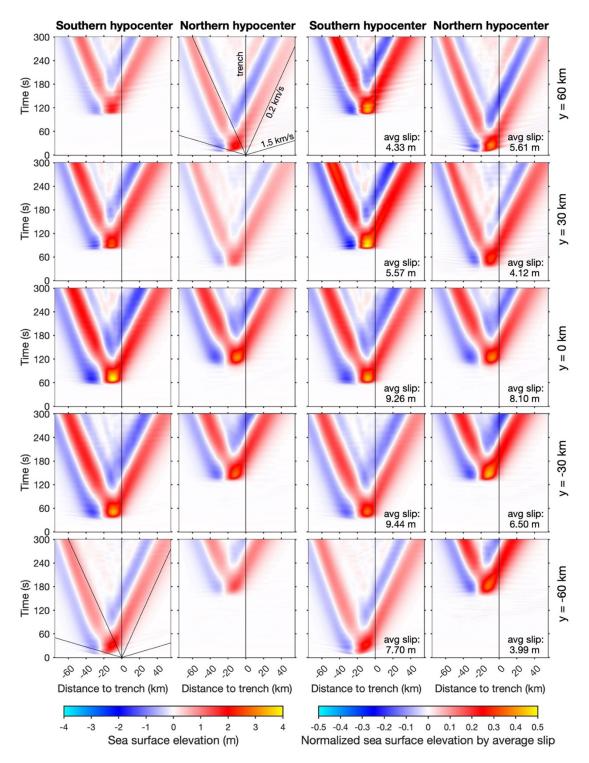
Figure 4.15. Space-time plots of unnormalized and normalized sea surface elevation by average slip at 5 cross sections are compared between inelastic models with northern and southern hypocenters. Northward rupture produces larger tsunami, but the efficiency of tsunami generation is similar between two models.

126
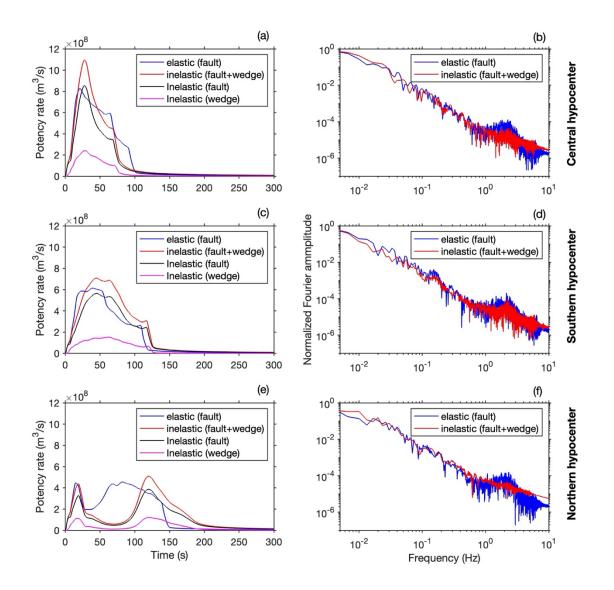
Figure 4.16. Potency rate time functions and spectra for elastic and inelastic models with 3 different hypocenter locations are plotted. The potency rate functions in the wedge in the inelastic models are shown. Inelastic models tend to produce longer rupture duration than elastic models due to slower rupture velocity. The spectra of these potency rate function, however, are similar due to their overall smooth nature.

Supplementary Materials

Movie captions

Movie 4.1. Movie of slip velocity, shear stress change, slip, seafloor vertical velocity, dynamic ocean bottom pressure change, sea surface elevation, and seafloor displacement vectors at 6 cross sections in the elastic model. The dotted lines show the locations of cross sections. The white star denotes the epicenter. The x sign shows the location of peak amplitude at each time instant in each panel (value shown in the upper left corner). Rupture propagates predominantly along strike with fast rupture velocity and large slip velocity, producing strong radiation of PL, oceanic Rayleigh waves and energy trapped within the sediment behind the rupture front. A small tsunami is generated, illustrated in sea surface elevation changes.
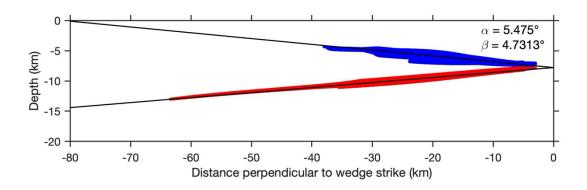
Movie 4.2. Similar to Movie 4.1 except for the inelastic model. Much weaker radiation is seen at the rupture front and a larger tsunami is generated due to inelastic wedge deformation. To the north the rupture velocity is nearly as fast as that in the elastic model and larger than that to the south, producing stronger radiation at rupture front. The inelastic deformation zone is wider to the south generating broader but smaller uplift to the south, which is due to the significant role of $\sigma_{y'x'}$ on inelastic deformation in mode III.

Movie 4.3. Similar to Movie 4.1 except for a southern hypocenter (elastic model).
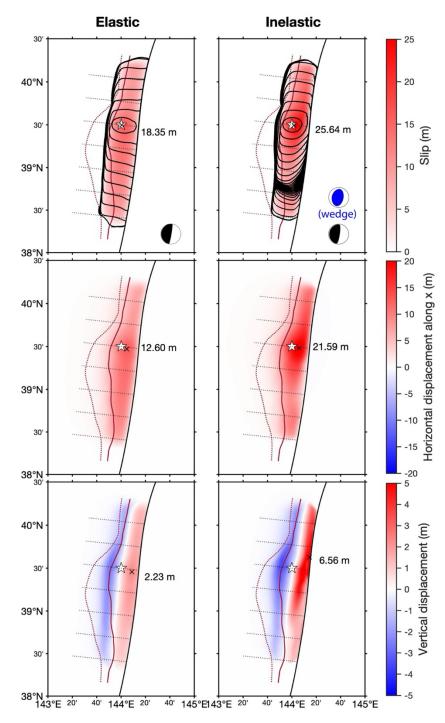
Movie 4.4. Similar to Movie 4.2 except for a southern hypocenter (inelastic model).

Movie 4.5. Similar to Movie 4.1 except for a northern hypocenter (elastic model).
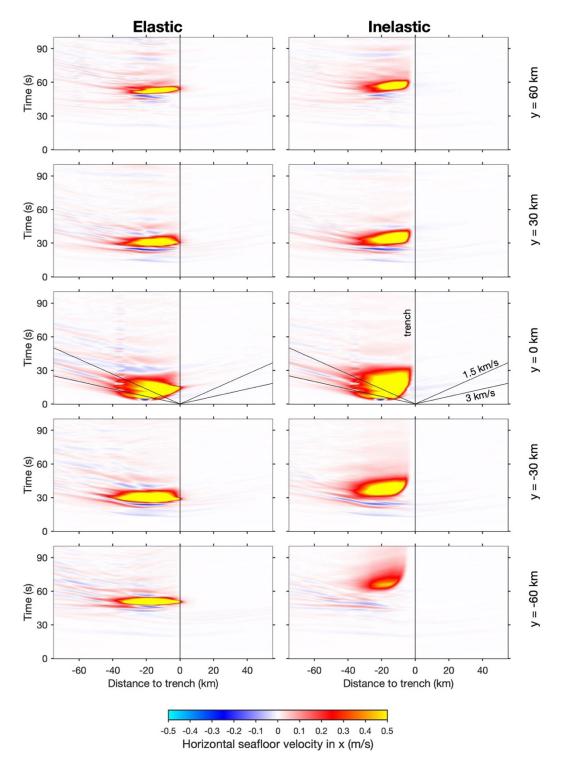
Movie 4.6. Similar to Movie 4.2 except for a northern hypocenter (inelastic model).
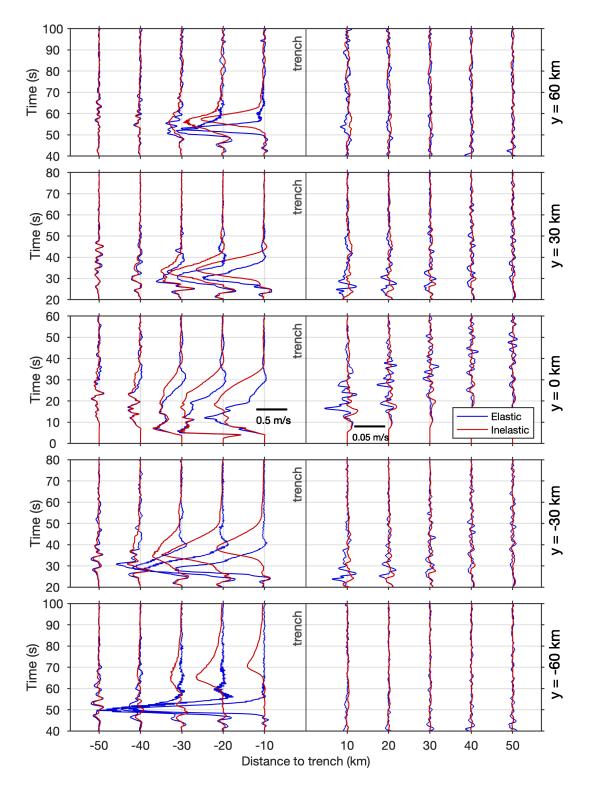
Supplemental Figure 4.1. Projection of all the points at the top and bottom of wedge sediment for $-150 < y < 90$ km in the finite-element mesh onto a plane normal to N5°E. Linear fitting gives the surface slope (α) and basal dip (β) used in the critical wedge solution.
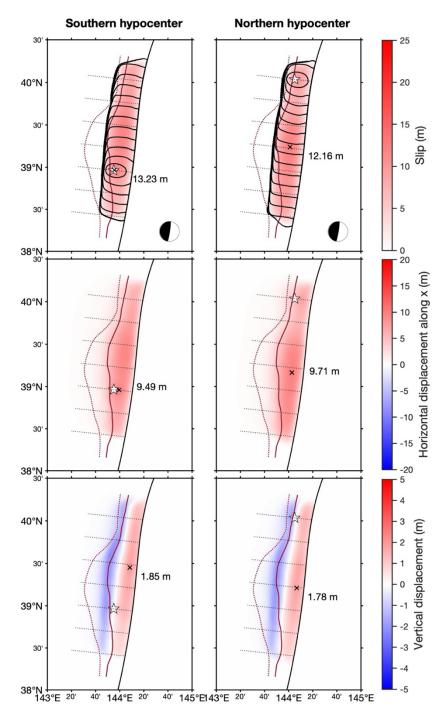
Supplemental Figure 4.2. Same as Figure 4.6 except for the shallow plate interface governed by the velocity-weakening friction.

Supplemental Figure 4.3. Space-time plots of horizontal seafloor velocity (along *x*-direction) at 5 cross sections are compared between elastic and inelastic models. The color is saturated to show small amplitudes.

Supplemental Figure 4.4. Time histories of horizontal seafloor velocity (along *x*-direction) are compared between elastic and inelastic models. Long-duration velocity pulses are clearly seen in the inelastic model. The pulse duration is longer, and amplitude is smaller to the south than the north due to the role of $\sigma_{y'x'}$ on inelastic deformation.

Supplemental Figure 4.5. Distributions of slip and horizontal and vertical seafloor displacements are shown for the elastic models with northern and southern hypocenters. Near constant rupture velocity and small uplift are observed in both models.

REFERENCES

Abe, K. (1978). A dislocation model of the 1933 Sanriku earthquake consistent with the tsunami waves. *Journal of Physics of the Earth, 26*(4), 381–396. https://doi.org/10.4294/jpe1952.26.381

Abrahams, L. S., Krenz, L., Dunham, E. M., Gabriel, A.-A., & Saito, T. (2023). Comparison of methods for coupled earthquake and tsunami modelling. *Geophysical Journal International, 234*(1), 404–426. https://doi.org/10.1093/gji/ggad053

Ampuero, J.-P. (2005). Ambiguity of the moment tensor. *Bulletin of the Seismological Society of America, 95*(2), 390–400. https://doi.org/10.1785/0120040103

Andrews, D. J. (1976). Rupture propagation with finite stress in antiplane strain. *Journal of Geophysical Research, 81*(20), 3575–3582. https://doi.org/10.1029/jb081i020p03575

Andrews, D. J. (2004). Rupture models with dynamically determined breakdown displacement. *Bulletin of the Seismological Society of America, 94*(3), 769–775. https://doi.org/10.1785/0120030142

Andrews, D. J. (2005). Rupture dynamics with energy loss outside the slip zone. *Journal of Geophysical Research*, *110*(B1), B01307. https:// doi.org/10.1029/2004jb003191

Aoi, S., Asano, Y., Kunugi, T., Kimura, T., Uehira, K., Takahashi, N., Ueda, H., Shiomi, K., Matsumoto, T., & Fujiwara, H. (2020). MOWLAS: Nied Observation Network for earthquake, tsunami and Volcano. *Earth, Planets and Space, 72*(1). https://doi.org/10.1186/s40623-020-01250-x

Baba, T., Takahashi, N., Kaneda, Y., Ando, K., Matsuoka, D., & Kato, T. (2015). Parallel implementation of dispersive tsunami wave modeling with a nesting algorithm for the 2011 Tohoku Tsunami. *Pure and Applied Geophysics*, *172*(12), 3455–3472. https://doi.org/10.1007/s00024-015-1049-2

Bilek, S. L., & Lay, T. (2002). Tsunami earthquakes possibly widespread manifestations of frictional conditional stability. *Geophysical Research Letters, 29*(14). https://doi.org/10.1029/2002gl015215

Carvajal, M., Sun, T., Wang, K., Luo, H., & Zhu, Y. (2022). Evaluating the tsunamigenic potential of buried versus trench-breaching Megathrust Slip. *Journal of Geophysical Research: Solid Earth, 127*(8). https://doi.org/10.1029/2021jb023722

Cerjan, C., Kosloff, D., Kosloff, R., & Reshef, M. (1985). A nonreflecting boundary condition for discrete acoustic and elastic equations. *Geophysics*, *50*, 705–708. https://doi.org/10.1190/1.1441945

Cheung, K. F., Lay, T., Sun, L., & Yamazaki, Y. (2021). Tsunami size variability with rupture depth. *Nature Geoscience, 15*(1), 33–36. https://doi.org/10.1038/s41561-021-00869-z

Dahlen, F. A. (1984). Noncohesive critical coulomb wedges: An exact solution. *Journal of Geophysical Research: Solid Earth, 89*(B12), 10125–10133. https://doi.org/10.1029/jb089ib12p10125

Dresback, K. M., Kolar, R. L., & Dietrich, J. C. (2005). On the form of the momentum equation for shallow water models based on the generalized wave continuity equation. *Advances in Water Resources*, *28*(4), 345–358. https://doi.org/10.1016/j.advwatres.2004.11.011

Du, Y., Ma, S., Kubota, T., & Saito, T. (2021). Impulsive tsunami and large runup along the sanriku coast of Japan produced by an inelastic wedge deformation model. *Journal of Geophysical Research: Solid Earth, 126*(8). https://doi.org/10.1029/2021jb022098

Duan, B. (2012). Dynamic rupture of the 2011 MW 9.0 tohoku-oki earthquake: Roles of a possible Subducting Seamount. *Journal of Geophysical Research: Solid Earth, 117*(B5). https://doi.org/10.1029/2011jb009124

Ewing, M., Tolstoy, I., & Press, F. (1950). Proposed use of the T phase in Tsunami Warning Systems*. *Bulletin of the Seismological Society of America, 40*(1), 53–58. https://doi.org/10.1785/bssa0400010053

Fujiwara, T. (2021). Seafloor geodesy from repeated multibeam bathymetric surveys: Application to seafloor displacement caused by the 2011 Tohoku-Oki earthquake. *Frontiers in Earth Science, 9.* https://doi.org/10.3389/feart.2021.667666

Fujiwara, T., dos Santos Ferreira, C., Bachmann, A. K., Strasser, M., Wefer, G., Sun, T., Kanamatsu, T., & Kodaira, S. (2017). Seafloor displacement after the 2011 tohoku-oki earthquake in the Northern Japan Trench examined by repeated bathymetric surveys. *Geophysical Research Letters, 44*(23). https://doi.org/10.1002/2017gl075839

Fujiwara, T., Kodaira, S., No, T., Kaiho, Y., Takahashi, N., & Kaneda, Y. (2011). The 2011 Tohoku-oki earthquake: Displacement reaching the trench axis. *Science*, *334*(6060), 1240. https://doi.org/10.1126/science.1211554

Geist, E. L., & Dmowska, R. (1999). Local tsunamis and distributed slip at the source. *Pure and Applied Geophysics*, *154*, 485–512. https://doi.org/10.1007/s000240050241

Gomez, B., & Kadri, U. (2023). Numerical validation of an effective slender fault source solution for past tsunami scenarios. *Physics of Fluids, 35*(4). https://doi.org/10.1063/5.0144360
Gusman, A. R., Tanioka, Y., Sakai, S., & Tsushima, H. (2012). Source model of the Great 2011 Tohoku earthquake estimated from tsunami waveforms and crustal deformation data. *Earth and Planetary Science Letters*, 341–344, 234–242. https://doi.org/10.1016/j.epsl.2012.06.006

Harris, R. A., & Day, S. M. (1997). Effects of a low-velocity zone on a dynamic rupture. *Bulletin of the Seismological Society of America, 87*(5), 1267–1280. https://doi.org/10.1785/bssa0870051267

Hill, E. M., Borrero, J. C., Huang, Z., Qiu, Q., Banerjee, P., Natawidjaja, D. H., Elosegui, P., Fritz, H. M., Suwargadi, B. W., Pranantyo, I. R., Li, L., Macpherson, K. A., Skanavis, V., Synolakis, C. E., & Sieh, K. (2012). The 2010 mw 7.8 mentawai earthquake: Very shallow source of a rare tsunami earthquake determined from Tsunami Field Survey and near-Field GPS Data. *Journal of Geophysical Research: Solid Earth, 117*(B6). https://doi.org/10.1029/2012jb009159

Horrillo, J., Kowalik, Z., & Shigihara, Y. (2006). Wave dispersion study in the Indian Ocean-Tsunami of December 26, 2004. *Marine Geod-esy*, *29*(3), 149–166. https://doi.org/10.1080/01490410600939140

Hossen, M. J., Cummins, P. R., Dettmer, J., & Baba, T. (2015). Tsunami waveform inversion for sea surface Displacement following the 2011 Tohoku earthquake: Importance of dispersion and source kinematics. *Journal of Geophysical Research: Solid Earth*, *120*(9), 6452–6473. https://doi.org/10.1002/2015jb011942

Iinuma, T., Hino, R., Kido, M., Inazu, D., Osada, Y., Ito, Y., Ohzono, M., Tsushima, H., Suzuki, S., Fujimoto, H., & Miura, S. (2012). Coseismic slip distribution of the 2011 off the Pacific coast of Tohoku earthquake (m9.0) refined by means of seafloor geodetic data. *Journal of Geophysical Research: Solid Earth, 117*(B7). https://doi.org/10.1029/2012jb009186

Iki, T. (1897). Field survey report of the 1896 Sanriku tsunami. *Rep Imp Earthq Invest Comm*, *11*, 5–34. (in Japanese).

Kajiura, K. (1963). Leading wave of a tsunami. *Bulletin of the Earthquake Research Institute*, *43*, 535–571. https://doi.org/10.1086/dia41504341

Kanamori, H. (1971). Seismological evidence for a lithospheric normal faulting—The Sanriku earthquake of 1933. *Physics of the Earth and Planetary Interiors*, *4*(4), 289–300. https://doi.org/10.1016/0031-9201(71)90013-6

Kanamori, H. (1972). Mechanism of tsunami earthquakes. *Physics of the Earth and Planetary Interiors, 6*(5), 346–359. https://doi.org/10.1016/0031-9201(72)90058-1

Kanamori, H., & Kikuchi, M. (1993). The 1992 Nicaragua earthquake: A slow tsunami earthquake associated with subducted sediments. *Nature, 361*(6414), 714–716. https://doi.org/10.1038/361714a0

Kato, A., & Igarashi, T. (2012). Regional extent of the large coseismic slip zone of the 2011 MW 9.0 tohoku-oki earthquake delineated by on-fault aftershocks. *Geophysical Research Letters, 39*(15). https://doi.org/10.1029/2012gl052220

Kido, M., Osada, Y., Fujimoto, H., Hino, R., & Ito, Y. (2011). Trench-normal variation in observed seafloor displacements associated with the 2011 Tohoku-Oki earthquake. *Geophysical Research Letters, 38*(24). https://doi.org/10.1029/2011gl050057

Kirby, J. T., Shi, F., Tehranirad, B., Harris, J. C., & Grilli, S. T. (2013). Dispersive tsunami waves in the ocean: Model equations and sensitiv-ity to dispersion and Coriolis effects. *Ocean Modelling*, *62*, 39–55. https://doi.org/10.1016/j.ocemod.2012.11.009

Kodaira, S., Fujiwara, T., Fujie, G., Nakamura, Y., & Kanamatsu, T. (2020). Large coseismic slip to the trench during the 2011 Tohoku-Oki earthquake. *Annual Review of Earth and Planetary Sciences, 48*(1), 321–343. https://doi.org/10.1146/annurev-earth-071719-055216

Kodaira, S., Iinuma, T., & Imai, K. (2021). Investigating a tsunamigenic megathrust earthquake in the Japan Trench. *Science, 371*(6534). https://doi.org/10.1126/science.abe1169

Kodaira, S., Nakamura, Y., Yamamoto, Y., Obana, K., Fujie, G., No, T., Kaiho, Y., Sato, T., & Miura, S. (2017). Depth-varying structural characters in the rupture zone of the 2011 Tohoku-Oki earthquake. *Geosphere, 13*(5), 1408–1424. https://doi.org/10.1130/ges01489.1

Kodaira, S., No, T., Nakamura, Y., Fujiwara, T., Kaiho, Y., Miura, S., Takahashi, N., Kaneda, Y., & Taira, A. (2012). Coseismic fault rupture at the trench axis during the 2011 Tohoku-Oki earthquake. *Nature Geoscience, 5*(9), 646–650. https://doi.org/10.1038/ngeo1547

Koketsu, K., Miyake, H., & Suzuki, H. (2012). Japan integrated velocity structure model version 1. Proceedings of the 15th world conference on earthquake engineering. https://www.iitk.ac.in/nicee/wcee/article/WCEE2012_1773.pdf

Kozdon, J. E., & Dunham, E. M. (2014). Constraining shallow slip and tsunami excitation in megathrust ruptures using seismic and ocean acoustic waves recorded on ocean-bottom sensor networks. *Earth and Planetary Science Letters, 396*, 56–65. https://doi.org/10.1016/j.epsl.2014.04.001

Kubota, T., Saito, T., & Hino, R. (2022). A new mechanical perspective on a shallow megathrust near-trench slip from the high-resolution fault model of the 2011 Tohoku-Oki earthquake. *Progress in Earth and Planetary Science, 9*(1). https://doi.org/10.1186/s40645-022-00524-0

Kurahashi, S., & Irikura, K. (2013). Short-period source model of the 2011 MW 9.0 off the pacific coast of Tohoku earthquake. *Bulletin of the Seismological Society of America, 103*(2B), 1373–1393. https://doi.org/10.1785/0120120157

Lay, T. (2018). A review of the rupture characteristics of the 2011 Tohoku-oki MW 9.1 earthquake. *Tectonophysics*, *733*, 4–36. https://doi.org/10.1016/j.tecto.2017.09.022

Lay, T., Kanamori, H., Ammon, C. J., Koper, K. D., Hutko, A. R., Ye, L., Yue, H., & Rushing, T. M. (2012). Depth-varying rupture properties of subduction zone megathrust faults. *Journal of Geophysical Research: Solid Earth, 117*(B4). https://doi.org/10.1029/2011jb009133

Lotto, G. C., & Dunham, E. M. (2015). High-order finite difference modeling of tsunami generation in a compressible ocean from offshore earthquakes. *Computational Geosciences, 19*(2), 327–340. https://doi.org/10.1007/s10596-015-9472-0

Lotto, G. C., Dunham, E. M., Jeppson, T. N., & Tobin, H. J. (2017). The effect of compliant prisms on subduction zone earthquakes and Tsunamis. *Earth and Planetary Science Letters, 458*, 213–222. https://doi.org/10.1016/j.epsl.2016.10.050

Lotto, G. C., Jeppson, T. N., & Dunham, E. M. (2018). Fully coupled simulations of megathrust earthquakes and tsunamis in the Japan Trench, Nankai Trough, and Cascadia Subduction Zone. *Pure and Applied Geophysics, 176*(9), 4009–4041. https://doi.org/10.1007/s00024-018-1990-y

Ma, K., Brodsky, E. E., Mori, J., Ji, C., Song, T. A., & Kanamori, H. (2003). Evidence for fault lubrication during the 1999 chi-chi, Taiwan, earthquake (MW7.6). *Geophysical Research Letters, 30*(5). https://doi.org/10.1029/2002gl015380

Ma, S. (2008). A physical model for widespread near-surface and fault zone damage induced by earthquakes. *Geochemistry, Geophysics, Geosystems, 9*(11). https://doi.org/10.1029/2008gc002231

Ma, S. (2012). A self-consistent mechanism for slow dynamic deformation and tsunami generation for earthquakes in the shallow subduction zone. *Geophysical Research Letters, 39*(11). https://doi.org/10.1029/2012gl051854

Ma, S. (2022). Dynamic off-fault failure and Tsunamigenesis at strike-slip restraining bends: Fully-coupled models of dynamic rupture, ocean acoustic waves, and tsunami in a shallow bay. *Tectonophysics*, *838,* 229496. https://doi.org/10.1016/j.tecto.2022.229496

Ma, S. (2023). Wedge plasticity and a minimalist dynamic rupture model for the 2011 MW 9.1 Tohoku-Oki Earthquake and Tsunami. *Tectonophysics, 869*, 230146. https://doi.org/10.1016/j.tecto.2023.230146

Ma, S., & Andrews, D. J. (2010). Inelastic off-fault response and three-dimensional dynamics of earthquake rupture on a strike-slip fault. *Journal of Geophysical Research: Solid Earth, 115*(B4). https://doi.org/10.1029/2009jb006382

Ma, S., & Beroza, G. C. (2008). Rupture dynamics on a bimaterial interface for dipping faults. *Bulletin of the Seismological Society of America, 98*(4), 1642–1658. https://doi.org/10.1785/0120070201

Ma, S., & Hirakawa, E. T. (2013). Dynamic wedge failure reveals anomalous energy radiation of shallow subduction earthquakes. *Earth and Planetary Science Letters, 375*, 113–122. https://doi.org/10.1016/j.epsl.2013.05.016

Ma, S., & Nie, S. (2019). Dynamic Wedge Failure and along-arc variations of Tsunamigenesis in the Japan Trench Margin. *Geophysical Research Letters, 46*(15), 8782–8790. https://doi.org/10.1029/2019gl083148

Ma, S., Custódio, S., Archuleta, R. J., & Liu, P. (2008). Dynamic modeling of the 2004 mw 6.0 Parkfield, California, earthquake. *Journal of Geophysical Research: Solid Earth, 113*(B2). https://doi.org/10.1029/2007jb005216

MacInnes, B. T., Gusman, A. R., LeVeque, R. J., & Tanioka, Y. (2013). Comparison of earthquake source models for the 2011 Tohoku event using tsunami simulations and near-field observations. *Bulletin of the Seismological Society of America, 103*(2B), 1256–1274. https://doi.org/10.1785/0120120121

Maeda, T., Furumura, T., Sakai, S., & Shinohara, M. (2011). Significant tsunami observed at ocean-bottom pressure gauges during the 2011 off the Pacific coast of Tohoku earthquake. *Earth, Planets and Space, 63*(7), 803–808. https://doi.org/10.5047/eps.2011.06.005

Matsuo, H. (1933). Report on the survey of the 1933 Sanriku tsunami. *Report of the Civil Engineering Laboratory*, *24*, 83–136. (in Japanese).

Mei, C. C., & Kadri, U. (2017). Sound signals of tsunamis from a slender fault. *Journal of Fluid Mechanics, 836*, 352–373. https://doi.org/10.1017/jfm.2017.811

Meng, Q., & Duan, B. (2023). Do upper-plate material properties or fault frictional properties play more important roles in tsunami earthquake characteristics? *Tectonophysics, 850*, 229765. https://doi.org/10.1016/j.tecto.2023.229765

Mori, N., Takahashi, T., Yasuda, T., & Yanagisawa, H. (2011). Survey of 2011 Tohoku earthquake tsunami inundation and run-up. *Geophysical Research Letters, 38*(7). https://doi.org/10.1029/2011gl049210

Newman, A. V., & Okal, E. A. (1998). Teleseismic estimates of radiated seismic energy: The E/m0 discriminant for tsunami earthquakes. *Journal of Geophysical Research: Solid Earth, 103*(B11), 26885–26898. https://doi.org/10.1029/98jb02236

Noda, H., & Lapusta, N. (2013). Stable creeping fault segments can become destructive as a result of dynamic weakening. *Nature, 493*(7433), 518–521. https://doi.org/10.1038/nature11703
Okada, Y. (1985). Surface deformation due to shear and tensile faults in a half-space. *Bulletin of the Seismological Society of America*, *75*, 1135–1154. https://doi.org/10.1016/0148-9062(86)90674-1

Okal, E. A. (1988). Seismic parameters controlling far-field tsunami amplitudes: A Review. *Natural Hazards, 1*(1), 67–96. https://doi.org/10.1007/bf00168222

Okal, E. A., Alasset, P.-J., Hyvernaud, O., & Schindelé, F. (2003). The deficienttwaves of tsunami earthquakes. *Geophysical Journal International, 152*(2), 416–432. https://doi.org/10.1046/j.1365-246x.2003.01853.x

Oliver, J., & Major, M. (1959). Leaking modes and the PL phase. *Seismological Research Letters, 30*(2), 18–18. https://doi.org/10.1785/gssrl.30.2.18a

Phinney, R. A. (1961). Leaking modes in the crustal waveguide: 1. the oceanic pl wave. *Journal of Geophysical Research, 66*(5), 1445–1469. https://doi.org/10.1029/jz066i005p01445

Polet, J., & Kanamori, H. (2000). Shallow subduction zone earthquakes and their tsunamigenic potential. *Geophysical Journal International, 142*(3), 684–702. https://doi.org/10.1046/j.1365-246x.2000.00205.x

Roeber, V., Cheung, K. F., & Kobayashi, M. H. (2010). Shock-capturing Boussinesq-type model for nearshore wave processes. *Coastal Engineering, 57*(4), 407–423. https://doi.org/10.1016/j.coastaleng.2009.11.007

Rogers, S. R., & Mei, C. C. (1978). Nonlinear resonant excitation of a long and narrow bay. *Journal of Fluid Mechanics, 88*, 161–180. https://doi.org/10.1017/s0022112078002037

Saito, T. (2019). *Tsunami generation and propagation*. Springer. https://doi.org/10.1007/978-4-431-56850-6

Saito, T., Inazu, D., Miyoshi, T., & Hino, R. (2014). Dispersion and nonlinear effects in the 2011 Tohoku-Oki earthquake tsunami. *Journal of Geophysical Research: Oceans, 119*(8), 5160-5180. http://doi:10.1002/2014jc009971

Sallarès, V., & Ranero, C. R. (2019). Upper-plate rigidity determines depth-varying rupture behaviour of megathrust earthquakes. *Nature, 576*(7785), 96–101. https://doi.org/10.1038/s41586-019-1784-0

Satake, K., & Tanioka, Y. (1999). Sources of tsunami and tsunamigenic earthquakes in subduction zones. *Seismogenic and Tsunamigenic Processes in Shallow Subduction Zones*, 467–483. https://doi.org/10.1007/978-3-0348-8679-6_5

Satake, K., Fujii, Y., & Yamaki, S. (2017). Different depths of near-trench slips of the 1896 sanriku and 2011 Tohoku earthquakes. *Geoscience Letters, 4*(1). https://doi.org/10.1186/s40562-017-0099-y

Satake, K., Fujii, Y., Harada, T., & Namegaya, Y. (2013). Time and space distribution of coseismic slip of the 2011 Tohoku earthquake as inferred from tsunami waveform data. *Bulletin of the Seismological Society of America, 103*(2B), 1473–1492. https://doi.org/10.1785/0120120122

Sato, M., Ishikawa, T., Ujihara, N., Yoshida, S., Fujita, M., Mochizuki, M., & Asada, A. (2011). Displacement above the hypocenter of the 2011 Tohoku-Oki earthquake. *Science, 332*(6036), 1395–1395. https://doi.org/10.1126/science.1207401

Scholz, C. H. (1998). Earthquakes and friction laws. *Nature, 391*(6662), 37–42. https://doi.org/10.1038/34097

Scholz, C. H. (2014). The rupture mode of the shallow large-slip surge of the tohoku-oki earthquake. *Bulletin of the Seismological Society of America, 104*(5), 2627–2631. https://doi.org/10.1785/0120140130

Seno, T. (2000). The 21 September, 1999 Chi-Chi earthquake in Taiwan: Implications for tsunami earthquakes. *Terrestrial, Atmospheric and Oceanic Sciences, 11*(3), 701. https://doi.org/10.3319/tao.2000.11.3.701(cce)

Shimozono, T., Cui, H., Pietrzak, J. D., Fritz, H. M., Okayasu, A., & Hooper, A. J. (2014). Short wave amplification and extreme runup by the 2011 Tohoku tsunami. *Pure and Applied Geophysics, 171*(12), 3217–3228. https://doi.org/10.1007/s00024-014-0803-1

Shimozono, T., Sato, S., Okayasu, A., Tajima, Y., Fritz, H. M., Liu, H., & Takagawa, T. (2012). Propagation and Inundation characteristics of the 2011 Tohoku tsunami on the Central Sanriku Coast. *Coastal Engineering Journal*, *54*(1). https://doi.org/10.1142/s0578563412500040

Shuto, N., Imamura, F., Koshimura, S., Satake, K., & Matsutomi, H. (2007). *Encyclopedia of tsunamis (tsunami no jiten)* (p. 350). Tokyo: Asakura Publishing.

Sun, T., Wang, K., Fujiwara, T., Kodaira, S., & He, J. (2017). Large fault slip peaking at Trench in the 2011 Tohoku-Oki earthquake. *Nature Communications, 8*(1). https://doi.org/10.1038/ncomms14044

Tanioka, Y., & Satake, K. (1996). Tsunami generation by horizontal displacement of Ocean Bottom. *Geophysical Research Letters, 23*(8), 861–864. https://doi.org/10.1029/96gl00736

Tanioka, Y., & Seno, T. (2001a). Detailed analysis of tsunami waveforms generated by the 1946 aleutian tsunami earthquake. *Natural Hazards and Earth System Sciences, 1*(4), 171–175. https://doi.org/10.5194/nhess-1-171-2001

Tanioka, Y., & Seno, T. (2001b). Sediment effect on tsunami generation of the 1896 sanriku tsunami earthquake. *Geophysical Research Letters, 28*(17), 3389–3392. https://doi.org/10.1029/2001gl013149

Tanioka, Y., Ramirez, A. G., & Yamanaka, Y. (2018). Simulation of a dispersive tsunami due to the 2016 El Salvador–Nicaragua outer-rise earthquake (M_w 6.9). *Pure and Applied Geophysics*, *175*(4), 1363–1370. https://doi.org/10.1007/s00024-018-1773-5

Tanioka, Y., & Satake, K. (1996). Tsunami generation by horizontal displacement of ocean bottom. *Geophysical Research Letters*, *23*(8), 861–864. https://doi.org/10.1029/96gl00736

Tanioka, Y., & Seno, T. (2001). Sediment effect on tsunami generation of the 1896 Sanriku tsunami earthquake. *Geophysical Research Letters*, *28*(17), 3389–3392. https://doi.org/10.1029/2001gl013149

Tappin, D. R., Grilli, S. T., Harris, J. C., Geller, R. J., Masterlark, T., Kirby, J. T., Shi, F., Ma, G., Thingbaijam, K. K. S., & Mai, P. M. (2014). Did a submarine landslide contribute to the 2011 Tohoku tsunami? *Marine Geology, 357*, 344–361. https://doi.org/10.1016/j.margeo.2014.09.043

Tsuru, T., Park, J., Miura, S., Kodaira, S., Kido, Y., & Hayashi, T. (2002). Along-arc structural variation of the plate boundary at the Japan Trench Margin: Implication of interplate coupling. *Journal of Geophysical Research: Solid Earth, 107*(B12). https://doi.org/10.1029/2001jb001664

Uchida, N., & Bürgmann, R. (2021). A decade of lessons learned from the 2011 tohoku-oki earthquake. *Reviews of Geophysics, 59*(2). https://doi.org/10.1029/2020rg000713

Ueda, H., Kitazato, H., Jamieson, A., Bond, T., Cardigos, S., Funaki, M., Maroni, P. J., Nanbu, H., O'Callaghan, J. M., Onishi, T., Pedersen, S. W., Roperez, J., Tsuruzono, H., Watanabe, H. K., & Yasuda, T. (2023). The submarine fault scarp of the 2011 Tohoku-Oki earthquake in the Japan Trench. *Communications Earth & Environment, 4*(1). https://doi.org/10.1038/s43247-023-01118-4

Utsu, T. (1994). Aftershock activity of the 1896 sanriku earthquake. *Zisin (Journal of the Seismological Society of Japan. 2nd Ser.), 47*(1), 89–92. https://doi.org/10.4294/zisin1948.47.1_89

Wang, X., & Power, W. (2011). COMCOT: A tsunami generation propagation and run-up model. *GNS Science Report*, New Zealand.

Wilson, A., & Ma, S. (2021). Wedge plasticity and fully coupled simulations of dynamic rupture and tsunami in the Cascadia Subduction Zone. *Journal of Geophysical Research: Solid Earth, 126*(7). https://doi.org/10.1029/2020jb021627

Yamanaka, Y., & Nakamura, M. (2020). Frequency-dependent amplification of the Sanriku tsunamis in Ryori bay. *Earth, Planets and Space*, *72*(1). https://doi.org/10.1186/s40623-019-1128-1

Yamazaki, Y., Cheung, K. F., & Lay, T. (2018). A self-consistent fault slip model for the 2011 Tohoku earthquake and Tsunami. *Journal of Geophysical Research: Solid Earth, 123*(2), 1435–1458. https://doi.org/10.1002/2017jb014749

Yin, J., & Denolle, M. (2021). *The Earth Surface Controls the Depth-Dependent Seismic Radiation of Megathrust Earthquakes*. https://doi.org/10.1002/essoar.10506212.1

Young, D. M. (1971). *Iterative solution of large linear systems*. Academic Press.

Zhang, K., Wang, Y., Luo, Y., Zhao, D., Wang, M., Yang, F., & Wu, Z. (2023). Complex tsunamigenic near-trench seafloor deformation during the 2011 Tohoku–Oki Earthquake. *Nature Communications, 14*(1). https://doi.org/10.1038/s41467-023-38970-z